ADVERTIMENT. L'accés als continguts d'aquesta tesi queda condicionat a l'acceptació de les condicions d'ús establertes per la següent llicència Creative Commons: 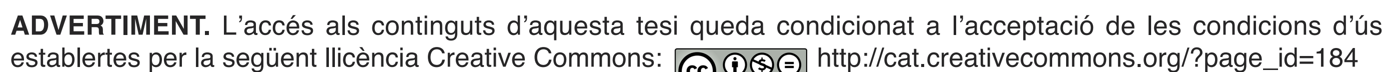 http://cat.creativecommons.org/?page_id=184

ADVERTENCIA. El acceso a los contenidos de esta tesis queda condicionado a la aceptación de las condiciones de uso establecidas por la siguiente licencia Creative Commons: 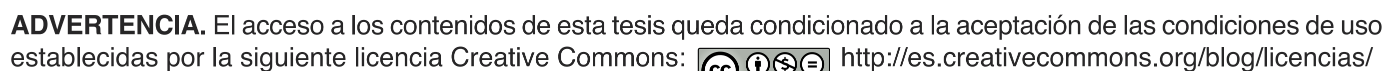 http://es.creativecommons.org/blog/licencias/

WARNING. The access to the contents of this doctoral thesis it is limited to the acceptance of the use conditions set by the following Creative Commons license: 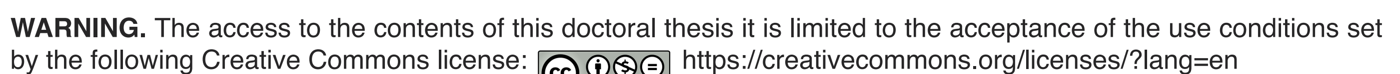 https://creativecommons.org/licenses/?lang=en

FACULTY OF SCIENCE – DEPARTMENT OF PHYSICS

Characterization of nanostructured materials for thermal conduction and heat transfer control

DOCTORAL THESIS – MAY 2017

Alexandros El Sachat

Director: Dr. Francesc Alzina

Tutor: Prof. Jordi Mompart

This ph.D thesis has been developed at the Catalan Institute of Nanoscience and Nanotechnology (ICN2). The research work has been funded from the EU FP7 project QUANTIHEAT (Grant No 604668).

Contents

Abstract

Abbreviation List

1. Introduction 1
    1.1 Organization. 7
2. Experimental Methods. 8
    2.1 Scanning Thermal Microscopy (SThM) 8
    2.2 Two Laser Raman Thermometry (2LRT) 24
    2.3 Energy Dispersive X-ray Spectrometry (EDS) 28

RESULTS

3. Nanomembranes. 30
    3.1 Si membranes: Thickness dependence of the thermal conductivity at high temperatures. 31
    3.2 Heat transport tuning in Si membranes patterned with holes 35
4. $Si_{1-x}Ge_x$ epitaxial nanowires. 51
    4.1 Structural characterization. 52
    4.2 Composition study. 57
    4.3 SThM measurements. 60
5. Self-assembled block copolymer nanostructures. 77
    5.1 Preparation of block copolymer templates. 78
    5.2 Structural characterization. 80
    5.3 SThM measurements. 83
6. Conclusions and perspectives 95

References. 98

Acknowledgements 106

Publication List. 108

Abstract

The main objective of this thesis is the study of thermal properties of nanostructured materials as a mean to control heat transport. For this purpose thermal measurements with different experimental techniques on length scales covering tens of microns to sub-50 nm have been performed. Two experimental techniques in particular have been studied and presented in this thesis: (a) the scanning thermal microscopy technique (SThM) and (b) the two-laser Raman thermometry (2LRT). These techniques have been extensively applied to successfully measure thermal properties in various nanomaterials. In particular, two configurations of Si based materials are investigated using 2LRT: (a) Si membranes with thicknesses ranging from 8 to 1000 nm and (b) periodic porous membranes with different lattice parameters and disordered pattern. The results obtained showed that the in-plane thermal conductivity of silicon and its temperature evolution from room temperature to about 1000 K can be effectively reduced and tuned by (i) thickness and (ii) periodic patterning (holes). We attribute the reduction of the thermal conductivity to the shortening of the phonon mean free path Λ due to diffuse (incoherent) phonon-boundary scattering. Furthermore, we showed that the temperature dependence of the thermal conductivity of Si membranes in the high temperature range (from 400 to 1000 K) is governed by phonons with mean free path smaller than 200 nm. To investigate thermal transport in supported nanostructures and in smaller length scale, we studied heat transfer between different heated scanning probe sensors and nanomaterials, such as, (i) in-plane epitaxial $Si_{1-x}Ge_x$ alloy nanowires and (ii) self-assembled block copolymer nanostructures, provided high resolution thermal images of sub-50 micrometre structures with sub-20 nm spatial resolution. The combination of the two experimental techniques was crucial for the thermal characterization of different material systems and the better understanding of fundamental aspects of thermal transport.

Abbreviation List

T: Temperature

T_g: Glass transition temperature

k: Thermal conductivity

C_p: Heat capacity

t: Membrane thickness

d: Hole diameter in PnCs

α: Lattice parameter

n: Neck size

Λ: Mean free path

R_p: Probe thermal resistance in vacuum

R_{pr}: Probe thermal resistance in air

R_{pr}^{el}: Probe electrical resistance

I: Electrical current

V: Voltage

V_{out}: Output voltage of the Whetstone bridge

$V_{in,con}$: Output voltage of the Whetstone bridge in contact with the sample

$V_{out,con}$: Output voltage of the Whetstone bridge in contact with the sample

G_{th}: Total thermal conductance between tip-sample

G_{sol}: Thermal conductance through the mechanical contact

G_W: Thermal conductance through the water meniscus

G_{rad}: Thermal conductance through radiation

L_t: Length of the Pt wires in the thermal probe

NA: Numerical aperture

P_0: Absorbed power

A: Cross sectional area

k_r: Relative thermal conductivity

V_s: Source voltage

R_x : Variable resistor in the Wheatstone bridge

R_1 , R_2 : constant resistors in the Wheatstone bridge

X: Amplification factor

P_{ts} : Power dissipated into the sample

p: Hole position in the PnCs

φ: Filling fraction

ε: Correction factor

P_{loss}: Absolute value of air losses

w: Nanowires width

L: Nanowires length

h: Nanowires height

r_c: Radius of the thermal tip

T_g: Glass transition temperature

D: Average spacing between the PEO cylinders

r: Radius of the PEO cylinders

Q_{total}: Total Joule heat generated by the current

Q_t: Heat flux generated to the probe

Q_{ts}: Heat flux transferred from the probe to the sample

r_{int}: Interface resistance between the SiGe NWs and Si substrate

RMS: Root Mean Square

EELS: Electron Energy-Loss spectroscopy

1

Introduction

Nowadays, from the technological perspective, thermal characterization and energy dissipation at the nanoscale range consist of critical issues for evaluating a variety of electronic and photonic devices. Progress in thermal management at the nanoscale is important to continued advances in microelectronic industry related with optoelectronic, phase-change memory, heat-assisted magnetic storage and high efficient thermoelectric devices.[1-3] However, with the continuous downscale of device features ($< 45\,nm$) thermal management and characterization are becoming increasingly more challenging. The performance and the reliability of these devices are highly connected with the efficient control of the thermal transport, thus there is a need for a greater scientific understanding of the basic principles governing the heat transfer at the nanoscale. As one notable example, microelectronics primary goals, such as the efficient heat removal or cooling of integrated circuits, are directly related with thermal management processes. Therefore, the ability to better control heat propagation at the nanoscale would result in more efficient thermal designs. On the other hand, from a purely scientific perspective fundamental processes, such as thermal energy transfer and conversion, especially in sub-micron scale, are essential to be further investigated.

Toward this direction, there has been a lot of effort in recent years to develop techniques for characterizing the thermal behaviour of nanostructured materials and overcome the experimental lack of tools to quantify thermal transport down to submicron length scales.[1,4-6] In general, thermal instruments can be broadly categorized as electrical and optical or contact and non-contact, and can be classified according to their applications and performance. Depending on the materials and structures under

investigation, and the required material property that needs to be measured, either of these techniques might be convenient. Several electrical and optical measurement techniques have been developed to measure thermal properties of a large variety of materials and structures.[1,4,7-9]

In the electrical measurement techniques physical materials properties, such as temperature, are converted into electrical signals. Depending on the experimental configuration electrical quantities such as, voltage, current, and resistance can be measured. Standard methods used today to study thermal transport properties include the 3ω technique[10] for thin films and the micro-electro-mechanical measurement (MEMS) platform.[7,9] The latter usually consist of two suspended membranes patterned with heating/sensing elements. Temperature measurements can be performed by placing the sample between the heat source and the thermometer (heat sink). The sample is heated by the heat source with known steady-state power input, and the temperature sensor measures the resulting temperature drop ΔT across a given length of the sample. The information of the ΔT then can be used to obtain intrinsic material properties, such as the thermal conductivity (k). In similar configurations, the temperature of a sample can be measured through electrical resistance measurements by using two or four probe measurements.[11] In the latter a current source is supplied to two outside terminals of the device, and the voltage drop across the device is measured using the two inside terminals. The main disadvantages of the electrical techniques are related with difficulties in sample preparation, the limited temperature range of measurements, the risk of sample contamination and contact resistance issues.

On the contrary, in optical techniques there is no interference between heater/sensor and sample and measurements can be performed at high temperatures. In optical measurements the parameter that needs to be measured is converted into some form of electrical signal through different kind of photo-detectors. For example in optical spectroscopy, which includes pump-probe spectroscopy methods (e.g., time domain thermoreflectance and Raman spectroscopy), is studied absorption and emission of light by the sample. The basic idea is the use of light to heat and probe changes in the materials properties. In Raman spectroscopy for example photons of the

laser light are absorbed and reemitted by the sample. The shift in wavelength of the inelastically scattered light can provide except of chemical and structural information as well as information regarding the temperature of the sample. For temperature measurements, a calibration of the Raman shift with temperature is necessary. Generally, the non-contact temperature measurements usually exhibit high accuracy with no distortion of measured values, as compared to measurements with contact thermometers. The major disadvantage in the optical techniques is the diffraction limited spatial resolution ($\sim 300\ nm$). Note that in both electrical and optical techniques different heat sources can be supplied, either periodically or as a pulse, resulting in periodic (phase signal output) and transient (amplitude signal output) temperature changes in the sample, respectively. In these cases the measured physical properties are time-dependent and measured during the process of heating up. Transient methods are usually used for diffusivity measurement.
Among the aforementioned electrical and optical techniques, scanning probe microscopy (SPM) and Raman thermometry have proven to be of great potential. Next, this chapter focuses to a literature review of the present state of the art on thermal transport studies using SPM techniques and Raman thermometry, which have been applied in the experiments presented in the following chapters.

The standard Raman thermometry or single laser Raman thermometry method[12] is a non-invasive optical technique which has been widely used to investigate the thermal conductivity of various materials[13,14–19] such as carbon nanotubes, Si, SiGe, Ge, GaAs[20-24] or graphene.[19] Briefly, the temperature rise (T_{max}) at the focused laser spot, which depends on the incident laser power, is obtained from the spectral position of the Raman active phonon modes, provided that a previous calibration of the Raman shift with temperature has been made. On a macroscopic length scale, heat transport is generally described as diffusive following Fourier´s law of heat conduction. Subsequently, in this heat transport regime the steady-state heat equation can be solved analytically or numerically, depending on the geometry and dimensionality of the sample, to obtain the relationship between thermal conductivity (k), temperature rise (T_{max}) and the absorbed power on the sample (P_o). To obtain reliable quantitative information on the

local thermal conductivity with this method, the knowledge of three major parameters is required: The intensity profile of the exciting laser, the geometry of the sample and the absorbed optical heating power. The last parameter is the most critical, particularly in complex structures (e. g., rough surfaces, porous materials) where the direct measurement of reflected and transmitted excitation power can be difficult.[12,25] Therefore assumptions on absorption coefficients and reflectivities have to be made. This technique offers a spatial resolution on the micrometre scale and is given from the excited laser spot size. A novel contactless technique for thermal conductivity determination and thermal field mapping has been reported recently.[21] This technique directly maps the thermal field and from a single measurement of the absorbed power the thermal conductivity is extracted. This technique is presented in detail in the experimental methods (chapter 2).

Scanning Probe Microscope (SPM) techniques such as Scanning Tunnelling Microscopy (STM)[26,27] and Atomic Force Microscopy (AFM),[28] provide a great potential solution for nanoscale characterization and are widely used to measure physical properties, such as static charge distribution, localized friction, magnetic fields, elastic moduli, and thermal properties as well. The introduction of the SPM techniques has been made first from Williams and Wickramasinghe,[29] where they introduced a new high-resolution profilometer based upon a non-contacting near-field thermal probe by using a thermocouple sensor with dimensions approaching 100 nm. This work has shown a lateral resolution of 100 nm and a depth resolution of 3 nm. In STM a tunnelling sensor is used to measure the current passing between a metal probe and a conductive sample in extremely close proximity. These measurements are governed by near-field electromagnetic interactions between the tip and the sample and still are not fully understood. STM can provide temperature measurements with spatial resolution as small as 10 nm.[27] However, the main limitation of this technique is that the sample has to be conducting.

On the other hand, the SThM is an AFM-based technique, which relies on thermal conduction between tip and sample and can be used for non-conductive materials. SThM has been developed in order to investigate the

thermal properties of materials, such as thermal conductivity, and thermal quantities, such as temperature, with sub-micron resolution. Nowadays SThM benefits from the AFM performances that allow imaging and analysis of the surface properties at sub-micrometre scales, as well as the study of the physical mechanisms of interaction between thermal probe and sample. The key element in this technique is the probe. It generally consists of a small thermal sensor built at the extremity of a tip supported by a cantilever. In particular, the SThM technique has been applied in different areas for temperature mapping[30-34] and thermal conductance measurement[35-38] by using either thermocouples or resistive thermal probes. A very common resistive probe is based on a Wollaston wire.[38-41] This wire is etched at the tip over a length of 200 μm and acts like an AFM cantilever.

The principle of operation of the resistive-SThM probes is based on the fact that the resistance of the probes is dependent upon temperature, which in turn is related to the temperature of the sample. The variation of the resistance is measured with an accurate method. Several kinds of resistive probes have been used. They differ by the cantilever/tip geometry and size, by the type of material that forms the resistive sensor and by the location of the sensor near or at the probe apex.[41] There are two types of operation in resistive probes, the "passive" mode and the "active" mode.[42] In the "passive" mode the probe acts as a detector (thermo-sensing element). In this case, a low constant current (in order to make the Joule heating of the probe negligible) is passed through the probe. The probe brought in contact with the sample and during the scanning across the sample the resistance of the probe changes due to the temperature differences on the sample. The probe resistance variations are monitored, and a representative temperature map is obtained. Such measurement, for example are used for mapping the temperature distribution in self-heated structures and devices.[33,35,42-44] In the "active" mode the thermal probe acts as a heater and thermometer. Therefore a large constant current (sufficient to raise the temperature of the probe above that of the sample surface) is passed through the probe. In this case, when the probe is in contact with the tested sample, the heat flux from the tip to the sample results in a decrease in the tip temperature and therefore in the probe resistance. By scanning the sample surface, a thermal resistance mapping can be obtained. However, the major difficulty is to

relate the signals acquired to the thermal conductivity of the sample in contact, mainly due to the different heat transfer mechanisms of the tip-sample system and the position dependent thermal contact resistance between the probe and the sample. Consequently, for the determination of intrinsic material properties, such as thermal conductivity, a specific thermal model of the probe-sample system taking into account the surrounding environment is required. This issue is further discussed in chapter 2 and 4 of this thesis. Nowadays, still there is a significant effort to find a way to determine quantitatively the thermal conductivity and establish a proper theoretical model of the probe-sample system.[41,42,45,47] This is the reason why thermal conductivity measurements using the SThM technique are challenging and not widely used. More recently, quantitative thermal analysis of the SThM measurements have been achieved by using resistive-SThM probes with a spatial resolution in the nanometre range.[37,41,47]

Besides resistive SThM probes, thermocouple probes have been used widely for temperature measurements.[48,49] The thermocouples rely on the Seebeck effect to measure temperatures. For that, two metals need to be welded and form a thermocouple junction. Temperature changes at the tip apex result in a voltage in the thermocouple junction. In this case the evaluated quantity is the thermo-voltage (Seebeck voltage). The corresponding current is amplified by a trans-impedance amplifier to generate an output voltage. The proportion coefficient between the measured and the actual temperature depends on the thermal resistance values of the different components of the system's thermal circuit. In particular, it has been found that this coefficient changes as the measured feature size decreases.[42] Thus, the calibration coefficient should be extracted from a measurement of a controlled calibration sample with similar characteristic sizes than the one to be measured. For both thermocouple and thermistor-based SThM temperature measurements, the key technical challenge is to understand how the measured temperature signal is related with the sample surface temperature. Over the last decade, there have been significant improvements in thermal spatial resolution, better than $20\,nm$, temperature precision to $30\,mK$ and measurements of nanometer-scale heat flows to $10\,pW$.[33,35,37,50] Despite the fact that SThM has been in development more than 25 years there are still many challenges and unanswered fundamental questions.

1.1 Organization

The thesis is organized in six chapters. The first chapter is devoted to a review of the state of the art of the techniques for temperature fields and thermal transport studies, focusing mostly on SThM and Raman thermometry. The experimental methods that have been used in this thesis are described in detail in the second chapter. In chapters three, four and five, we present and discuss the experimental results . Each of these chapters is devoted to a complete experimental work, starting with an introduction, which contains the background of the investigated subject and addresses the open scientific questions, and ending with a short summary highlighting the main results. In the final chapter of the thesis, we provide the main conclusions and possible directions to continue the research.

2
Experimental methods

2.1 Scanning Thermal Microscopy (SThM)

The first experimental technique described in this chapter is the scanning thermal microscopy (SThM). We first present our system and the principle of operation used in this thesis in order to perform thermal measurements in ambient environment. Next, we briefly described the high vacuum-based thermal microscope set-up used during my research stay at the University of Lancaster (ULANC).

The Scanning Thermal Microscope in ambient environment

Our Nanonics MV4000 SPM system is based on an open architecture, which allows flexible integration of different analytical tools. Figures 1a,b show the complete system which consists of several subsystems such as an integrated dual microscope, two scanning probe heads and a sample scanning stage. The dual probe configuration is shown in Fig. 1c. The MV400 it's an SPM that depending on the probe can be used for atomic force imaging, near-field optical measurements optical (SNOM), thermal (SThM) measurements, nanochemical writing on a variety of structures and probe nanoindentation. In this work it has been used for SThM measurements by using thermo-resistive probes supplied by the same company.

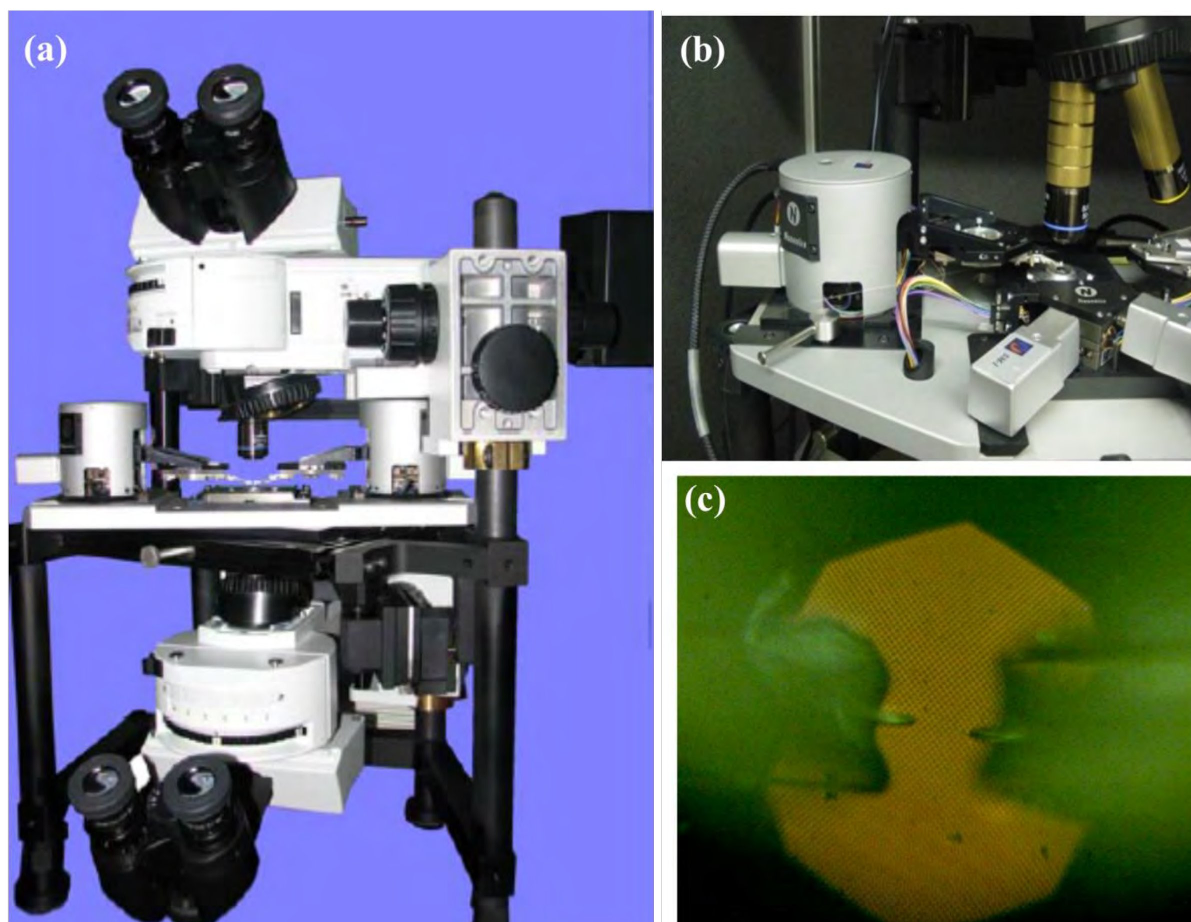

Fig. 1 (a) The Scanning thermal microscope, (b) closer view of the scanning probe head, the scanner stage and the top integrated microscope and (c) optical image of the dual-probe configuration.

A schematic representation of the scanning probe heads with two towers integrated is shown in Fig. 2. Each tower contains a tip-scanning stage, a tip mount, a pre-amplifier, a Z stepper motor, XY stepper motors and electrical connectors. The sample is placed on the lower scanner which performs sample scanning. Each probe's height is individually controlled by a Z stepper motor unit, located inside the tower. Each tower includes two XY lateral stepper motors, used for rough positioning of the tip. The towers and the lower scanner stage are placed on an interface plate, which sits on the XY stage of the optical microscope.

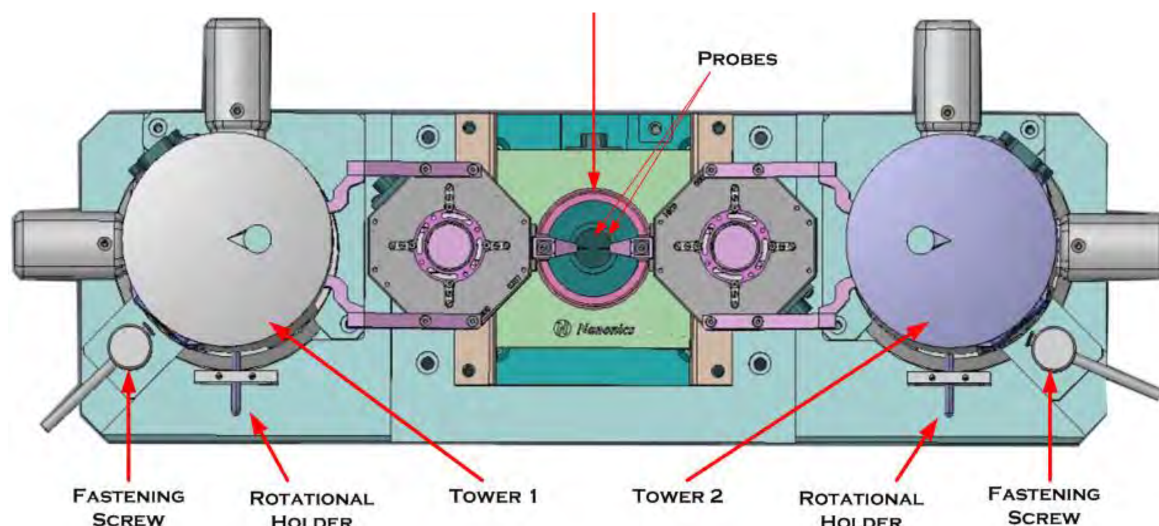

Fig. 2 Schematic representation of the scanning probe heads integrated in the scanning thermal microscope

Each tower can be rotated around its base for probe/sample mounting. The tip-mount attaches to the electroblock via an electrode panel at its back, and tapers at its front, where a tuning fork is mounted, to which the AFM probe is attached. This structure can be seen in detail in Fig. 3. The two tines of the tuning fork are connected via wires (red arrows) to the two outer electrodes on the tip-mount electrode pad. These electrodes transmit the signals generated by the tuning fork response.

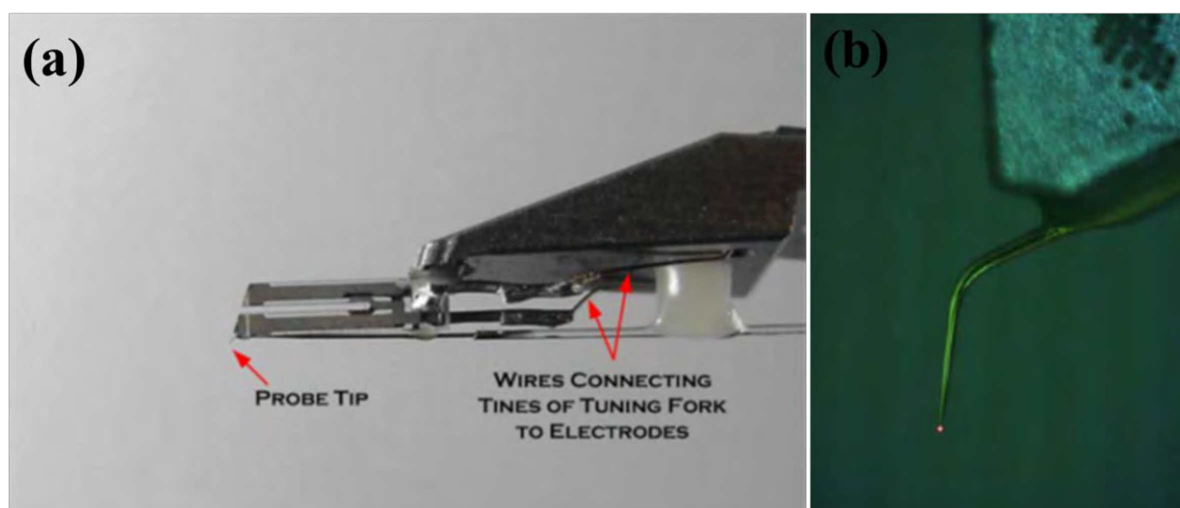

Fig. 3 (a) The tuning fork portion of a tip-mount (left image) and (b) an AFM probe which extends beyond the end of the tuning fork and showing both cantilever and tip (right image).

These signals are amplified and sent a specific controller for generation of the error signal. The two inner electrodes on the tip-mount electrode pad are used only with thermal probes. Our probes are based on glass pulling technology. The fiberglass probe is bonded lengthwise along the lower surface of the bottom tine of the tuning fork, and protrudes beyond it at different cantilever lengths, depending upon the type of probe employed. The part of the probe protruding beyond the tuning fork consists of a cantilever and the tip. The length of each element is customized according to the application. For example, longer cantilevers are required for NSOM measurements, while longer tips are needed for deep-trench AFM imaging.

Next, we focus on thermal probes used for probe resistance measurements. As already discussed in the introduction, the design of a resistive probe has a significant impact on the SThM performance. Spatial and thermal resolutions of resistive-based SThM are dependent on tip sharpness, tip sample heat transfer mechanism and thermal design of the probe. Our resistive probes are made of two platinum (Pt) wires stretched through a glass nanopipette (borosilicate glass) and fused together at their ends. This fused junction has a resistance that is temperature dependent. The Pt double wires have resistance between 20-150 *ohms* and a temperature coefficient of resistance of 3.8 $(^0C^{-1})$. The change in the resistance is measured as a change of the output voltage across a Wheatstone bridge circuit (thermal control unit supplied by Nanonics). The temperature sensitivity is around 10 millidegrees and the thermal lateral resolution can be as low as 100 nm. The mechanical interaction between the tip and the surface is controlled using the tuning fork that can use both amplitude and phase signals in the feedback loop. In this case the problems related to external heating of the probe in laser-beam-bounce detection are avoided.

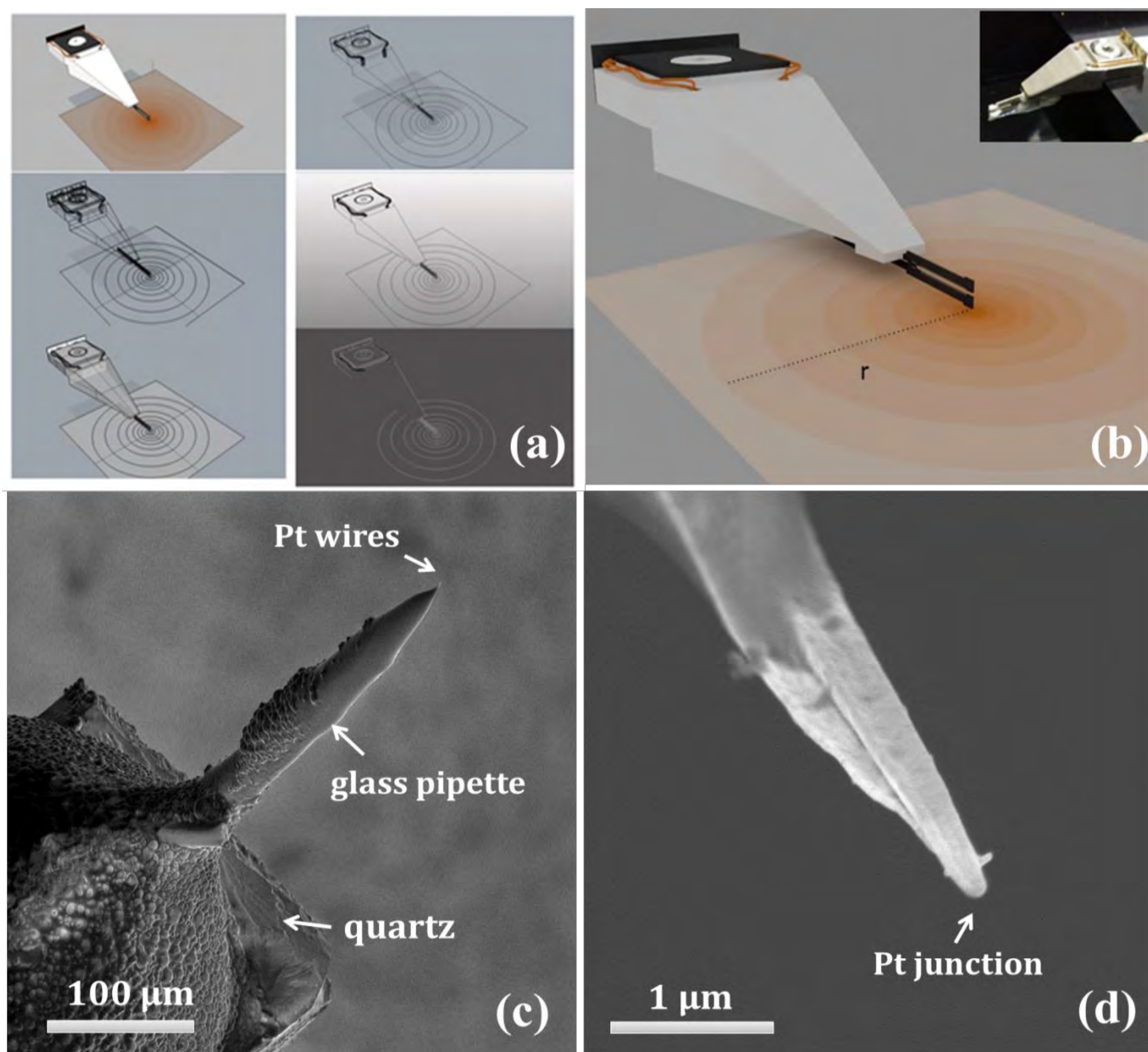

Fig. 4 (a), (b) Schematic representation of the dual-wire thermoresistive probe. (c), (d) SEM image of themoresistive probe showing the quartz tuning fork and the nanopipette with the integrated Pt resistive elements. (d) SEM image showing the nanometer-scale junction formed at the end of the Pt wires.

Principle of operation of the dual-wire resistive thermal probe

Our SThM works on an ambient air. Recalling the operational modes described in the introduction, in this work the active operational mode with a DC current was mostly used. We probed variations of tip-sample effective thermal conductance or resistance by monitoring changes in heat flux related signals by the change of the probe electrical resistance. The relation between the probe electrical resistance and the direct measurement of the experiment is described in the following analysis.

Assuming that the temperature range is not very wide, the electrical resistance of the resistive probes changes approximately linearly with temperature as follow:[51]

$$R_{pr}^{el}(T) = R_{pr(0)}^{el}\,[1 + \lambda\,(T - T_0)] \quad (1)$$

where $R_{pr(0)}^{el}$ is the electrical resistance of the probe at ambient temperature, T_0 the ambient temperature and λ the temperature coefficient of the resistance of the probe material. For the dual wire platinum Pt resistive probe used in the present study, $R_{pr(0)}^{el} = 50\ Ohms$ and $\lambda = 3.8\ (^0C^{-1})$. In our experimental setup, a Wheatstone bridge circuit allows to monitor changes in the probe resistance due to a variation in probe temperature, which is related to heat loss from the probe to the sample under study. A schematic representation of the Wheatstone bridge is shown in Fig. 5. The two resistors R_1 and R_2 have constant values 49.9 and 51.1 $Ohms$ respectively, while the source voltage (V_s) is fixed to 15 V.

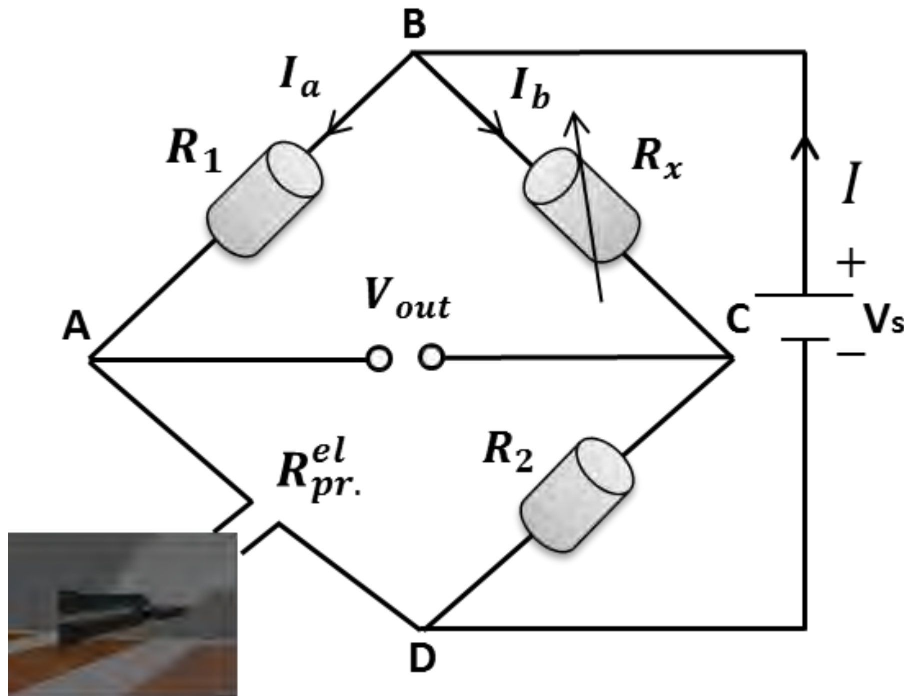

Fig. 5 Schematic of the Wheatstone bridge circuit.

When the bridge is balanced, the variable resistor (R_x) is adjusted in order to have $V_{AC} = 0$. In this case, the voltage drop from B to A is equal to the voltage drop from B to C ($V_{BA} = V_{BC}$). Therefore we can write:

$$I_a R_1 = I_b R_x \quad (2)$$

$$I_a R_{pr(0)}^{el} = I_b R_2 \quad (3)$$

Dividing eq. (3) by eq. (2) we have the relation between the resistors:

$$R_{pr(0)}^{el} = \frac{R_1 R_2}{R_x} \quad (4)$$

In unbalanced conditions by applying Kirchhoff's voltage law and Ohm's law to the upper and lower arms of the bridge, we have the following expressions:

$$V_s = I_a\left(R_{pr}^{el} + R_1\right) = I_b(R_x + R_2) \quad (5)$$

$$V_{AC} = V_A - V_C = (V_D - V_C) - (V_D - V_A) = -I_b\, R_2 - (-I_a\, R_{pr})$$

$$V_{AC} = I_a\, R_{pr}^{el} - I_b R_2 \quad (6)$$

Using eq. (5) to find I_a and I_b and substituting these in eq. (6), we have the expression of the output voltage as a function of the resistors forming the bridge:

$$V_{AC} = V_S\left(\frac{R_{pr}^{el}}{R_1 + R_{pr}} - \frac{R_2}{R_2 + R_x}\right) \quad (7)$$

V_{out} is inverted by the amplification circuit and, thus, the measured output voltage can be written as follows:

$$V_{out} = V_{AC}(-X) = XV_S\left(\frac{R_2}{R_2 + R_x} - \frac{R_{pr}^{el}}{R_1 + R_{pr}^{el}}\right) \quad (8)$$

where X is the amplification factor. In order to see how the V_{out} changes when R_{pr}^{el} changes from $R_{pr(0)}^{el}$ to $R_{pr(0)}^{el} + \varDelta R_{pr}^{el}$ we write:

$$\varDelta V_{out} \approx \varDelta R_{pr}^{el}\left(\frac{dV_{out}}{dR_{pr}^{el}}\right)_{R_{pr}^{el}=R_{pr(0)}^{el}} = -XV_S\, \frac{R_1}{(R_1 + R_{pr(0)}^{el})^2}\varDelta R_{pr}^{el} \quad (9)$$

Substituting eq. (4) into eq. (9) we obtain:

$$\Delta V_{out} = -QV_S \frac{\Delta R_{pr}^{el}}{R_1\left(1+\frac{R_2}{R_x}\right)^2} \qquad (10)$$

Therefore, ΔV_{out} is directly proportional to the change of the probe resistance ($\Delta V_{out} \propto \Delta R_{pr}^{el}$). Similarly, we can estimate changes of the power dissipated into the sample (ΔP_{ts}) considering small changes of the probe resistance as follow:

$$\Delta P_{ts} = \left(\frac{dP_{ts}}{dR_{pr}^{el}}\right)\Delta R_{pr}^{el} = \frac{d}{dR_{pr}^{el}}\left(\frac{V_{pr}^2}{R_{pr}^{el}}\right)\Delta R_{pr}^{el} \qquad (11)$$

Taking into account eq. (10) and eq. (4), eq. (11) then becomes:

$$\Delta P_{ts} = V_S \frac{R_2}{R_x+R_2}\left[\frac{2}{R_{pr}^{el}} - \frac{R_2}{R_x+R_2}\frac{\left(R_1+\frac{R_2R_1}{R_x}\right)^2}{R_1}\frac{1}{{R_{pr}^{el}}^2}\right]\Delta V_{out} \qquad (12)$$

In this case, we can directly correlate changes of $\Delta P_{ts}$with changes of the measured output voltage ($\Delta P_{ts} \propto \Delta V_{out}$) and estimate the change of the power dissipated into the sample.

Sensitivity of the SThM probe in thermal conductivity

Here we study the sensitivity of the Pt thermal probe in samples with different thermal conductivity. For this purpose different samples with known thermal conductivities and similar average surface roughness were measured covering a thermal conductivity range from $1.2 - 393\ Wm^{-1}K^{-1}$. Changes in the heat flux was monitored through the change of the probe resistance, which then resulted in a change of the differential output voltage of the Wheatstone bridge as described before. By measuring the response of the probe into these samples, we related the different measured output voltages with known thermal conductivity values.

Particularly, when the heated tip is brought in contact with the sample the heat flows from the tip to the sample causing a decrease in the tip

temperature which theoretically can be related with the sample thermal conductivity. We note that this relationship requires the assumption that the thermal conductance between the scanning probe sensor and the sample is not suppressed by the structural size of the tip. The validation of this assumption is questioned particularly in materials with relative large topography variations, which usually lead to a position dependent thermal interface resistance. However, for bulk samples with very low values of roughness this assumption can be made. Next we present an experimental methodology for sample thermal conductivity determination, assuming that the sample can be considered as bulk. For more complex structures both the thermal resistance of the scanning probe tip and the tip-sample interface thermal resistance need to be studied.

The exact experimental procedure of the calibration is given below:

1) The current is set to the working value in active mode (3.2 mA).

2) The Wheatstone bridge is balanced ($\Delta V_{out} = 0$) when the probe is far away from the sample surface. In all the calibration samples this distance was kept constant in order to ensure that we don't have heat transfer between the tip and the sample

4) AFM feedback tuning and setting parameters. The Wheatstone bridge was balanced through lock-in settings, where we set the resonance frequency of the cantilever (~ 39.04 kHz). By setting the same frequency each time we ensure that the amplitude of the contacting forces is in the same range in different experiments.

5) With the probe out of contact we were monitoring the output voltage of the Wheatstone bridge circuit for 30 sec by recording three values each 10 seconds in order to see the evolution of thermal signal with time. The value is close to zero but not exactly zero ($V_{out,con.}$) due to a thermal drift.

6) The probe is approached to the sample surface.

7) After waiting for stabilization, the thermal probe was brought in contact with the sample for 30 seconds and we recorded similarly three values every 10 seconds the voltage at the bridge ($V_{in,con.}$).

8) The thermal probe was brought again out of contact at the same distance from the sample surface in order to compare the thermal signals out of contact before and after the point measurements. We repeated this procedure 10 times.

The method was applied to a series of bulk samples with known thermal conductivity (PMMA, pyrex, Si, SiO_2, Ti, Zn, Cu, AlO_3, Ta, AlN, LiF, ZnO_2, Ge, Cu). For each sample we measured the voltage difference $\Delta V_{sam.} = V_{in,con} - V_{out,con}$, where $V_{in,con}$ and $V_{out,con}$ are, respectively, the output voltage of the probe in and out of contact with the sample. The $\Delta V_{sam.}$can be directly related to the thermal contact resistance. The measurements performed in ambient air conditions ($T = 24\ ^0C$) in five consecutive days. A reference material (i.e. Si) was measured each day for monitoring deviations of the measured values and allowing the correction of the values if needed.

By plotting the $\Delta V_{sam.}$ versus different calibration samples thermal conductivities, a calibration curve can be obtained for different probe geometries. Figure 6 shows the measured $\Delta V_{sam.}$ for each sample as a function of the sample thermal conductivity for a specific probe geometry. Each point is obtained by averaging ten consecutive point contact measurements and the error bars represent the dispersion of the values. As we observe with this method, the double-wire Pt probe shows a large range of sensitivity to the variation of the thermal conductivity. However, Ti, Ta, and AlO_3, show larger dispersion of the values taken at different point measurements than the other samples. A possible explanation is the higher RMS roughness on these samples. It's worth mentioning that as the heated tip approaches the surface, the tip heats the surface even before the contact is made. Therefore there is a gradual heat increase in the heat dissipation thermal signal up to the physical contact point. This behaviour of the thermal signal indicates that when the tip is in contact with the surface, the area around the contact point is already preheated by the approaching thermal probe at certain distance. This is the main disadvantage working in ambient SThM environment, where the conduction through air might be misleading in the interpretation of the thermal respone[41,42]. All the heat transfer mechanisms contributed in the thermal response of the SThM probe in ambient environment are described below.

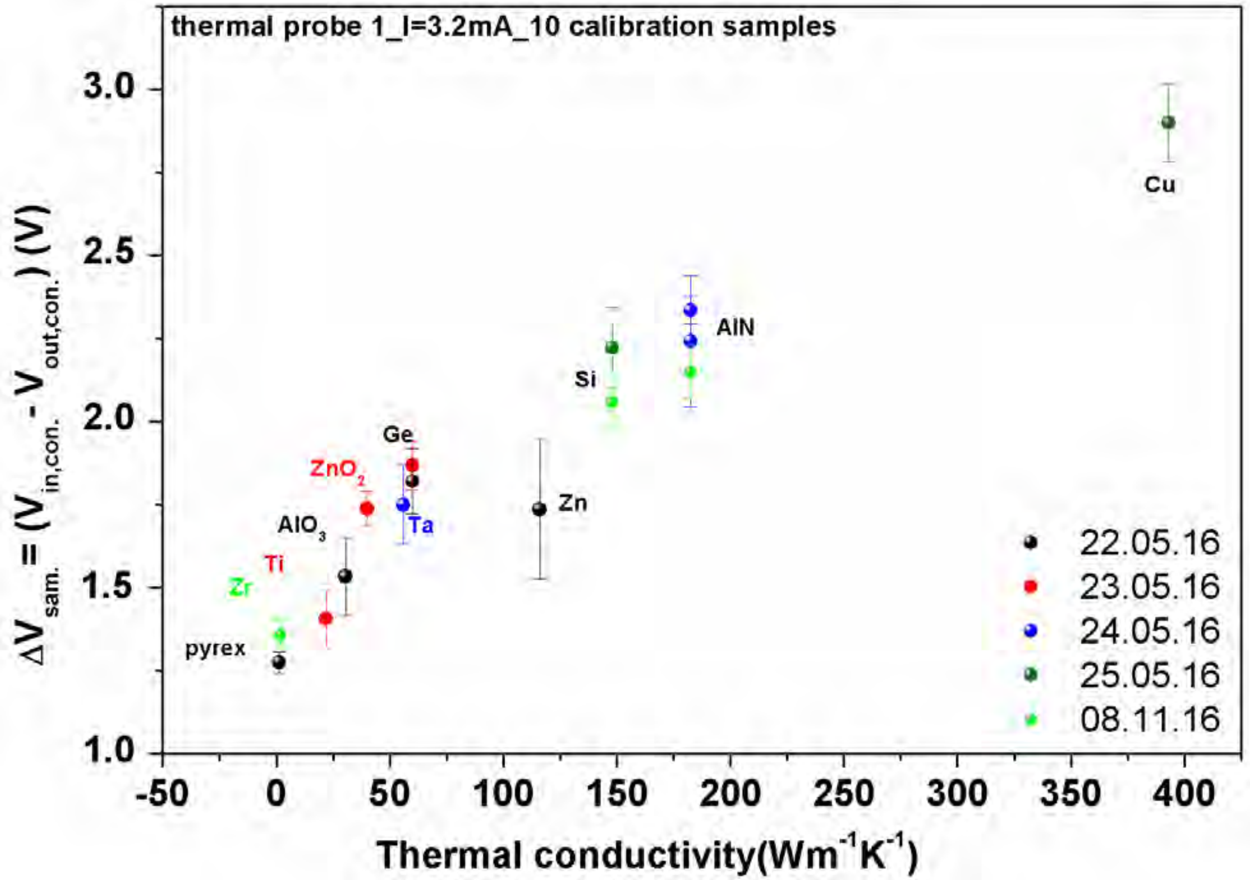

Fig. 6 Sensitivity of the dual-wire thermal probe in bulk materials

Heat transfer mechanisms

Different heat transfer mechanisms contributed in the probe–sample thermal conductance, such as heat conduction through the tip-sample contact (G_{sol}), heat conduction through air (G_{air}), heat conduction through the water meniscus (G_w) and thermal radiation (G_{rad}). Consequently, we can write the total thermal conductance between the thermal probe and the sample, G_{th}, as follow:

$$G_{th} = G_{sol} + G_{air} + G_w + G_{rad} \qquad (13)$$

where G_{rad}, G_w, G_{air}, G_{sol} are the thermal conductances due to radiation, liquid meniscus, air and mechanical contact[41], respectively. Under ambient SThM environment, the heat transfer through thermal radiation ($G_{rad.}$) is much smaller than the ones of other mechanisms due to the very small heated

area, thus usually is neglected[42,52]. For a quantitative estimation of the radiation heat transfer, ultra-high vacuum environment (pressure $\sim (10^{-8} - 10^{-9})\, mbar$) in order to eliminate conduction through water meniscus and conduction through the air is required. Similarly, to quantify experimentally, the percentage of heat which is transferred through the mechanical contact, G_{sol}, we need firstly to determine the radius of contact area and secondarily to work under vacuum conditions,[41,42,52] where the dominant heat transfer mechanisms are the thermal radiation and the heat conduction through the tip-sample contact. According to recent reports, [41,53] for specific probe geometries and relative high heating temperatures ($100\ ^0C$), the heat transfer due to liquid conduction, G_w, is one order of magnitude smaller than the conductance through air, thus can be neglected.

On the other hand the tip-sample air conduction in ambient environment, which depends on the size of the heated region, cannot be neglected.[41,54] Neglecting conductances due to radiation and liquid meniscus and considering the scanning probe in contact with the sample, the thermal interaction is a function of both, the air conduction and the heat conduction across the tip-sample contact. Both of these conduction mechanisms can potentially be dominant depending of the geometry of the heated tip. In the dual wire Pt probes the contribution of the air conduction to the total conductance was measured experimentally by approaching the tip very close to a Si substrate surface (few nm). We found that less than 30% of the acquired signal is coming from the conduction through air. This relative low percentage of contribution from the air conduction in Pt probes compare to other probes[41] is probably due to the particular position of the heat source, which is localized at the very end of the Pt wires (see Fig. 4d).

Next we show with finite element method (FEM) simulations that the temperature distribution in the Pt probe starting from the end of the junction decays exponential, confirming the localized heat source of the Pt probe. Note that this percentage depence on the materials thermal conductivity under investigation. In order to eliminate the conduction through air, which seems to be the most problematic issue in ambient SThM environment, measurements in vacuum conditions are required.

Temperature distribution in the thermal probe - FEM simulations

Here we study the thermal transport in our probes by using a finite element simulations based on COMSOL Multiphysics. First, we estimate the thermal resistance of the probe in vacuum (R_p) and in air (R_{pr}) using a 3D model that simulates the temperature distribution along the Pt wires and the cantilever material. Taking into account the length of the uncovered Pt wires ($L_t = 1.2\ \mu m$), their thermal conductivity ($k_t = 71.6\ Wm^{-1}K^{-1}$), the tip radius of the Pt junction ($r_t = 50\ nm$), the length of the cantilever($L_c = 150\ \mu m$) and its thermal conductivity ($k_c = 1.5\ Wm^{-1}K^{-1}$), we obtain $R_P = 2.5 \times 10^6\ K\ W^{-1}$ and $R_{pr} = 1.7 \times 10^6\ KW^{-1}$. We can then obtain the thermal resistance of the heat flowing from the probe to the surrounding air ($R_{P(air)} = 6.5\ \times\ 10^6\ KW^{-1}$) by taking the equivalent of the thermal resistance network formed by the parallel R_P and $R_{P(air)}$:

$$R_{pr} = \frac{R_P R_{P(air)}}{R_P + R_{P(air)}} \quad (14)$$

In Fig. 7 are shown the three dimensional (3D) geometry of one representative thermal probe and its temperature distribution, respectively, for a given power generated at the Pt junction.

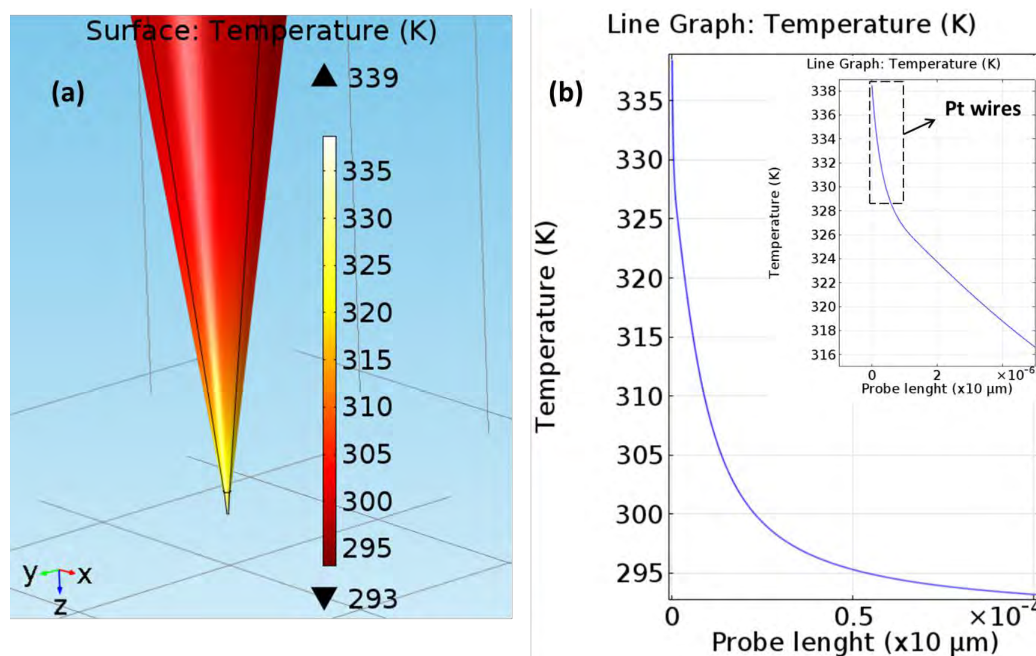

Fig. 7 (a) The three dimensional (3D) geometry of the thermal probe and (b) the temperature distribution from the nanometer-scale junction of the Pt wires until the glass nanopippete.

SThM measurements in ultra-high vacuum environment

Control of the scanning environment is particularly needed to minimize parasitic heat flow between the scanning probe sensor and the sample, for example via air conduction as discussed previously, and increase the thermal spatial resolution. Next, we briefly describe a vacuum-based thermal microscope and its principle of operation that has been used during my research stay in the University of Lancaster (ULANC). More details related with the experimental setup can be found elsewhere.[36]

The experimental setup was based on SPM system encased in a chamber that can be evacuated. A turbo-molecular pump together with an ion pump is used to pump vacuum levels of approximately $10^{-7}\ mbar$. The turbo pump was shut down during the experiment in order to avoid mechanical excitation of the microscope and electrical interferences noise of the pump control electronics on our measurements. The thermal microscope is suspended on springs using magnetic dampers, thus sufficiently isolated against mechanical excitations. The cantilever motion during a regular contact mode AFM operation is controlled by a laser beam deflection system. Using specific thermal probes (described below) measurements can be performed on selected spots of the investigated sample surface by following either the deflection of the cantilever supporting the nanoscale tip or the tip electrical resistance during an active or passive mode probe operation. Therefore, these probes can be used to study both thermal and mechanical properties of materials.

For thermal measurements, a pre-calibration of the thermal probe is required in order to correlate the probe electrical resistance with its temperature assuming that all electrical power dissipated leads to an increase of the heater temperature. The thermal calibration of the probes performed using a temperature stabilized Peltier hot/cold plate at several temperatures from room temperature to 120 ^{0}C. The calibration took place outside from the SPM. The linear dependence of the probe resistance versus probe temperature is shown in Fig. 8. Then, for dynamic measurements, a voltage excitation (square voltage pulse) is used to induce Joule heating in the probe by a function generator. The tip resistance (and correspondingly its temperature) is measured with a modified Maxwell bridge which is biased by a composite signal $V_{in} = V_{AC} + V_{DC}$ and balanced for both in-phase and out-phase

components using resistors and capacitors. The DC component is used to Joule heat the probe, while the smaller AC component at frequency around 90 kHz is applied for measuring with the aid of a lock-in amplifier, the resistance and, therefore, the temperature of the sensor.

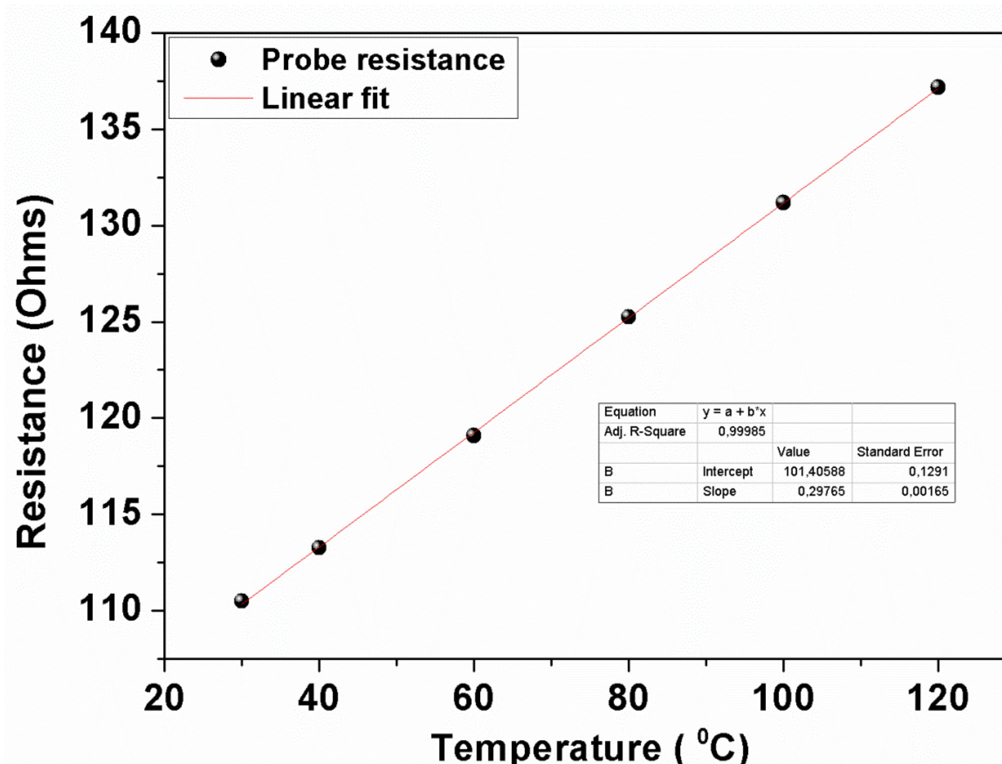

Fig. 8 Calibration of the probe - linear dependence of probe resistance vs probe temperature.

Doped Silicon resistive probes

The doped Si resistive probes consist of two micrometric legs with high doping level and a low doped resistive element platform. The electrical resistance of this probe at 300 K is $R_{pr(0)}^{el} = 1456\ Ohms$. A tip of a nanoscopic radius curvature ($(5-10)\ nm$) with a pyramidal shape is mounted on top of the resistive element. According to the geometry of the probe, a thermal spatial resolution of 10 nm can be achieved. The spring constant of these kind of cantilevers vary by their dimensions ($(0.1-3)\ Nm^{-1}$). A SEM picture of a doped Si resistive probe is shown in Fig. 9.

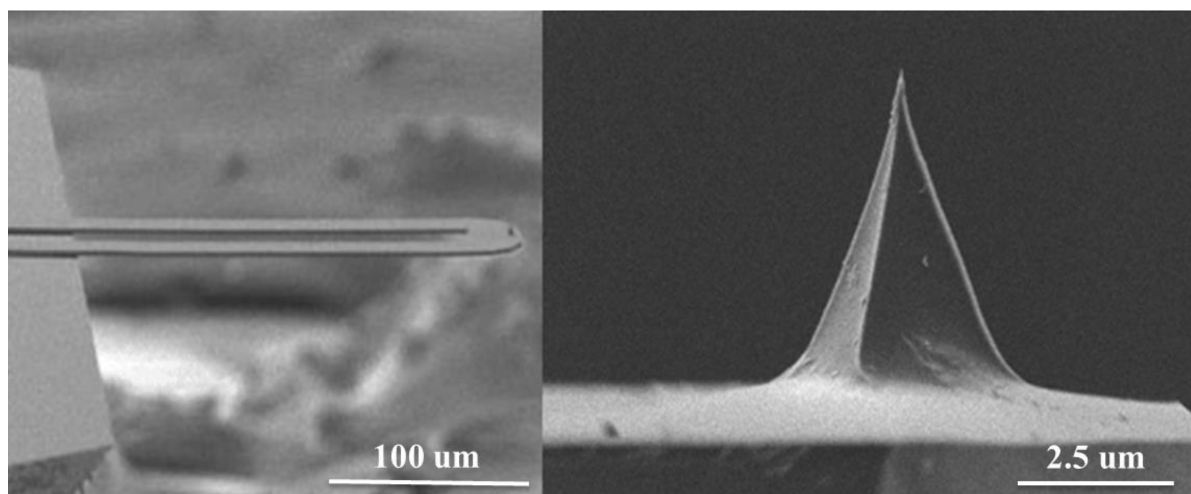

Fig. 9 SEM image of a typical Si-doped SThM probe.

SThM probes	Environment	Operation Mode	Current	Spatial resolution	Measured parameter
Pt resistive probe	Ambient	Tapping mode	DC	100 *nm*	Electrical resistance
Si-doped resistive probe	Vacuum	Contact mode	DC/AC	sub-20 *nm*	Electrical resistance

Table I Comparison between the two SThM resistive probes.

2.2 Two Laser Raman Thermometry (2LRT)

This contactless optical technique is based on the concept of Raman thermometry, however, with the decisive difference that heating of the sample and probing of the temperature are decoupled by using two spatially independent lasers. This method overcomes the main drawbacks of the single laser Raman thermometry technique as discussed previously (chapter 1). The 2LRT we describe below is suitable for thermal mapping with diffraction limited resolution and particularly appropriate for the determination of the thermal conductivity of suspended 2-dimensional structures. Therefore 2LRT can be applied in any material in membrane format, where the absorbed power can be considered uniform along the thickness, exhibiting a detectable temperature-dependent phonon Raman scattering signal. The two-laser Raman thermometry technique is shown schematically in Fig. 10.

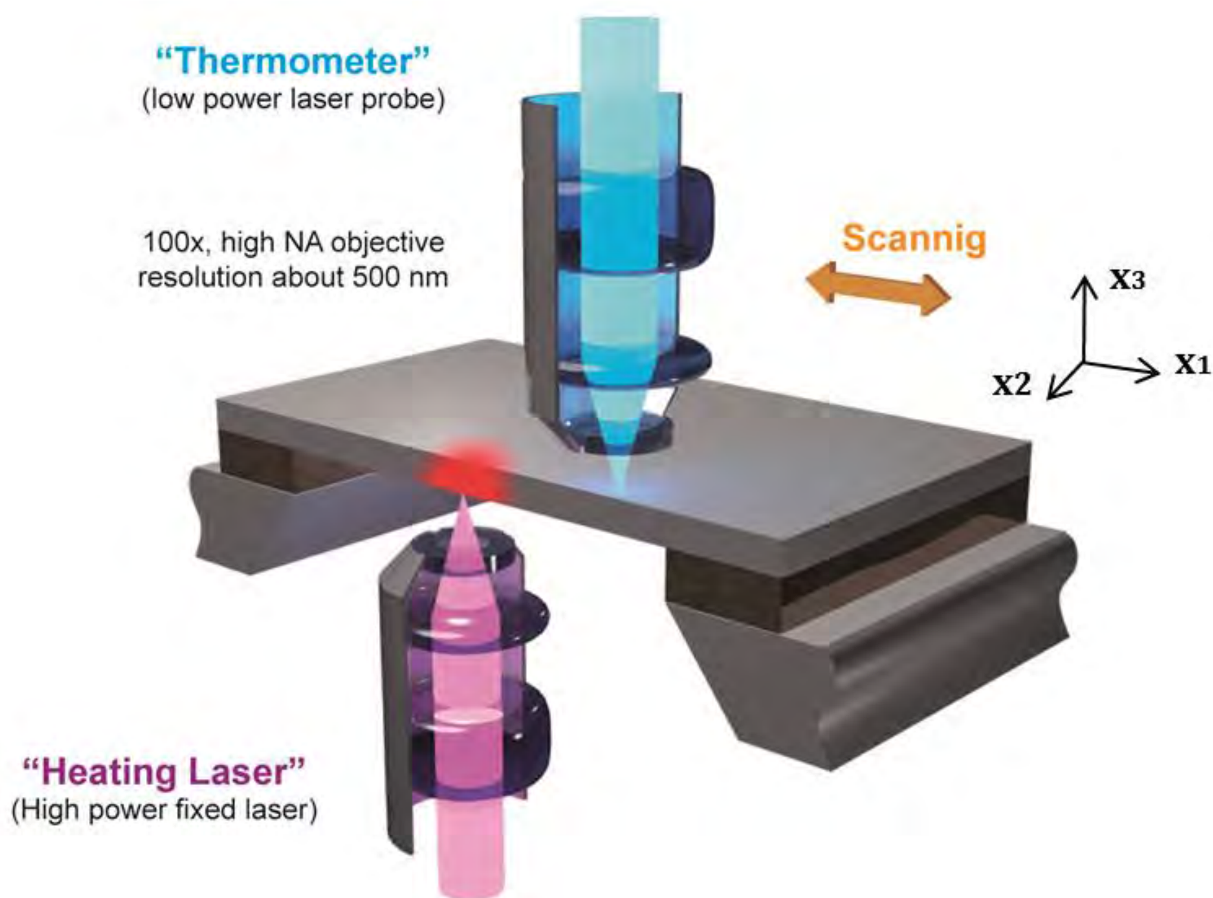

Fig. 10 Schematic of the 2-laser Raman thermometry experimental setup.

The basic idea of this method is to use two lasers of different wavelengths: one high power laser in the centre of the membrane, which serves as a steady state heater (Cobolt Samba lasing at 405 nm), and another, low power, probing laser (Spectra Physics 2018 lasing at 488 nm), which measures the Raman shift along a line on the membrane. Light emitted by the fibre-coupled laser operating at 405 nm is focused on the sample from the bottom by a long working distance microscope objectives (100× or 50× and $NA = 0.55$) and it works as a Gaussian heat source with a waist size of about 2 μm. The absorbed power P_0 is measured on site (see Fig. 10) for each sample as the difference between incident and transmitted plus reflected light intensities probed by the calibrated system based on a cube non-polarizing beam splitter with an error of $\Delta P_0 = 2\%$. The second laser beam with wavelength of 488 nm, which is focused on the sample from the top by a second microscope objective (50× and $NA = 0.55$), works as a temperature probe. The probing laser power is kept to the minimum in order not to heat the sample. The sample is mounted in a cryostat (Linkam THMS 350EV), which is fixed in a motorized scanning stage together with the heating beam unit. The stages fixed in the vertical direction(x_3) and allows scanning in the horizontal (x_1x_2) plane in steps as small as 0.2 μm. The latter value, together with the probe beam spot diameter defined as $1.22\lambda_p/NA = 1.08\ \mu m$, results in the total spatial uncertainty of the experiment $\Delta r = 0.55\ \mu m$.

Taking as example silicon, the spectral position of the longitudinal optical phonon (LO) ($\Delta\omega_R(300\ K) = 520.7\ cm^{-1}$) is used as a temperature reference. Figure 11a displays a calibration curve obtained controlling the bath temperature in the cryostat, from which the temperature coefficient between 300 and 870 K was determined as $dT/d\,\Delta\omega_R = 43.43\ \pm 0.05\ K/cm^{-1}$. Figure 11b shows exemplary Raman spectra and their Lorentzian fits obtained in a 200 nm thick Si membrane at different relative positions r between the heating and the probe lasers. The Si LO Raman peak redshifts as the position of the probe laser moves closer to the heating source (at 0 μm). The spectral resolution of the Raman spectrometer is 0.5 cm^{-1}. The total temperature uncertainty was calculated using the error of the temperature coefficient and standard error of the Lorentzian fit performed for each point. The temperature resolution with this technique depends on the investigated material (e.g. 2 K for Si).

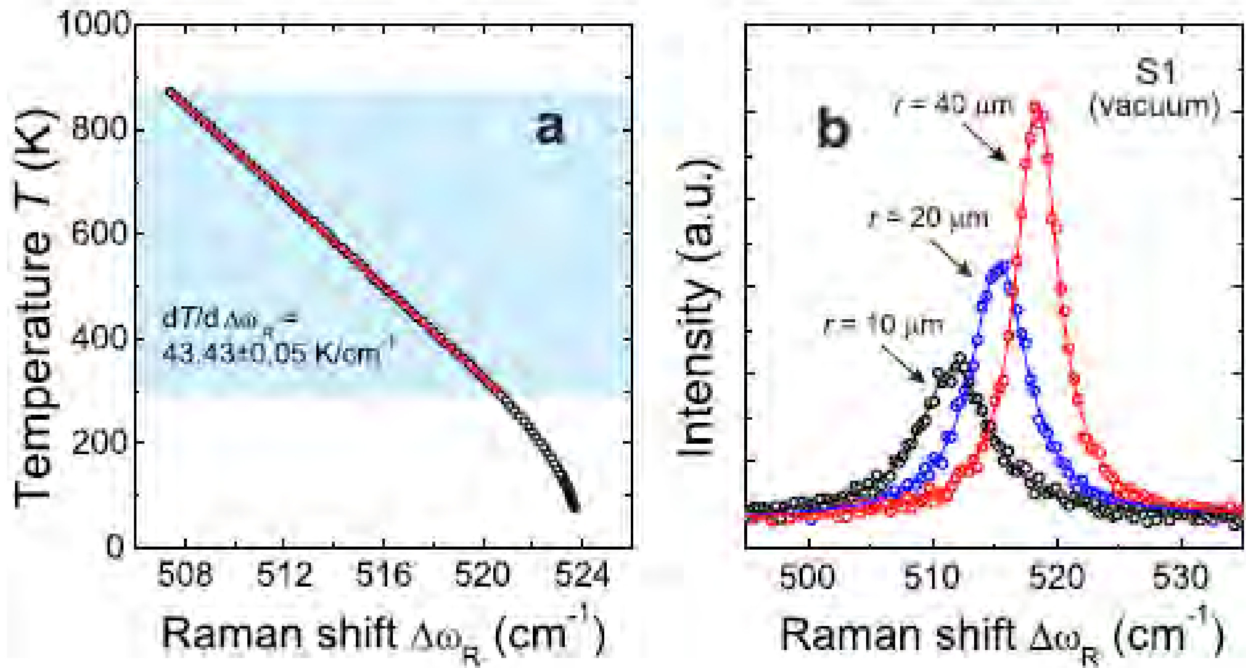

Fig. 11 (a) Temperature calibration of the Si LO phonon frequency. (b) Representative Raman spectra obtained in vacuum for Si membrane at different distances r from the heating spot (at 0 μm).

Analytical model of the temperature distribution and thermal conductivity deduction

An analytical model has been followed in order to determine k as a function of temperature. To do so we assume the temperature gradient established by the heater to be zero across the membrane in the x_3 direction and diffusive in-plane heat flow, for which the radial heat is governed by the Fourier's law:

$$\frac{P_0}{A} = -k(T)\,\frac{dT}{dr} \qquad (15)$$

where P_0 is the absorbed power, A the cross sectional area of the heat flux, k is the thermal conductivity and T the temperature. For a given membrane thickness t, the cross sectional area is $A = 2\pi rt$. Then, taking $r\,dT/dr = dT/dlnr = \xi(r)$ we obtain the following expression for the thermal conductivity:

$$k(T) = -\frac{P_0}{2\pi t \xi(r)} \quad (16)$$

Consequently, knowing P_0 and t the value of $k(T)$ can be extracted from the logarithmic temperature profile $T(lnr)$. In the case of a temperature independent thermal conductivity in the temperature range under study, the thermal field decays as $T(r) \propto lnr$ in the diffusive limit and k is directly obtained from eq. (16) and the slope of the linear fit of the logarithmic temperature profile. In this case, the temperature distribution in the membrane is gives as follow:

$$T(r) = T_o - \frac{P_0}{2\pi t k_0} ln(r/r_0) \qquad (k = k_0) \qquad (17)$$

When the temperature dependence of the thermal conductivity has to be taken into account, assuming that $k(T)$ of the membrane resembles the behaviour of bulk Si at high temperatures ($k(T) = aT^{-\beta}$), the Fourier's law gives us the follow function for the temperature distribution:

$$T(r) = \left(B - \frac{P_0(1-\beta)}{2\pi t a} lnr\right)^{1/(1-\beta)} \qquad \big(k = k(T)\big) \qquad (18)$$

where B is a constant of integration while the fitting parameters β and a determine $k(T)$. Figure 12 shows two examples of the temperature distribution in a 200 nm thick Si membrane. For small temperature gradients the thermal conductivity does not depend on temperature and the experimental data (black circles) are fitted with a linear function. In the case where the thermal conductivity is temperature dependent, we fit eq. (18) to the experimental data points (red circles). We point out that this procedure is valid for a data range starting at a distance of a few micrometres from the central point $r = 0$ due to the Gaussian shape of the heating source. Therefore the 2LRT method together with the model described here allowed us to obtain the temperature dependence of the thermal conductivity of Si-based suspended quasi-2D structures in the high temperature range ($400 - 1000\ K$).

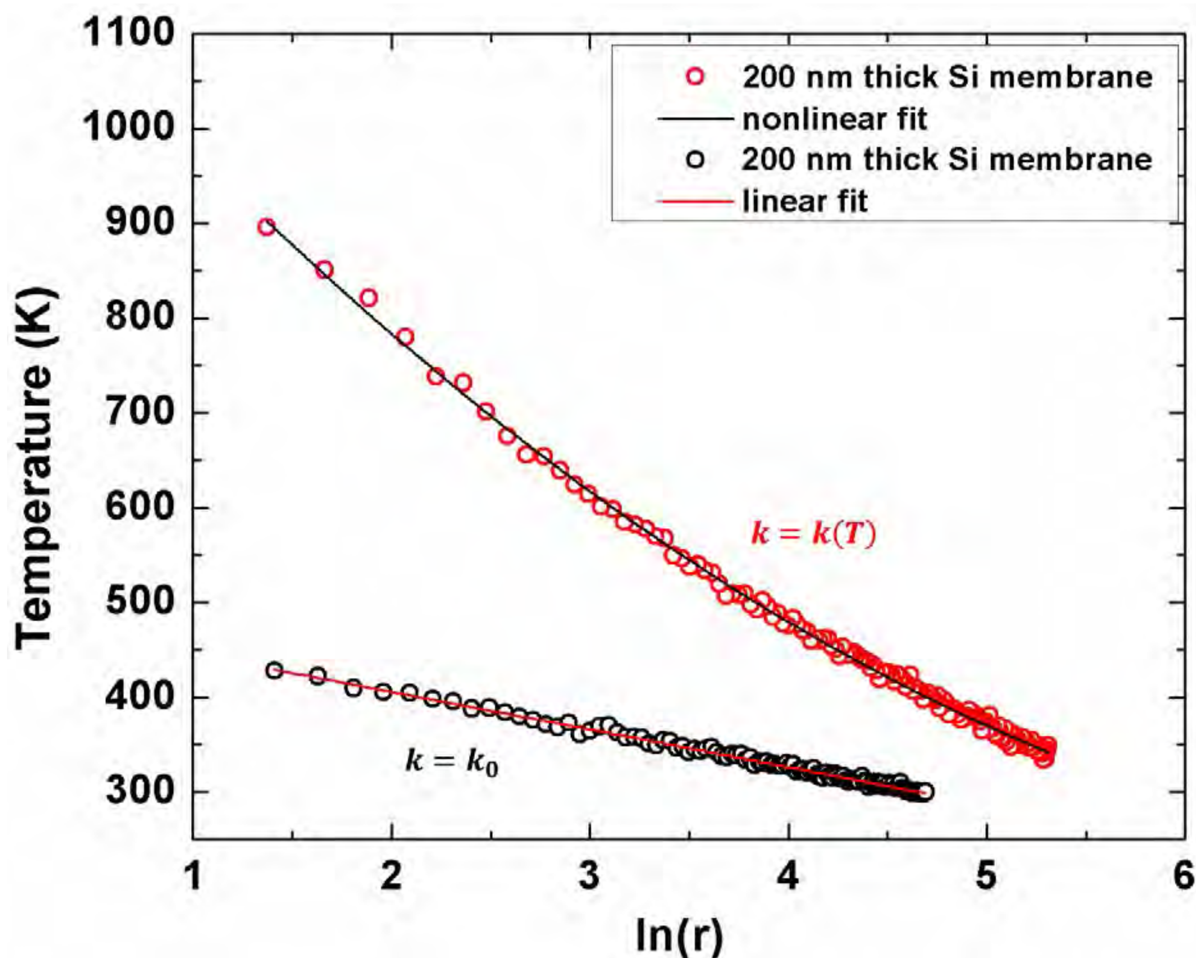

Fig. 12 Temperature profile examples in a 200 nm thick Si membrane.

2.3 Energy Dispersive X-ray Spectrometry (EDS)

The principle of the technique is based on the X-ray spectrum emitted by a solid sample bombarded with a focused beam of electrons. In principle, all the chemical elements from a composition structure can be detected to obtain a localized chemical analysis. A qualitative analysis is quite straightforward since involves only the identification of the lines in the X-ray spectra, which correspond to specific chemical elements. For a quantitative analysis, the determination of the concentrations of all the elements has to be performed by measuring the line intensities for each chemical element in the sample. The same elements in calibration samples of known composition have to be measured in advanced. By monitoring the intensity of each selected X-ray line, element distribution images or composition maps can be produced. X-ray

intensities are measured by counting photons and the precision obtainable is limited by statistical error. Uncertainties in the compositions of the calibration sample and errors in the various corrections which need to be applied to the raw data can decrease the analytical accuracy of this method, which is commonly $\pm 2\%$. The spatial resolution depence on the penetration and the spreading of the electron beam in the sample. This technique is used to study the spatial distribution of the elemental composition of alloy nanowires and BCP films (see chapters four and five). The samples analyzed in a Transmission Electron Microscope (TEM) with an X-ray spectrometer attached. A high spatial resolution of 1 nm achieved in this case. Particularly, high resolution transmission electron microscopy (HRTEM) and high angle annular dark field scanning TEM (HAADF-STEM) images were acquired at 200 kV on an FEI Tecnai G2 F20 microscope. Energy dispersive X-ray (EDX) spectra and EDX-STEM maps were obtained with an EDAX super ultra-thin window (SUTW) X-ray detector. In addition, in order to be more sensitive in the detection of light chemical elements, composition maps using the Electron energy-loss spectroscopy (EELS) were acquired. The EELS maps acquired by measuring the distribution of the electrons as a function of energy loss behind the sam

3
Nanomembranes

Present silicon technology provides single crystal films and membranes with thicknesses on the order of 10 nm and below. Along the years, the thermal studies on such structures have shown a reduction of the thermal conductivity consistent with the decrease of the characteristic size. Although the lowering of thermal conductivity is detrimental for heat dissipation processes in nanoelectronic devices, it becomes advantageous to increase the figure of merit (ZT) of Si and turning it as a promising material for thermoelectric applications. It is widely accepted that, for submicrometre thicknesses and down to 20 nm, the reduction of the in-plane thermal conductivity is mainly determined by the shortening of the phonon mean free path due to the diffusive scattering of phonons at the boundaries.[55-58] In this case an analytical model[57-59] that adopts the phonon bulk properties and includes the boundary scattering by a conductivity reduction factor is shown to match the experimental trend of systematical reduction of the thermal conductivity as the thickness of the film or membrane decreases. However, the studies on the influence of thickness on $k(T)$ above room temperature are scarce only for temperatures up to 450 K[60] in supported thin films for few thickness values, leaving the higher temperature range almost unexplored.

Membrane-based structures with periodically arranged holes have shown coherent features, such as a modified dispersion relation with band folding, and therefore they can be termed as truly phononic crystals (PnCs). In PnCs the heat transport is expected to be influenced by the modified dispersion relation, when the wavelength of the phonons involved in the heat transport is commensurate to their characteristic sizes. In principle, the approach to reduce the thermal conductivity would be linked to the

decrease of phonon's group velocity and lifetime in an extended range of frequencies. In reality, the results of Brillouin light scattering (BLS) from samples with characteristic sizes in the order of few hundreds of nm have showed coherent effects,[61] but only in a relative low frequency range (up to tens of GHz), which becomes relevant at very low temperatures, where most of heat is carried by long wavelength phonons.[62,63,64] There have been many works over the last years investigating the thermal transport in Si membranes with controlled structuring at room temperature, with some attributing the observed properties, such as a strong reduction of the intrinsic thermal conductivity, to PnCs behaviour,[65] while others dispute this explanation.[63,66-68] Since there is no conclusive understanding whether the reduction of the thermal conductivity is caused entirely by classical diffuse boundary scattering, or there is a contribution of coherent effects, we have used the term *periodic porous Si membranes* instead of *PnCs* when referring to these structures in the context of thermal properties at room temperature and above.

3.1 Si membranes: Thickness dependence of the thermal conductivity at high temperatures

In this section present the study of the temperature dependence of the thermal conductivity in crystalline membranes with thicknesses ranging from 8 to 1000 nm, and in the temperature range from 400 to 1000 K, using 2LRT. The temperature dependent thermal conductivity $k(T)$ was inferred from the analysis of the thermal field as previously detailed in chapter 2. Figure 13 displays $k(T)$ for crystalline Si membranes with thicknesses of 200, 100, 70, 42, 30, and 8 nm as well as the case of bulk Si measured by Slack and Glassbrenner.[69] The data points from bulk Si are fitted using $k \propto T^{-\beta}$ (solid line obtained by taking $\beta = 1.3$), which is the usual behaviour for most single crystal semiconductors at high temperatures. In membranes, a clear reduction of the thermal conductivity and of its dependence on temperature is observed compared to bulk Si. In the case of the thinnest membrane, $t = 8\ nm$, k reaches the lowest value measured of $8 \pm 2\ Wm^{-1}K^{-1}$ and the temperature dependence is suppressed. The strong temperature dependence of k in bulk Si at high

temperatures is attributed to the phonon-phonon Umklapp processes, therefore the gradual softening of this trend, as seen in Fig. 13, indicates that other mechanisms than phonon-phonon scattering become increasingly dominant with decreasing thickness. The membrane thickness is the only parameter being changed in the set of high crystalline quality membranes studied in this work, thereby indicating that the most likely mechanism reducing the thermal transport is related to the sample boundaries. The phonon confinement effect, i.e, change of phonon dispersion relation, in the reduction of the thermal conductivity is seen to vanish for membrane thickness above 20 nm at room temperature.[70] Therefore, we can neglect it at the temperature range of our measurements.

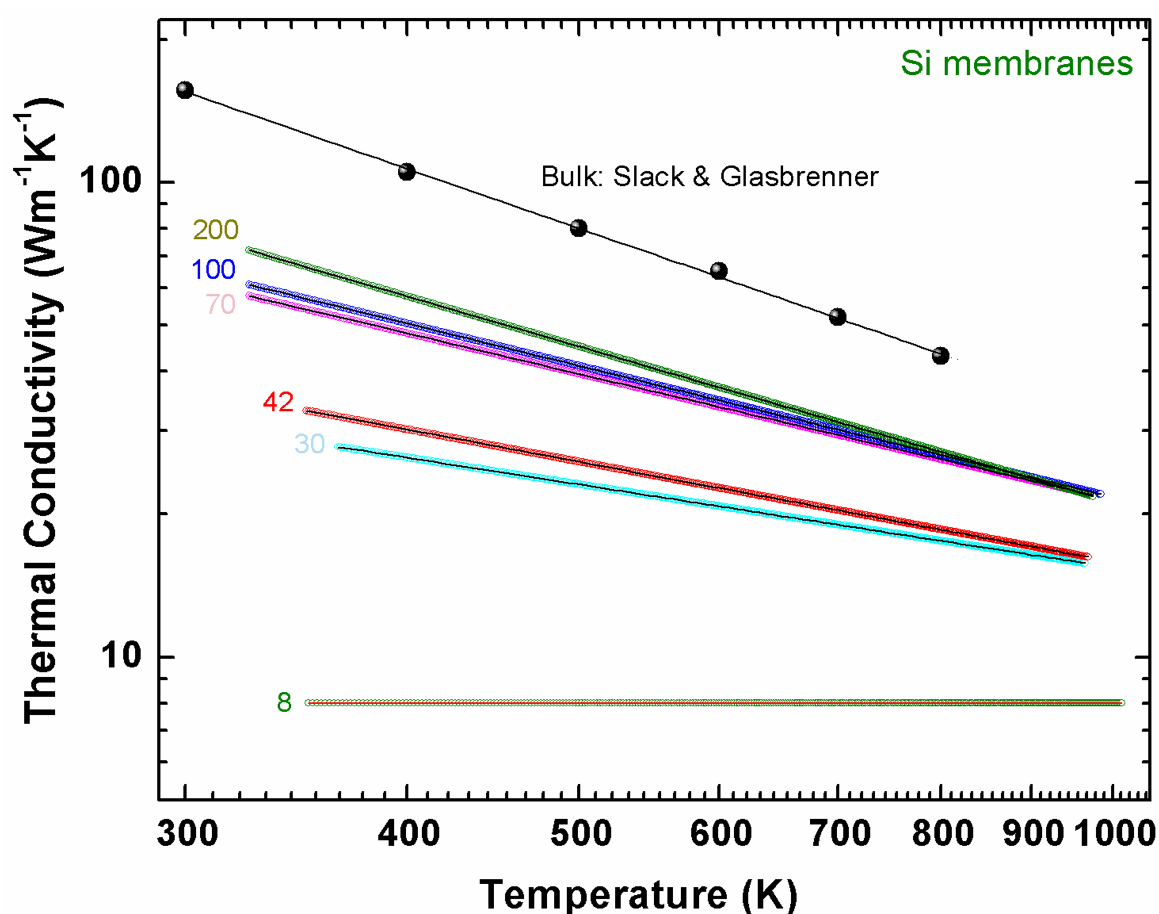

Fig. 13 Temperature dependence of the thermal conductivity for a series of crystalline Si membranes with thicknesses between 8 and 1000 nm, over the temperature range from 400 to 1000 K.

The dependence of $k(T)$ on thickness is revealed taking into account the exponent β in the function $k \propto T^{-\beta}$ for each curve in Fig. 13. Figure 14 displays the evolution of β for all membranes as a function of thickness. For each thickness we have added the value of the membrane to bulk thermal conductivity ratio at room temperature, i.e., $k_r = k/k_{Bulk}$ at $300\,K$. The rate of change of $k(T)$ spans from a value $\beta = 1.24$ for the thickest membrane ($t = 1\,\mu m$) approaching the bulk limit $\beta = 1.3$ (horizontal dashed line in Fig. 14), down to a value of $\beta = 0$ for the thinner membrane ($t = 8\,nm$). Here, the membrane thickness t is the limiting dimension, which, by determining the importance of the diffusive boundary scattering, obstructs to a large extent the propagation of phonons with mean free path, Λ, on the order or greater than the membrane thickness. Thus the contribution of these phonons to thermal transport will be significantly suppressed reducing the thermal conductivity. However, phonons with Λ longer than the film thickness might still contribute to the thermal conductivity provided that phonons wavevector directions are close to the direction of the temperature gradient. At high temperatures, the wavelength of phonons dominating the heat transport becomes shorter. Then, as the specular scattering is less probable, it is appropriate to assume diffuse transport.[71]

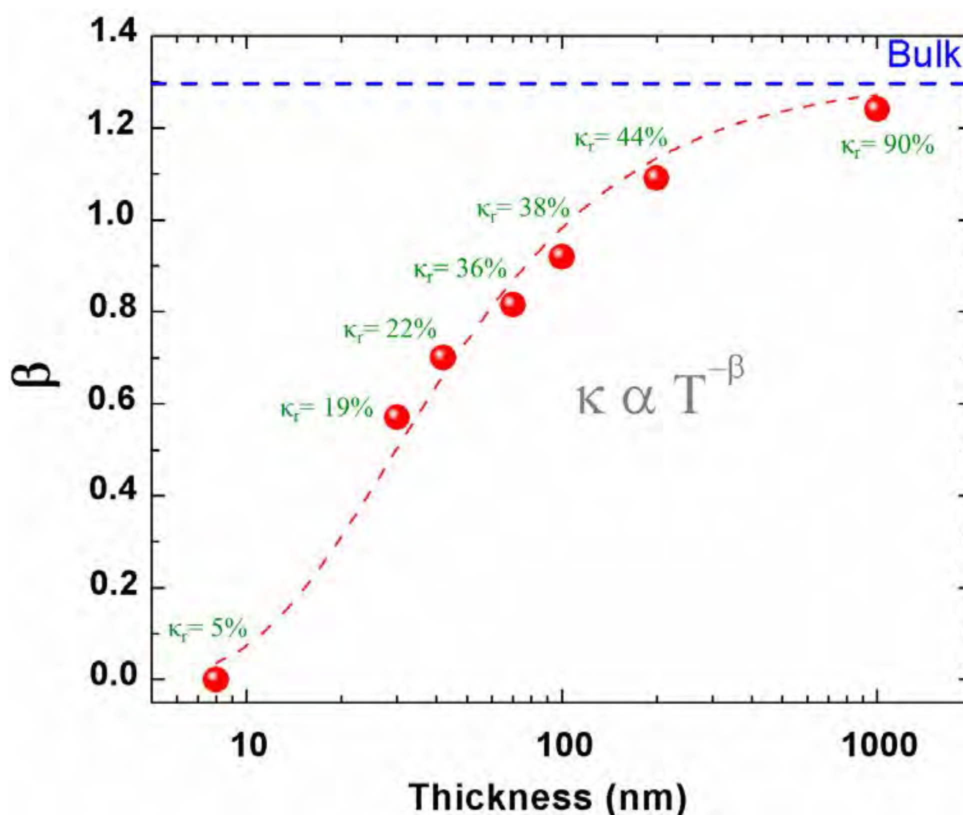

Fig. 14 Evolution of the exponent β as a function of the membrane thickness (red spheres). The value of the relative thermal conductivity k_r at room temperature is indicated at each membrane thickness.

From Fig. 14, qualitative remarks regarding the mean free path of the dominant phonons can be inferred. Since the thermal conductivity of the thicker membrane shows a reduction of only a 10% and an exponent β close to the bulk value, this implies that heat transport in the range between 450 and 1000 K is mostly contributed by phonons with Λ as large as 1 μm. The case of the 200 nm thick membrane is particularly interesting since k is decreased by a 56% ($k_r = 0.44$), whereas the influence of dimensionality on the temperature dependence is small, i.e., $\beta = 1.1$. Therefore, we suggest that those phonons with Λ > 200 nm contribute substantially to the thermal conductivity with a rather small influence on its temperature dependence. The latter reflects the effect of phonon-phonon scattering in reducing Λ.

Finally, in Fig. 15a we display the thermal conductivity as a function of thickness for temperatures varying between 400 and 900 K. From this graph we can determine the thickness at which k reaches the bulk value at each temperature when the curves are relatively flat. Figure 15a shows that as the temperature increases this maximal thickness gradually shifts to lower values, namely, from a value of about 200 nm at 400 K to below 50 nm at 900 K. This effect originates from the temperature dependence of the phonon mean free path i.e., Λ decreases with increasing temperature.[72] In other words, k becomes gradually more insensitive as temperature increases unless the thickness of the membranes is close to the Λ of the phonons responsible for most of the heat transport. The curves in Fig. 15 were phenomenologically fitted using an exponential expression, $k \propto e^{(-\delta/d)}$, where δ is a fitting parameter.

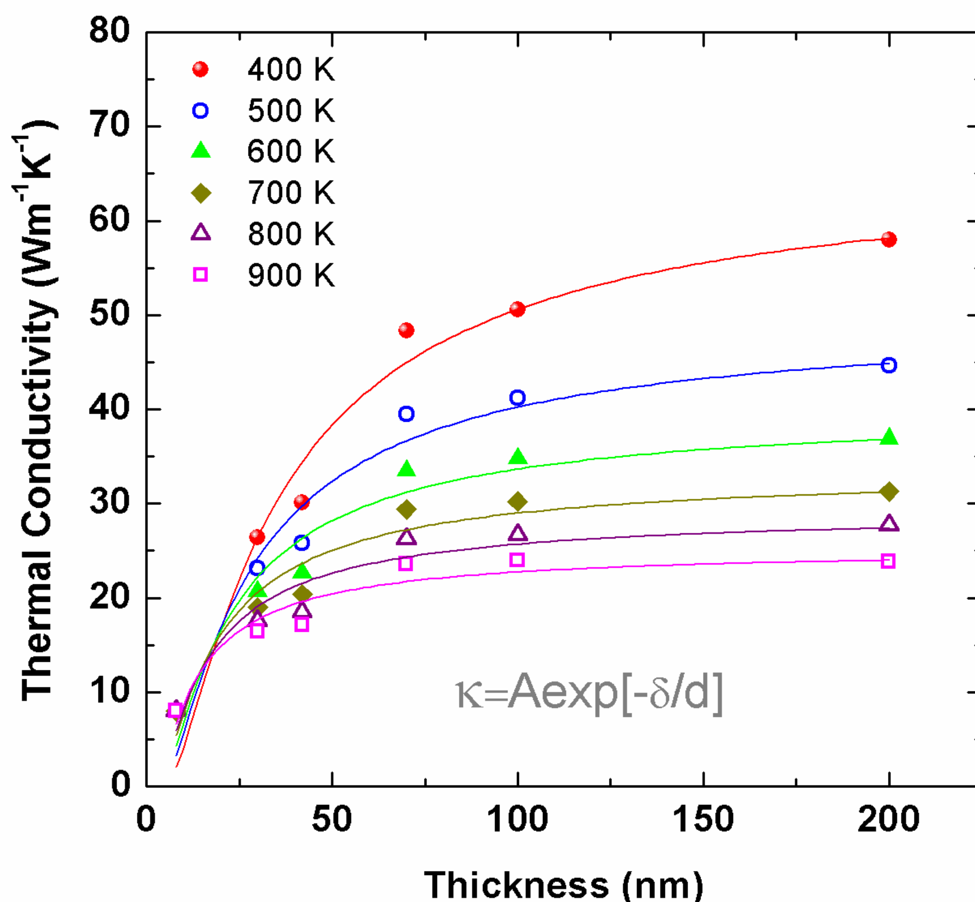

Fig. 15 Thermal conductivity as a function of membrane thickness for different temperatures.

3.2 Heat transport tuning in Si membranes patterned with holes

Samples

Three periodic porous membranes were fabricated with a square lattice of cylindrical holes of similar diameter of about $d = 135\,nm$ and different lattice constant ($a = 300,\ 250$ and $200\,nm$) (labelled as S1, S2 and S3). For the purpose of assessing whether the order on the array of pores have any effect on the thermal properties, we fabricated two samples (labelled S4 and S5) with equal hole diameter and filling fraction of about $d = 175\,nm$ and $a = 300\,nm$ and $\varphi = 0.267$, respectively, with ordered (sample S4 with a=300 nm) and disordered (sample S5) hole pattern. The fabrication of the arrays of holes on the Si membranes (see Fig. 16a) was based on

electron beam lithography (EBL) and reactive ion etching (RIE).[73] As the basis and reference sample we used commercially available, single crystalline silicon (001), $t = 250\ nm$ thick membranes with a window size of $3.2\ x\ 3.2\ mm^2$ placed on a thick Si square frame. Figure 16b displays a schematic top-view of the sample designed to keep radial symmetry about the x_3 axis running through the heating spot. The heating island of a diameter of about 5 μm has no holes to avoid the diffraction of the heating beam and subsequent uncertainties in the absorbed power measurements. This island is surrounded by the periodic porous membrane with a total diameter of 100 μm. In general, the radial symmetry of the sample simplifies the measurements to a single line scan in the x_1 direction, which determines a temperature profile. Figures 16c,d show typical SEM images of the samples with a well visible heating island.

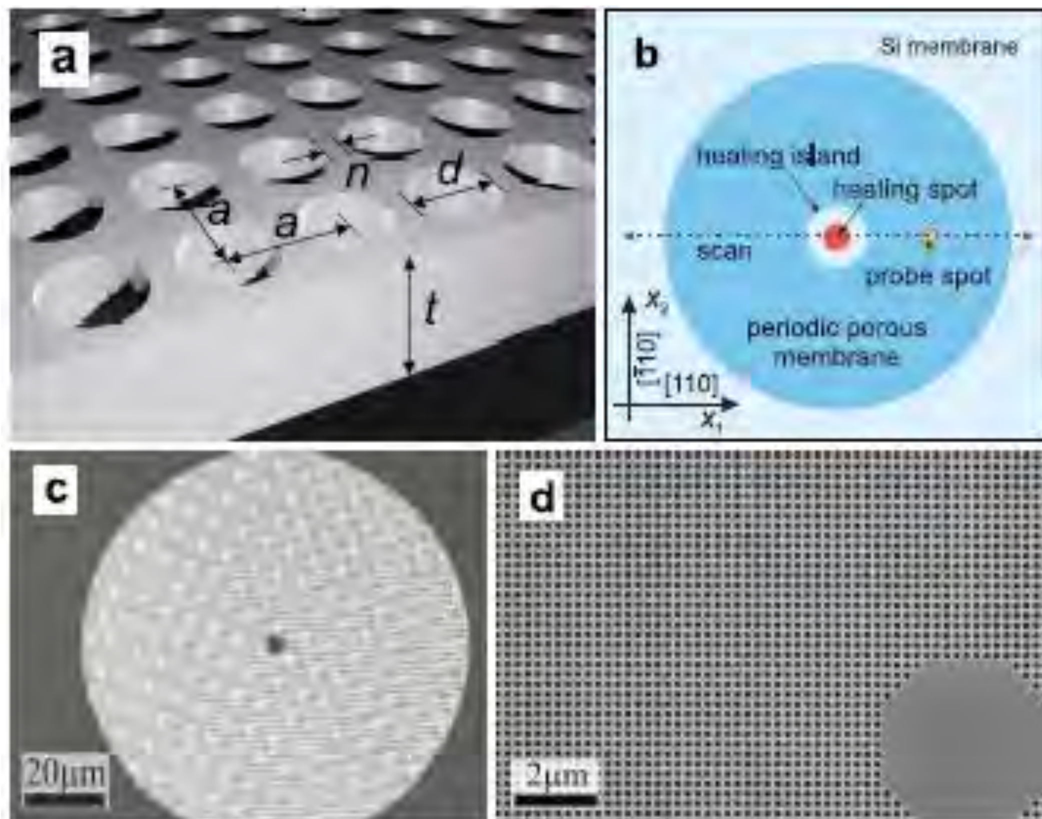

Fig. 16 (a) Schematic picture of the periodic porous membrane - square lattice of cylindrical holes in the free standing membrane, where $t = 250\ nm$ is the membrane thickness, d is the hole diameter, a is the lattice parameter and n stands for the neck. (b) Schematic illustration of the sample design. (c, d) SEM images of sample S2 with $a = 250\ nm$ and $d = 140\ nm$.

The samples S4 and S5 were fabricated in a similar way (Fig. 17a-c). In S5, however, disorder introduced by random displacements of the holes in x_1 and x_2 direction. The positions of the holes in the disordered lattice were defined by $p = p_0 \pm f \cdot s$, where p is the displaced hole position along the two in-plane axes, p_0 is the ordered lattice position, f is a random number between 0 and 1, and s is the maximum displacement, which was set to 45 nm. The level of disorder in percentage of the period $a = 300\ nm$ is then quantified by $(s/a) \cdot 100 = 15\%$. Figures 17d-f display schematic illustrations of the unprocessed membrane with a surface roughness of about 1 nm (d), the ordered lattice with a hole wall roughness of about 7 nm (e), and the disordered lattice with an average displacement of the holes from the ordered lattice sites of 22.5 nm in x_1 and x_2 direction (f).

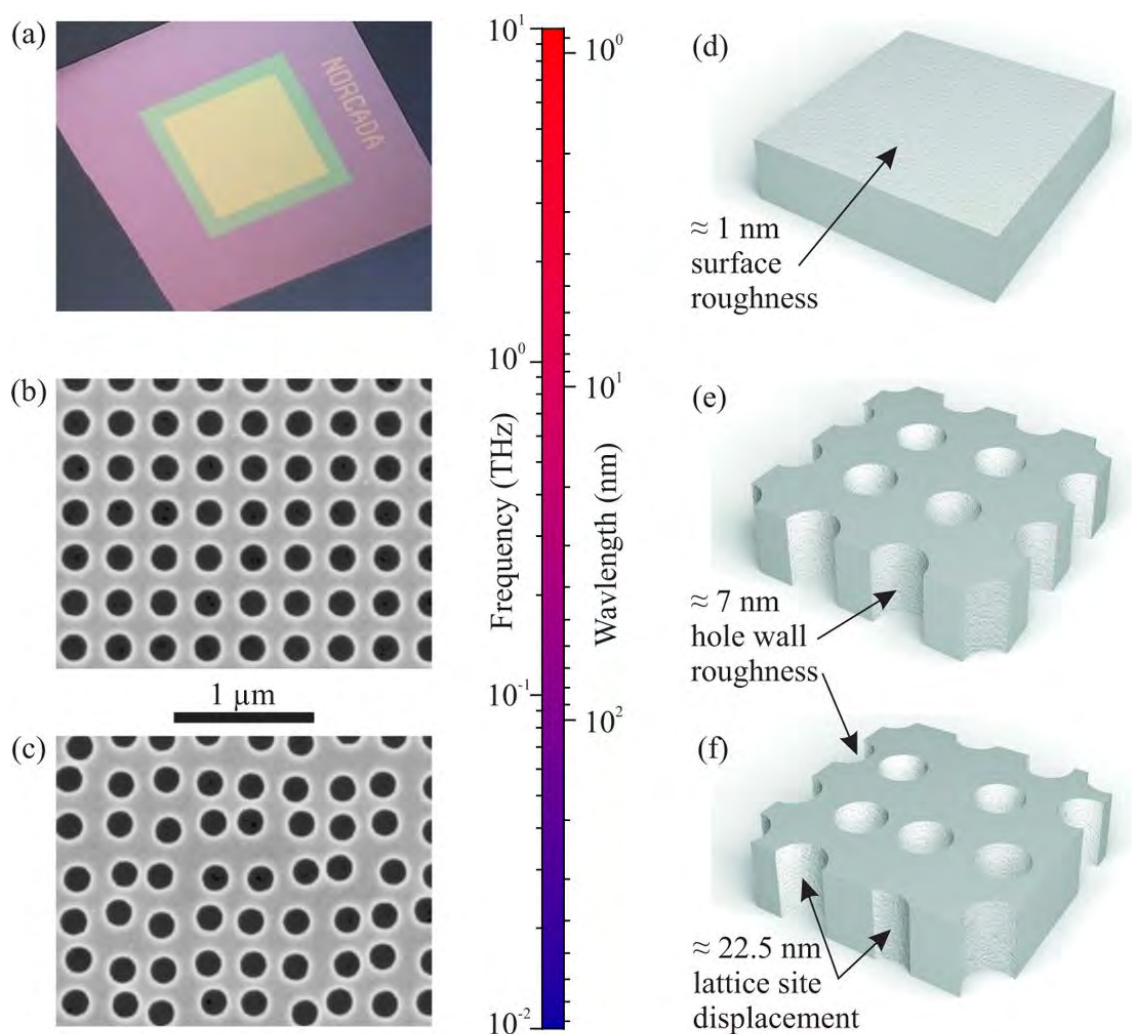

Fig. 17 (a) Optical image of a 250 nm thick Si membrane, (b) SEM image of the Si membrane with ordered 2D arrays of holes with hole diameter of 175 nm and pitch of 300 nm, (c) disordered 2D arrays of holes with equal hole diameter and filling

fraction $\varphi = 0.267$, (d) schematic of unpatterned membrane with surface roughness, (e) hole wall roughness in ordered 2D patterning, (f) combination of hole wall roughness and lattice site displacement in disordered 2D patterning.

Thermal conductivity of periodic porous membranes: Dependence on the feature size and temperature

Thermal conductivity of pristine membrane

Before going through the measurements performed on the porous membranes, we first characterize the bare membrane (sample S0) in order to establish a reference measurement for comparison purposes. Figure 18a displays two steady-state heat flow temperature profiles obtained at the same heating power $P_0 = 8.125\, mW$, but under different ambient conditions. The plots labelled vacuum and air correspond to the ambient pressure of 10^{-3} mbar and 10^3 mbar, respectively. These measurements were also performed in the porous samples to ascertain the effect of the air-mediated cooling discussed later. It follows from Fig. 18a that by applying a relatively small power to the membrane in vacuum, a temperature difference from 920 to 420 K is established over a distance of 500 μm which, as discussed in previous section, allows us to determine k as a function of temperature over a wide range by a single measurement. Figure 18b shows the temperature profiles in logarithmic scale, together with the fitted curve obtained to extract $k(T)$.

The obtained $k(T)$ is plotted in Fig. 19a and, assuming $k(T) = aT^{-\beta}$, extrapolated to close the ends of the $300 - 1000$ K range. As already reported previously, a large reduction of the thermal conductivity and its dependence on temperature with respect to bulk Si is clearly observed. From Fig. 18b we obtain $k_{mem} = 78 \pm 6\, Wm^{-1}K^{-1}$ for the pristine membrane at 300 K, which corresponds to a two-fold reduction of k with respect to bulk Si. This value is in good agreement with recent transient thermal grating measurements on Si membranes.[58] Furthermore, it is consistent with other existing data obtained for Si thin films of similar thicknesses by means of the harmonic Joule heating technique.[74]

Thermal conductivity of periodic porous membranes

As previously formulated for the case of the thin bare membranes (section 3.1), we use the temperature line scans and the corresponding temperature profiles in logarithmic scale to determine $k(T)$ for the periodic porous membranes. These are shown in Fig. 18c and Fig. 18d, respectively, for the case of the sample S3 (see Table II). For the measurements performed in vacuum, we notice that by heating with less power than for the pristine membrane, namely $P_0 = 0.41\ mW$, we create a similar temperature rise at $r = 0$. Simultaneously, the created temperature gradient covers a range of about 300 to 1000 K over a distance of only 50 μm. This suggests a reduction of k caused by the lattice of holes in the membrane. In principle this effect could result from volume removal, while the intrinsic material thermal conductivity might be preserved. Therefore, $k_{exp}(T)$ of the porous membranes determined from the experimental data and eq. (16) has to be scaled by a factor which takes into account the specific porosity of the membrane. This can be done by using a volume correction factor ε that can be obtained analytically or, more accurately, numerically by solving the diffusive heat transport model using FEM simulations.[62] Figure 18e shows a plot of ε as a function of the sample filling fraction φ obtained from FEM, which we use here, compared with two analytical expressions by Eucken[75] and later by Hashin and Shtrikman.[76] Once $k_{exp}(T)$ and φ of the porous membrane are obtained, we calculate the intrinsic thermal conductivity $k(T)$ from the formula $k(T) = k_{exp}\,(T)/\varepsilon(\varphi)$. It is worth mentioning that eq. (16) used to determine $k_{exp}(T)$ is valid when the radial symmetry of the temperature field is preserved. That symmetry is preserved for the pristine membrane as reports elsewhere.[25] In such a case the in-plane thermal conductivity of the membrane follows k of bulk Si in diffusive regime that is isotropic. This is not obvious for the periodic porous membranes with the in-plane structural anisotropy driven by the square lattice of holes. Nevertheless, in our case, the 2D thermal map obtained for the sample S1 and shown in Fig. 18f clearly demonstrates radial symmetry with no signature of the structure driven in-plane thermal anisotropy, and thus validates the use of eq. (16). We note that the probe laser spot measures an average temperature over its size, which comprises of several unit cells. In this way we obtain an effective k of porous membranes, which is the

thermal conductivity that would exhibit a homogeneous membrane in the Fourier approximation.

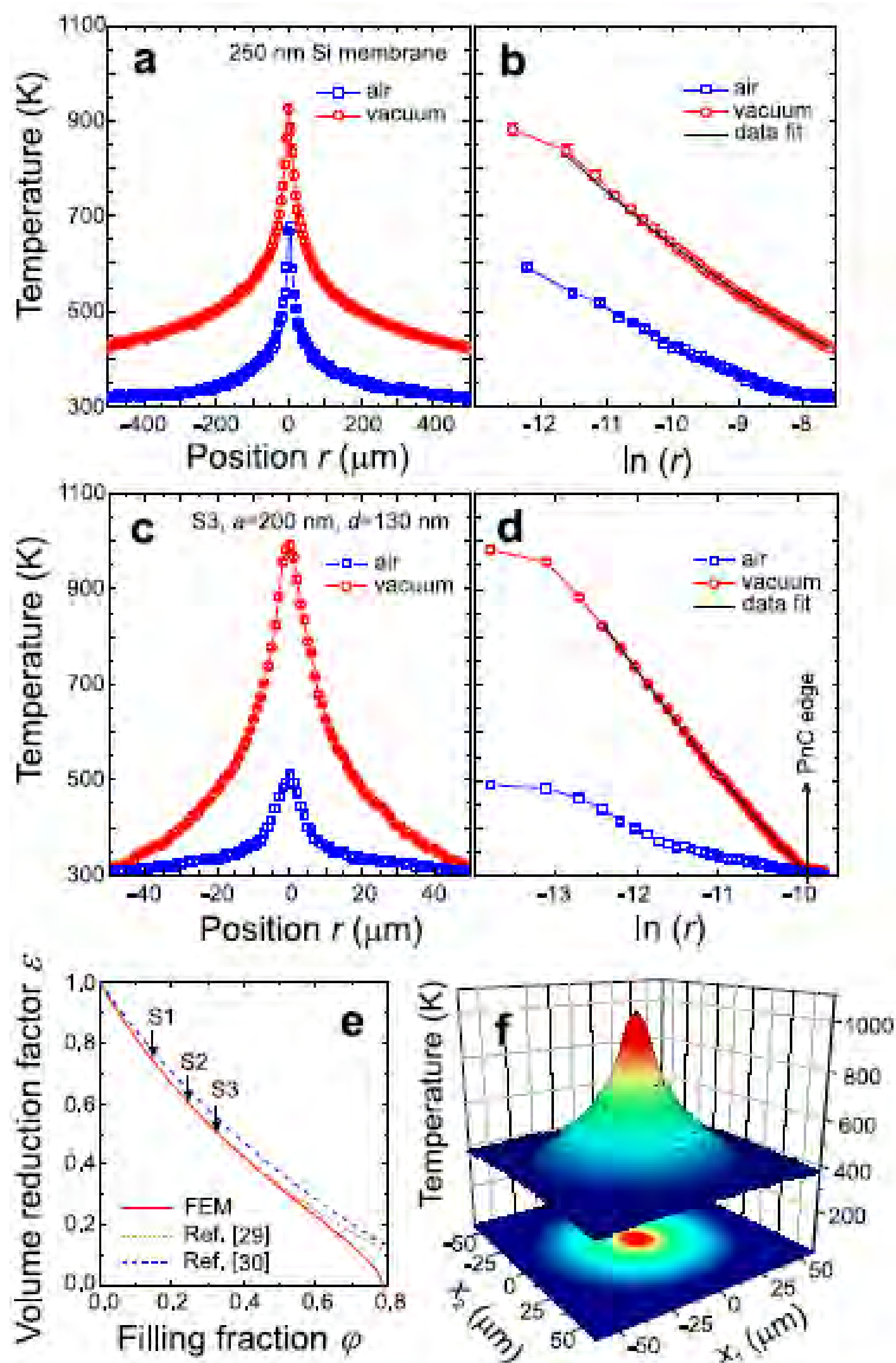

Fig. 18 Linear and corresponding logarithmic temperature profiles of (a, b) pristine 250 nm thick Si membrane and (c, d) sample S3 with lattice parameter of $a = 200nm$ and hole diameter of $d = 130\,nm$ (e) Volume reduction factor ε as a function of porosity calculated by FEM and using analytical expressions. (f) Measured temperature map of the sample S1 with lattice parameter $a = 300\,nm$ and hole diameter $d = 135\,nm$.

Figure 19a shows a comprehensive plot of $k(T)$ obtained for three porous samples and the 250 nm thick bare membrane. These results show that the reduction of the thermal conductivity in the porous samples with respect to the pristine membrane depends on the sample feature size and temperature. The observed reduction in the thermal conductivity is attributed to the phonon mean free path suppression due to the phonon diffusive boundary scattering in addition to phonon-phonon scattering processes. However, the contribution of coherent effects is still a subject of debate and will be discussed in a separate subsection.

As we can see from Fig. 19a, at first glance $k(T)$ decreases together with the sample neck size, namely, the shortest distance separating holes, given by $n = a - d$. Figure 19b depicts explicitly this behaviour in a log-log plot of the normalized thermal conductivity $k_{norm} = k/\,k_{mem}$ at three exemplary temperatures as a function of the neck size. From these data we can conclude that over a broad range of temperatures the dependence of k_{norm} on the neck size can be approximated by a function $k_{norm} \propto n^2$. interestingly, the same correlation function has been found recently for similar structures, with smaller feature size.[68] This trend holds for three exemplary temperatures and for a particular neck size the rate of decrease of k becomes smaller with increasing temperature. Since in our case the thermal conductivity depends on temperature as $k(T) \propto T^{-\beta}$, we can conclude that this behaviour is governed by the exponent β. The latter parameter is plotted as a function of neck size in Fig. 19c, where the exponential data fit is constrained to originate in $(n = 1, \beta = 0)$ and approach β of a pristine membrane as n tends to infinite. As can be seen, the temperature dependence of k becomes weaker with decreasing the distance between holes. This points to the diminishing role of phonon-phonon processes, which are overwhelmed by the temperature-independent diffuse phonon-boundary scattering. From Fig. 19b,c we deduce that both, the reduction and temperature dependence of the thermal conductivity, are related to the geometrical features of the samples. In other words, the thermal properties can be designed and tuned in a simple and efficient manner by changing the neck size. All the results discussed above are gathered in Table II. We point out that the thermal conductivity of the porous membranes can be reduced at most by a factor

of about 40 with respect to bulk Si at $300\,K$, thus approaching the amorphous limit of Si $k_{a-Si} = 1.7\,Wm^{-1}K^{-1}$.

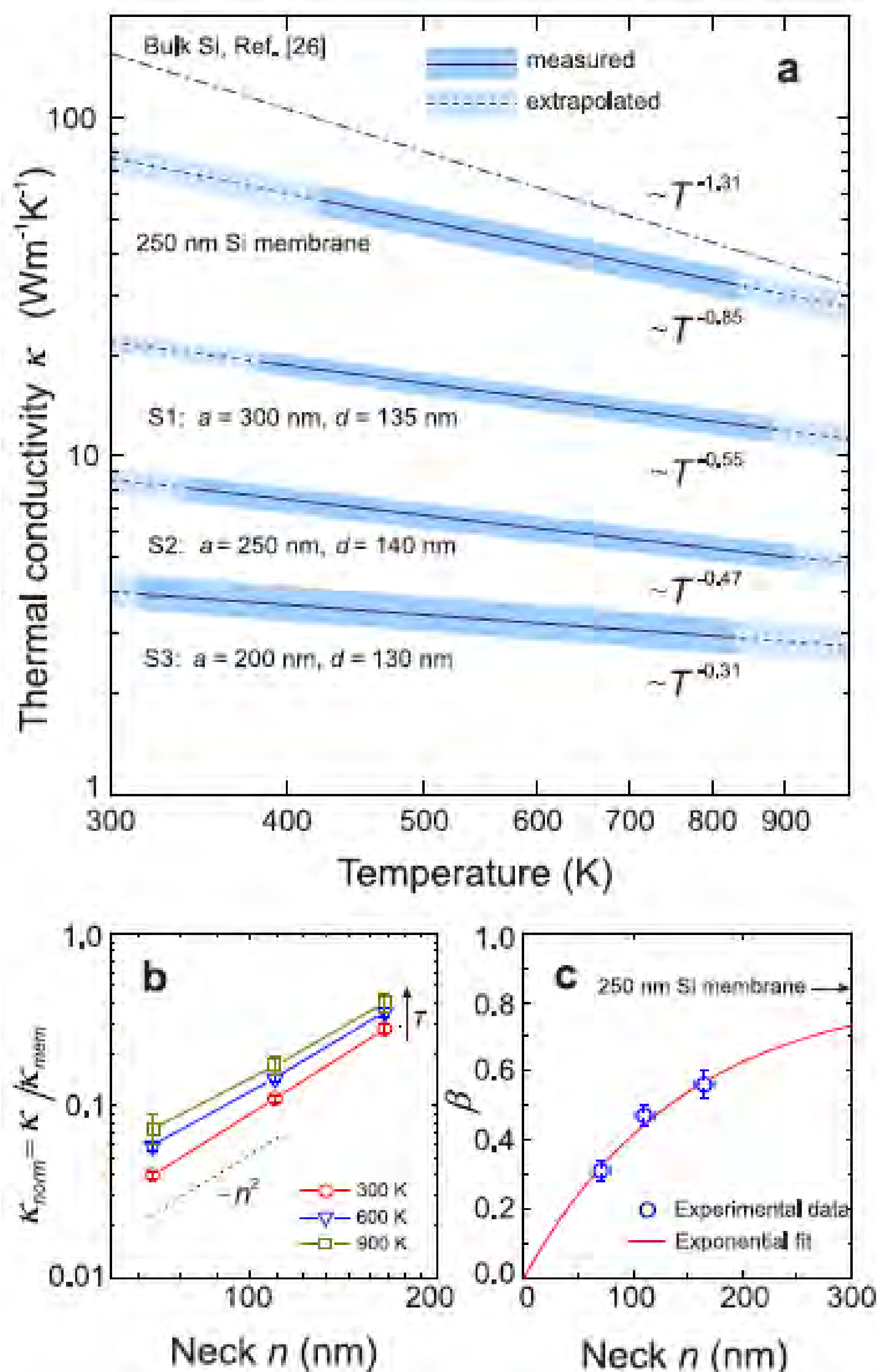

Fig. 19 Temperature dependence of the thermal conductivity. (a) Thermal conductivity of periodic porous membranes and $250\,nm$ thick membrane as a function of temperature. (b) Normalized thermal conductivity of porous membranes as a function of the neck size n for three example temperatures. (c) The exponent governing the temperature dependence of k as a function of the neck size n.

Coherent versus incoherent effects

It is clear that phonons with Λ shorter than the lattice parameter can be treated purely as particles governed by the bulk dispersion relation. Otherwise, the wave-like nature can be manifested as, e.g., dispersion relation zone folding, flattening of branches and band gaps, all of which have implications on the phonon group velocity and density of states (DOS) and, consequently, on the thermal conductivity. In such a case periodic porous membranes are synonymous to 2D PnCs. In bulk silicon, mean free paths span a broad range with Λ longer than 1 μm contributing to ~ 50% of the total thermal conductivity.[58,77,78] Furthermore, as predicted theoretically, in the case of 250 nm thick Si films, phonon mean free paths exceeding 300 nm contribute to about 20% of the total thermal conductivity.[72]
Since we investigate structures with lattice parameters smaller than 300 nm, it might be reasonable to consider the suppression of the thermal conductivity due to coherent Bragg scattering. The effects of coherence have been demonstrated in similar structures by BLS.[61,64,65,79] These results showed modification of the phonon dispersion in the GHz regime, exhibiting typical features of PnCs band diagram, such as zone folding, modification of group velocity and band gap opening.[61] However, at high temperatures most of the heat in bulk Si is carried by phonons of frequencies around 5 THz.[69,75] In this high frequency range the change in the phonon dispersion relation in periodic porous membranes (or PnCs), if any, can be captured indirectly by two-phonon (second order) Raman scattering.[80-82] The second-order Raman spectrum, which in bulk Si is dominated by overtones and, thus, has a striking similarity with the two-phonon DOS, is sensitive to the phonon dispersion relation along the Brillouin zone. Although it cannot be used to determine the dispersion relation, any change (additional dips or peaks) may be a clear indication of the modified phonon dispersion. In Fig. 20 we compare second-order Raman spectra of the pristine membrane and S1 measured in the $x_3(x_1x_1)\bar{x}_3$ scattering geometry. As we can notice the measured range of $100 - 1100\ cm^{-1}$ that corresponds to $1.5 - 16.5\ THz$ shows no detectable singularities in the Raman spectra of the S1 compared to the pristine

membrane. Furthermore, all spectral features are typical of bulk Si. Thus, it is unlikely that coherent effects play a role in the observed reduction of k.

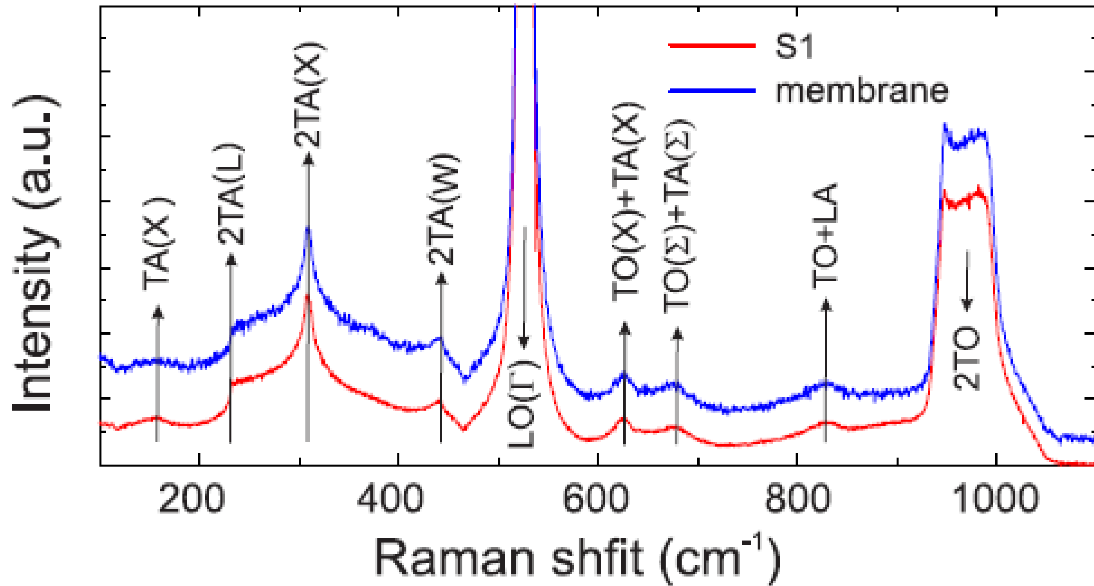

Fig. 20 One and two-phonon Raman spectra mimicking phonon DOS. Data obtained for pristine 250 nm membrane and S1 at room temperature. The arrows indicate critical points of the first Brillouin zone of bulk Si, where TA and TO are transverse acoustic and optical modes, respectively, and LO are longitudinal optical modes.

To further study the existence of coherent effects in the THz regime, the thermal conductivities of ordered (S4) and disoredered (S5) porous membranes were measured. Figure 21a displays the temperature profiles for the samples S4, S5 and the unpatterned Si membrane as measured by 2LRT. The purely linear decay observed when we plot the temperature profiles in logarithmic scale (see Fig. 21b) indicates that the thermal conductivity can be treated as temperature independent because the temperature range is sufficiently small ($\sim 50\ K$). In this case, the thermal conductivity, k_0, can be related directly to the slope of the thermal decay as discussed in Section 2.2. We recall that for the case of bulk Si the thermal conductivity changes by about 15% in the range from 350 to 400 K.[69] This variation represents only an upper (bulk) limit because the temperature dependence is typically reduced as boundary scattering increases. On the basis of these measurements and using a correction factor $\varepsilon = 0.528$, which was estimated according to a filling fraction of $\varphi = 0.267$, we obtain the same value for the thermal conductivity $k = k_0/\varepsilon = 14\ \pm 2\ Wm^{-1}K^{-1}$ for

the ordered (S4) and disordered (S5) porous membranes compared to $k_0 = 80 \pm 3\, Wm^{-1}K^{-1}$ of the unpatterned membrane. The reduction in the thermal conductivity of the ordered and disordered porous membranes is the same, down to 18% of the value of the unpatterned membrane, which corresponds to a 6-fold reduction. This value is in close accordance with the values found in the previous samples taking into account that the temperature measurements in S4 and S5 were performed in ambient air and a factor accounting for heat losses to air was applied. Therefore the introduction of short-range disorder does not affect the room-temperature thermal conductivity, thus there is no evidence of coherent effects related to the periodic porous arrays in the THz regime. On the contrary, the introduction of disorder in the arrays of holes has been demonstrated to impact the coherence of phonons in the GHz range.[83] Samples S4 and S5 were designed to fulfil the requirement of presenting identical surface to volume ratio. Therefore, since this parameter is maintained in both samples, but increased with respect to the unpatterned membrane, it is likely that the reduction measured in both S4 and S5 is purely related to diffusive scattering at the surface roughness. In this case, it appears that coherence will not be preserved when the dominant phonon wavelength is commensurate with the hole boundary roughness.

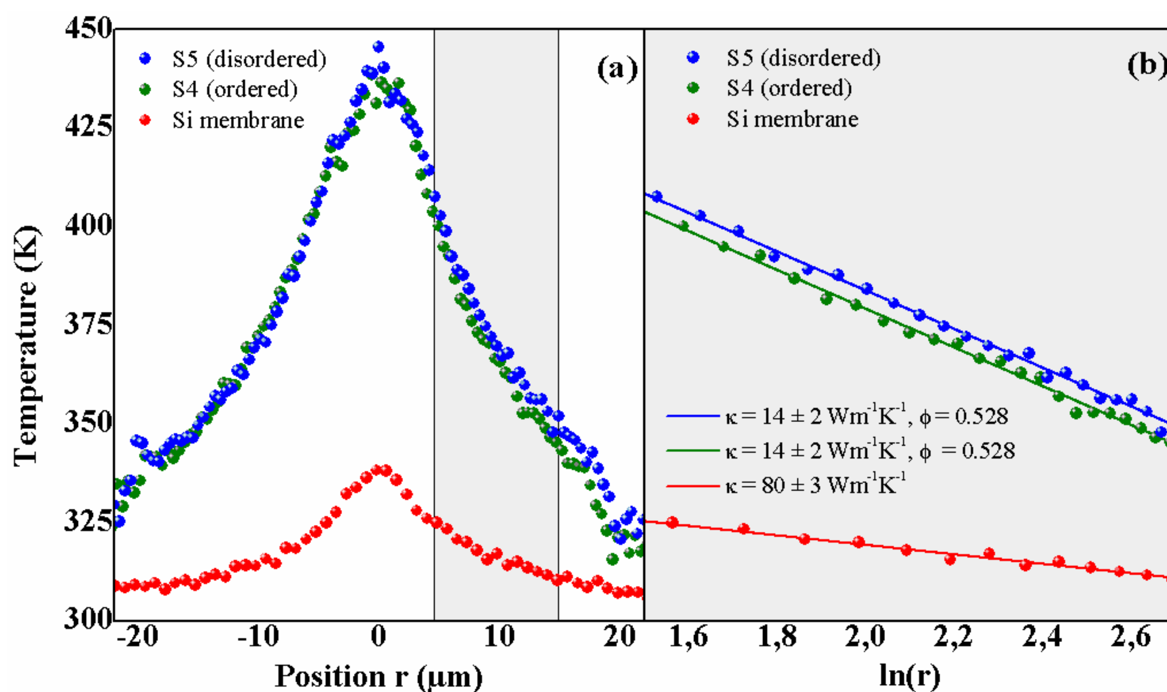

Fig. 21 (a) Temperature line-scan profiles of the ordered and disordered PnCs and the unpatterned Si membrane. (b) Logarithmic plot of the highlighted area in (a) to visualize the $ln(r)$ relation as predicted by eq. (16).

sample	a (nm)	d (nm)	φ	ε	k $(300\ K)$	k $(600\ K)$	k $(900\ K)$	β	$\frac{k_{mem}}{k_{bulk}}$ $(300\ K)$	n (nm)
S0	-	0	0	1	77.9 $\pm$ 8.1	42.5 $\pm$ 4.3	30.1 $\pm$ 3.2	0.85	~2	-
S1	300	135	0.159	0.725	21.9 $\pm$ 1.9	14.6 $\pm$ 1.1	11.9 $\pm$ 0.9	0.55	~7	165
S2	250	140	0.246	0.604	8.5 $\pm$ 0.9	6.2 $\pm$ 0.6	5.1 $\pm$ 0.5	0.47	~18	110
S3	200	130	0.332	0.499	3.9 $\pm$ 0.4	3.2 $\pm$ 0.3	2.8 $\pm$ 0.3	0.31	~40	70
S4	300	175	0.267	0.528	14 $\pm$ 2	-	-	-	~6	125
S5	-	175	0.267	0.528	14 $\pm$ 2	-	-	-	~6	-

TABLE II Characteristic sizes, coefficients and exemplary experimental data for the porous membranes and the 250 nm Si membrane: a - lattice spacing, d - hole diameter, φ - filing fraction, ε - volume reduction factor, n – neck size, k - thermal conductivity ($Wm^{-1}K^{-1}$).

Air-mediated cooling

Up to this point we have considered only measurements performed in vacuum, i.e., where air-mediated thermal transport via convection and conduction is negligible. This becomes rather important for the PnCs as operational building blocks in real-life applications, besides those for outer space. In principle, air has a poor thermal conductivity of about $2.623 - 6.763\ x\ 10^{-2}\ Wm^{-1}K^{-1}$ between 300 and 900 K.[84] However, in structures with high surface-to-volume ratio and reduced thermal conductivity heat dissipation via air has to be taken into account. This effect was previously observed in graphene,[85] photonic crystals[86] and nano-beams.[87] To analyse this issue in porous membranes we go back to Figs. 18a-d, where we compare 2LRT results obtained in vacuum and air.
At first glance, the temperature profiles of the pristine membrane and the exemplary porous membrane shown in Fig. 18a and 18c, respectively, clearly indicate heat losses caused by the presence of air. Foremost, the temperature rise at $r = 0$ for both samples in air are significantly smaller than those measured in vacuum. Consequently, if one were to use the conventional single laser Raman thermometry the thermal conductivity measured in air would be overestimated by factors of about 1.4 and 1.9 for

the membrane and S3, respectively. Likewise, $k(T)$ obtained from the corresponding logarithmic temperature profiles recorded in air (see Figs. 18b and 18d) would be inaccurate.

In what follows, we use these data and propose a novel approach to quantify the heat dissipation resulting from natural air-mediated cooling in 2D systems. Let us return to eq. (16) which determines k in vacuum conditions at a temperature T using the measured P_0 and $\xi(r)$. The latter, considered simply as the slope of the logarithmic temperature profile at r, is different for the vacuum and air data, showing larger nonlinearity for data taken in air, as seen in Figs. 18b and 18d. The only reason for this difference comes from the air-mediated losses, denoted P_{loss}, which occur in a distance from 0 to r. The thermal conductivity $k(T)$ and thickness t remain unchanged, thus in the case of the data obtained in air eq. (16) can be rewritten as:

$$k(T') = -\frac{P_0 - P_{loss}}{2\pi t \xi'(r)} \qquad (19)$$

where we denote the temperature and the slope of the logarithmic temperature profile at any arbitrary point r determined in air by T' and $\xi'(r)$, respectively. By combining eq. (16) and eq. (19) we obtain a simple expression that determines the relative air-mediated losses:

$$\frac{P_{loss}}{P_0} = 1 - \frac{\xi'(r)}{\xi(r)} \frac{k(T')}{k(T)} \qquad (20)$$

Figure 22a depicts relative losses as a function of the surface-to-volume ratio calculated for the membrane and the three porous samples. Here, we compare heat dissipation from the lateral area defined by the porous membrane, thus eq. (20) is derived for $r = 50\ \mu m$. The losses are seen to vary from about 8% to 85%, while the general trend is clearly nonlinear. The latter may result from the porosity and specific orientation of the samples, in particular the holes, with respect to the gravity vector, which allows free air flow through the holes. Consequently, the losses grow faster than it would be expected from the increasing surface-to-volume ratio.

To analyse this issue we plot in Fig. 22a the absolute value of losses P_{loss} as a function of surface-to-volume ratio. In this case, the use of relative losses may result in a misleading conclusion, where the optimum surface-to-volume ratio would need to be as large as possible. As shown before the measured samples differ in the thermal conductivity, therefore, to get approximately the same temperature rise at the hot spot we applied a different heating power for each case. From Fig. 22a we find that the porosity of S1 increases the absolute losses by about 60% with respect to the pristine membrane, but this trend is reversed when the surface-to-volume ratio is further increased (samples S2 and S3).

To understand this behaviour we examine the measured k_{exp} and the intrinsic k thermal conductivity, which are plotted at exemplary temperature of 600 K in Fig. 22b. The extensive structure property such as the thermal conductance is governed not only by the intrinsic k but also by the volume removal factor ε, thus the effective thermal conductivity values of the porous membranes are even lower and given by $k \cdot \varepsilon$. Now, if we compare Figs. 22a and 22b we see that increasing surface-to-volume ratio results in two opposite effects: (a) the increase of the relative heat losses due to the presence of air and (b) the reduction of the thermal conductivity. In other words, if efficient heat removal is the main priority then the effect of the reduced k has to be minimized. In practice this boils down to making the porous membrane neck sufficiently larger than the Λ.

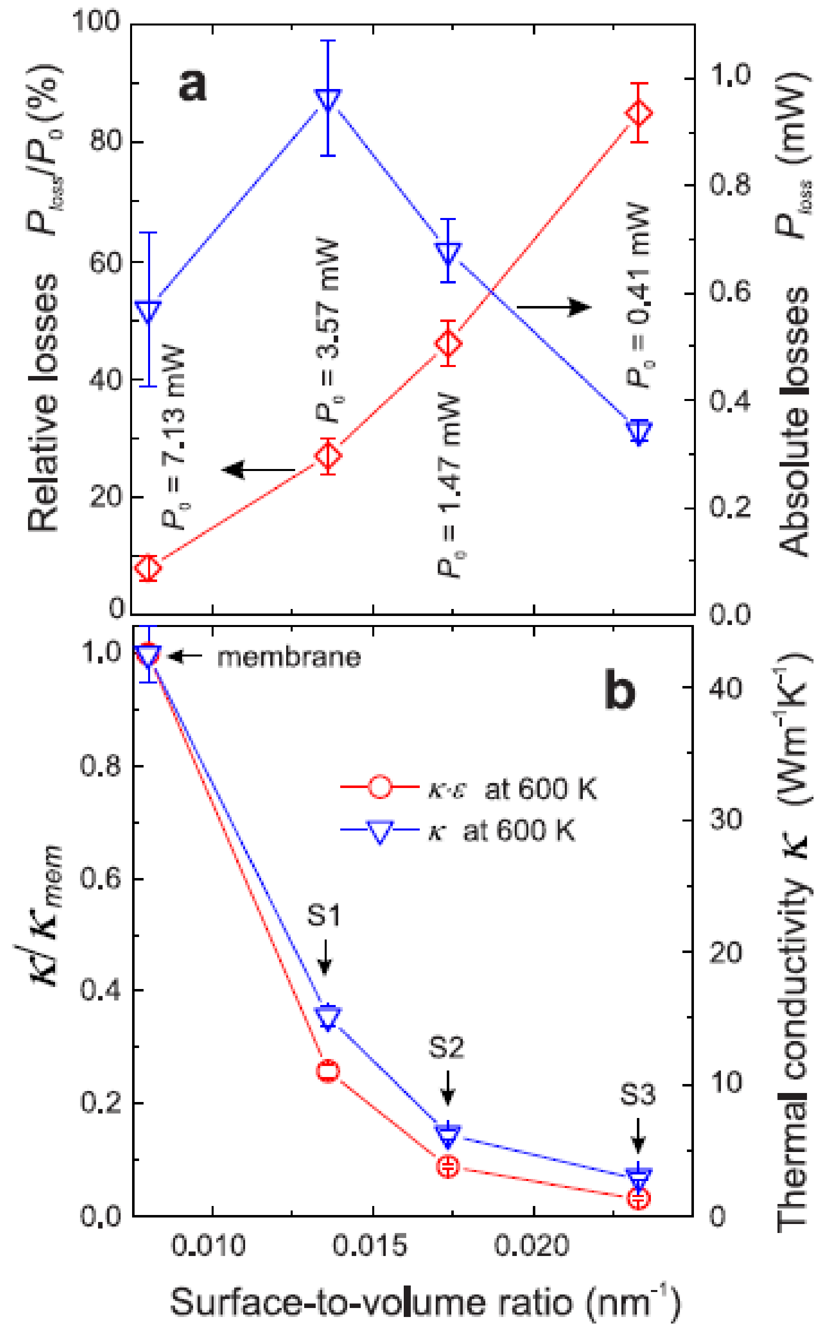

Fig. 22 (a) Relative $P_{loss} = P_0$ and absolute P_0 losses caused by air-mediated cooling. (b) Measured $k_{exp} = k \cdot \varepsilon$ and intrinsic k thermal conductivity at 600 K as a function of surface-to-volume ratio.

In summary, we investigated heat transport carried via lattice conduction in monocrystalline silicon membranes with two different conditions regarding characteristic sizes. In the first case the study has been performed on membranes with varying thickness from 8 to 1000 nm. In the second case, the membrane thickness is fixed 250 nm and a square

array of holes is patterned with the distance between holes or neck size increasing from 70 to 165 nm. We showed that the in-plane thermal conductivity of silicon and its temperature evolution from room temperature to about 900 K can be effectively reduced and tuned by means of the sample geometrical feature, i.e., the thickness or the neck size.

We also demonstrated that the thermal conductivity at room temperature can be decreased down to about 4 $Wm^{-1}K^{-1}$ in the periodic porous membranes with thicknesses of 250 nm. This value reaches the amorphous limit of silicon and is half the value achieved in a pristine silicon membrane of only 8 nm. Measurements of the thermal conductivity in periodic and disordered porous membranes showed that the reduction of the thermal conductivity reaches the same values for both samples. Therefore we attribute the observed reduction to the shortening of the phonon mean free path due to diffuse (incoherent) phonon-boundary scattering.

Finally, we demonstrated that heat dissipation in porous membranes resulting from the presence of air can be significant and tunable depending on the sample surface-to-volume ratio.

4

$Si_{1-x}Ge_x$ epitaxial nanowires

One-dimensional $Si_{1-x}Ge_x$ semiconductor nanostructures have attracted enormous research interest due to their unique electronic properties and recently have been utilized in a wide range of applications, such as heterojunction bipolar transistors, strained Si complementary metal-oxide-semiconductor (CMOS) devices,[88,89] nanoelectronics[89-92]and IR sensors.[93] Nanowire transistors with gate lengths of 5 nm have been produced in gate-all around configuration by scaling down the corresponding intrinsic nanowires (NWs) channel body.[94,95] In particular, in-plane assembled nanostructures target suitable geometry for integration on Si chips and CMOS architecture using planar microfabrication technology.[96] The continuous downscaling of semiconductor devices results in the fabrication of devices with sub-micrometre feature sizes, where localized Joule heating becomes important. Therefore high-resolution measurement techniques are necessary for the thermal characterization.

Thermal transport in $Si_{1-x}Ge_x$ NWs has been studied over the last decade both theoretically[97-104] and experimentally.[100-105,106,107] Most experimental studies focused on measuring the thermal conductivity of individual $Si_{1-x}Ge_x$ NWs with various Ge concentrations and diameters using microfabricated suspended thermometer/heater platforms. Furthermore, recent studies even proved the existence of ballistic thermal conduction in $Si_{1-x}Ge_x$ NWs with low thermal conductivity for a wide range of structural variations and alloy concentrations.[107] These results showed the significant potential of $Si_{1-x}Ge_x$ NWs in thermoelectric applications. However, only few experimental studies have reported thermal transport on supported $Si_{1-x}Ge_x$ NWs or NWs embedded in a matrix material,[108,109] which are more representative structures for many future NW-based applications.

In addition, the composition analysis of this kind of nanostructures is necessary. Usually performed by micro-Raman spectroscopy[110-113] and EDX analysis.[114,115] Although Raman spectroscopy is a fast and non-destructive technique to characterise nanostructures, there are some limitations, such as the lateral spatial resolution of about 300 nm, which does not allow discriminating composition inhomogeneities within, e.g., sub-300 nm nanostructures.

In this chapter is presented all the work performed related with the structural, compositional and thermal characterization of self-assembled $Si_{1-x}Ge_x$ nanowires (NWs). Briefly, the in-plane epitaxial Si_{1-x}Gex alloy NWs were grown by molecular beam epitaxy (MBE) on a Si (001) substrate using Au nanoparticles as catalyst. The growth consists of a three-step process involving the deposition of 1 nm thick each Au and Si layers, the AuSi seeds formation by annealing these layers at 800 ^0C and finally, the growth of the $Si_{1-x}Ge_x$ alloys by continuously supplying a Ge flux at 550 ^0C. More details about the fabrication process can be found elsewhere.[116] The growth of the sample has been made in the Institute of Science and Materials in Barcelona (ICMAB-CSI).

4.1 Structural characterization

Morphology

The surface morphology of the $Si_{1-x}Ge_x$ alloy NWs was characterised by means of SEM, AFM and TEM. Figure 23a shows the SEM image of the AuSi clusters after annealing the 1 nm Au and Si films at 800 ^0C. A SEM image of as grown $Si_{1-x}Ge_x$ alloy NWs is presented in Fig. 23b, where the variation of widths, heights and lengths is evident as well as the directional growth along the <110> directions of the Si substrate. Due to the excess Au content of the liquid SiGeAu droplets, Au rich particles at the end of the NWs are apparent after the MBE growth. These nanoparticles usually match the transversal size of the NWs, indicating that growth takes place following a vapour-liquid-solid (VLS) mechanism by continuous supply of a Ge flux at a fixed temperature of 550 ^0C. Previous investigations showed that at this temperature the diffusion length of Si atoms on the surface is quite small

whereas for Ge atoms it is of the order of $1\,\mu m$. Initially, Ge atoms as supplied from the effusion cell are homogeneously distributed on the whole substrate surface. All atoms remain adsorbed (the sticking coefficient at 550 ^0C is 1) and diffuse before they incorporate to the growing nanostructures. Most Ge atoms are preferentially collected by the liquid droplets and contribute to the NWs growth. The width and length distribution of these NWs was measured to be $w = 50 - 606\,nm$ and $L = 0.3 - 4\,\mu m$, respectively.

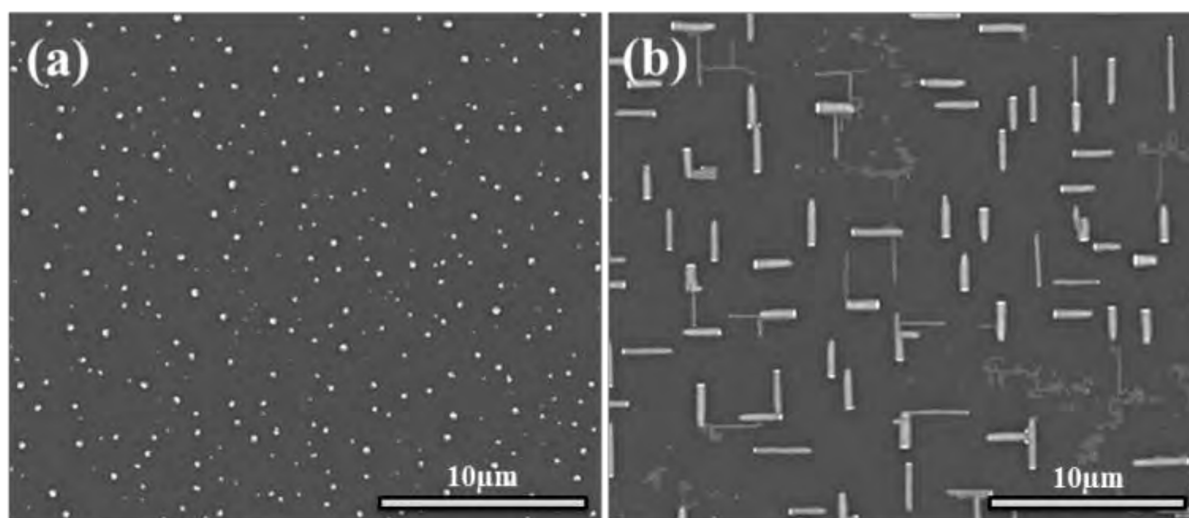

Fig. 23 SEM images of (a) the AuSi seeds after 5 minutes annealing of the Au and Si layers at 800^0C and (b) the in plane epitaxial $Si_{1-x}Ge_x$ alloy NWs after the Ge deposition by MBE.

However, a fraction of atoms do not reach a droplet and must contribute to form a thin wetting layer (WL) on most of the substrate. The existence of this WL could not be previously demonstrated and is observed in the present work. The NWs where also found to be compositionally homogeneous in length but display an inhomogeneity in the vertical cross section. Even if the SiGe composition given by the VLS process should be well-determined, the behaviour of the diffusing Ge atoms obviously can modify both the average composition as well as the vertical composition profile as is evaluated in this work. Although the growth mode in these samples is not a purely epitaxial process of SiGe on Si, the resulting NWs are epitaxial, as is shown below.

In Fig. 24a top view of one of the selected regions of the sample surface with NWs of different dimensions is shown. The region marked by the FIB

instrument created thick lines around the selected NWs. After the scanning thermal microscopy measurements, this area was prepared for TEM imaging and composition analysis. Figure 24b illustrates the same selected region in a cross sectional plane showing three of the four studied NWs. Figure 25a,b show lattice resolved ultra-high resolution TEM images of a single $Si_{1-x}Ge_x$ NW confirming its epitaxial growth along the <110> directions of the Si substrate.

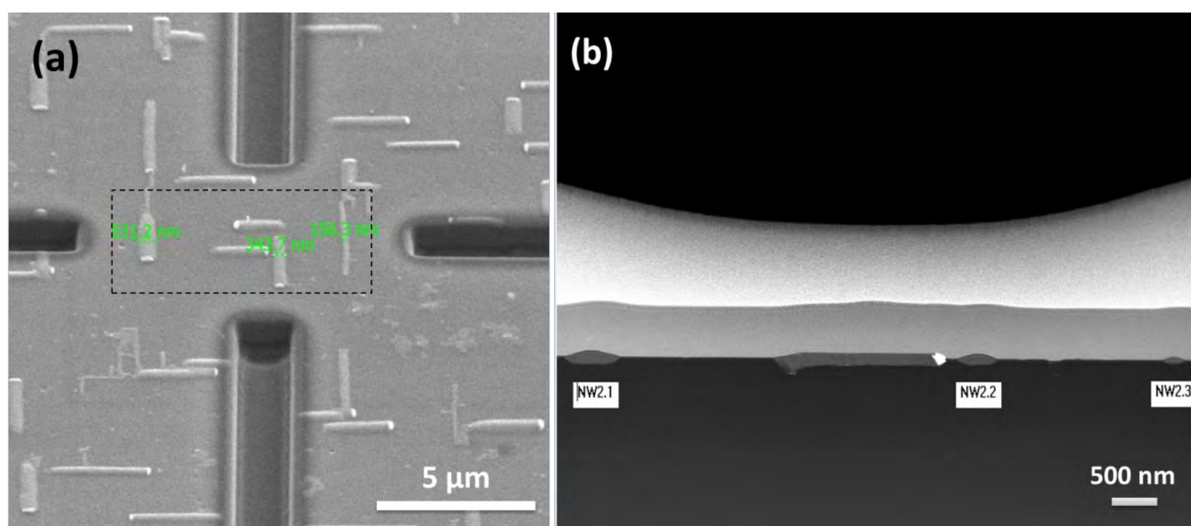

Fig. 24 (a) SEM image of one of the selected region of the sample surface, (b) cross section TEM images of three selected $Si_{1-x}Ge_x$ alloy NWs,

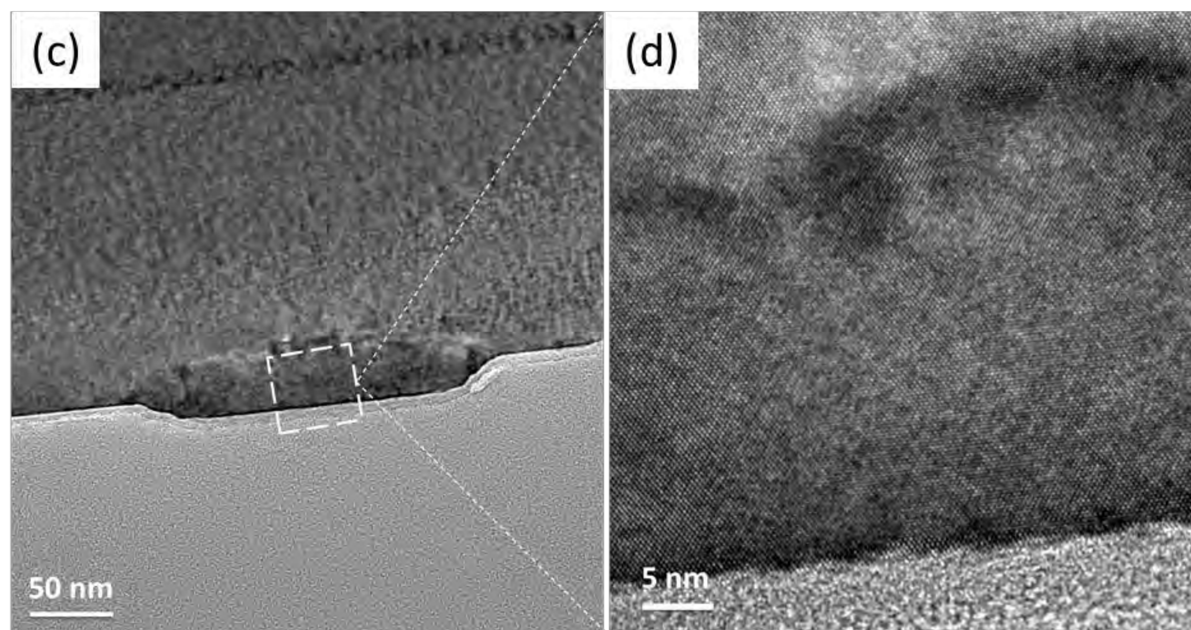

Fig. 25 (a), (b) High resolution TEM images of a single $Si_{1-x}Ge_x$ alloy NW.

In Fig. 26a is shown an atomic force microscopy image of the sample surface with different $Si_{1-x}Ge_x$ alloy NWs. The root mean square roughness is equal to 2.3 nm in the case of the NWs and 2.9 nm in the case of the WL. Figures 26b,c illustrate transverse and longitudinal topography profiles, respectively, of a single $Si_{1-x}Ge_x$ alloy nanowire. In some cases, Au rich particles were observed slightly higher (~ 7 nm) than the rest body of the NWs due to additional material deposition during cooling after growth. In order to measure more accurately the topography of the sample surface, a sharp atomic force microscopy tip was used.

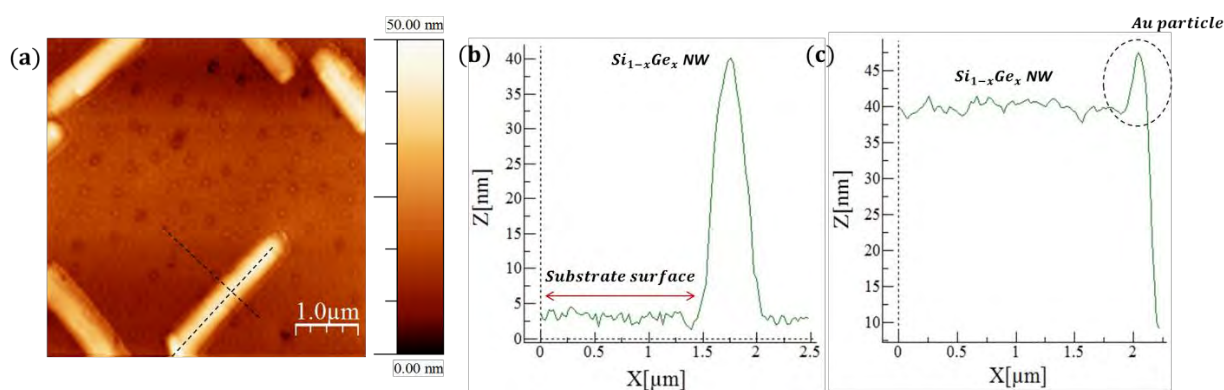

Fig. 26 Atomic force microscopy image of the sample surface (a) topography profile across (b) and along (c) a single $Si_{1-x}Ge_x$ alloy nanowire taken from the line scans depicted in (a).

Ultra-High resolution images in scanning-transmission mode (HRSTEM) of the selected $Si_{1-x}Ge_x$ alloy NWs are presented in Fig. 27. From the TEM analysis, we found that the NWs have elongated shape, with the height (h) roughly decreasing proportionally to the width (w) according to a relation $h(w) = a \cdot w$, where $a = (17 \pm 2.5)\%$. This approximate geometrical relationship is related to the fact that the NWs are actually faceted with a {001} top facet and lateral sidewalls mostly consistent with {115} planes. The inclination of these planes is $\Theta = 15.8$ degrees. Most of the width is given by the lateral sidewall geometry, that is, the proportionality constant is larger but close to $(tan\ \Theta)/2 = 0.14$.

In addition, we found that the NWs are partially buried with approximately half of the thickness embedded in the substrate. In fact, the NWs start to nucleate from droplets starting at dissolution pits. It was found that the droplets dissolve the substrate generating truncated inverted pyramids, with their lateral sides always oriented along <110> directions of the substrate and sidewalls consistent with {115} planes, resulting in the

approximate mirror-like appearance of the cross section and the preferential elongation direction of the NWs.

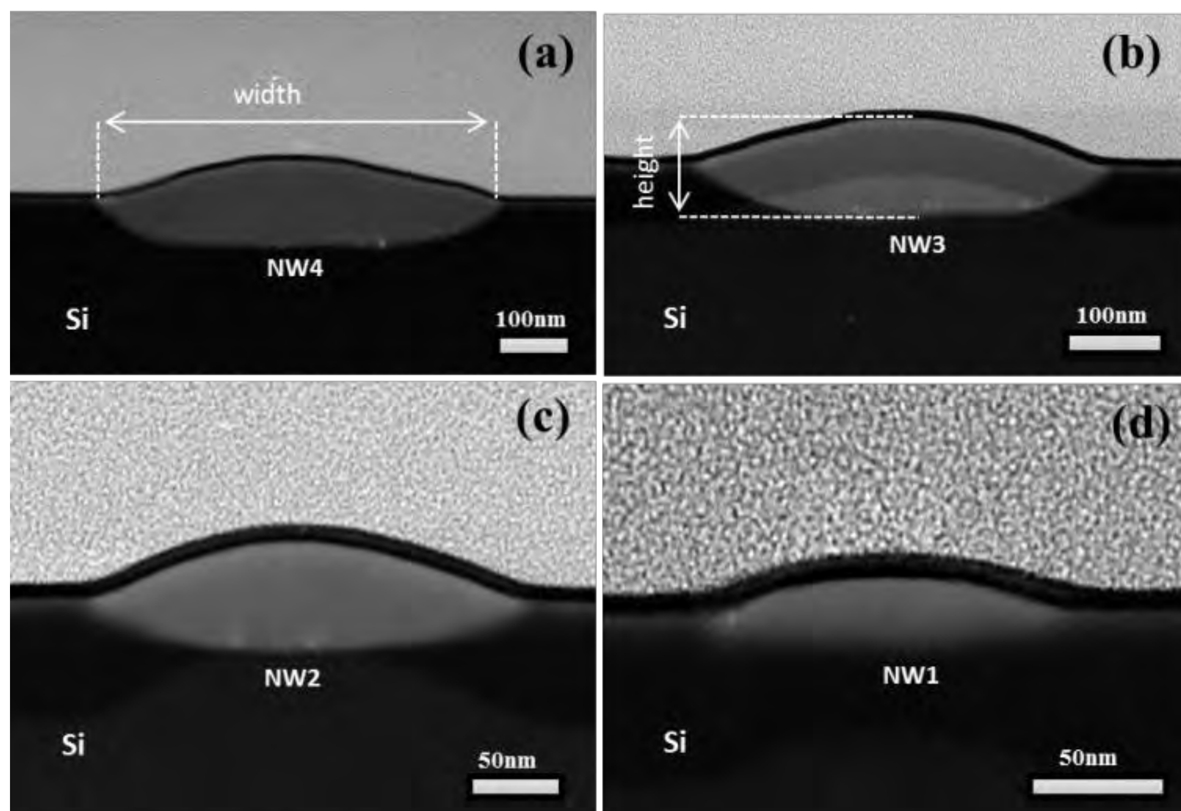

Fig. 27 (a)-(d) Cross section TEM images of the four investigated $Si_{1-x}Ge_x$ alloy NWs. Note that the scale bar is different in each image.

Table III summarizes the morphological characteristics of the four selected NWs. The perimeter/area ratio (P/A) accounts for the surface to volume ratio of the NWs. For the same NWs, we present in the next section SThM measurements which were performed before the composition analysis.

$Si_{1-x}Ge_x$	Width (nm)	Height (nm)	Length (μm)	P/A (μm^{-1})
NW1	130	20	1.32	0.14
NW2	224	47	1.35	0.057
NW3	421	82	2.03	0.032
NW4	585	105	1.21	0.023

Table III. Morphological characteristics of the four investigated $Si_{1-x}Ge_x$ alloy NWs.

4.2 Composition study

Having discussed the morphology of the NWs, we move to the chemical composition analysis of the sample. EDX spectra and elemental chemical maps revealed the existence of Si, Ge and Au both on the sample surface and inside the nanowire arrays in different concentrations. Figure 27a shows a cross-section TEM image in a flat region free of NWs of the sample surface, where the 5 nm WL is apparent. The rectangular box marks the selected area of the composition analysis. Figures 28b,c illustrate the composition map of the WL and the corresponding 2D composition profile, respectively, showing the evidence of an alloyed WL with continuous distribution of Si and Ge and trace amounts of Au. Different areas of the WL were analysed in order to confirm its homogeneity in the whole substrate surface. Figure 28d illustrates the composition map by averaging in the lateral direction from the surface into the substrate. Particularly, within the WL we found a vertical alloy composition gradient with a maximal Ge composition of 14.5 at% at the surface uppermost. The relative low Ge concentration on the WL indicates that Ge diffusion on the substrate towards the NW positions is very effective.

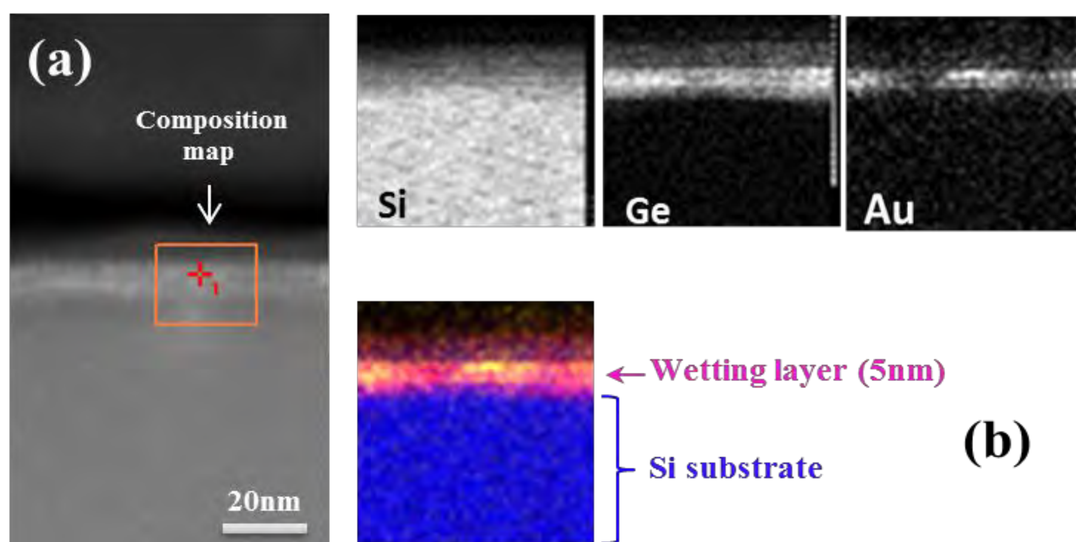

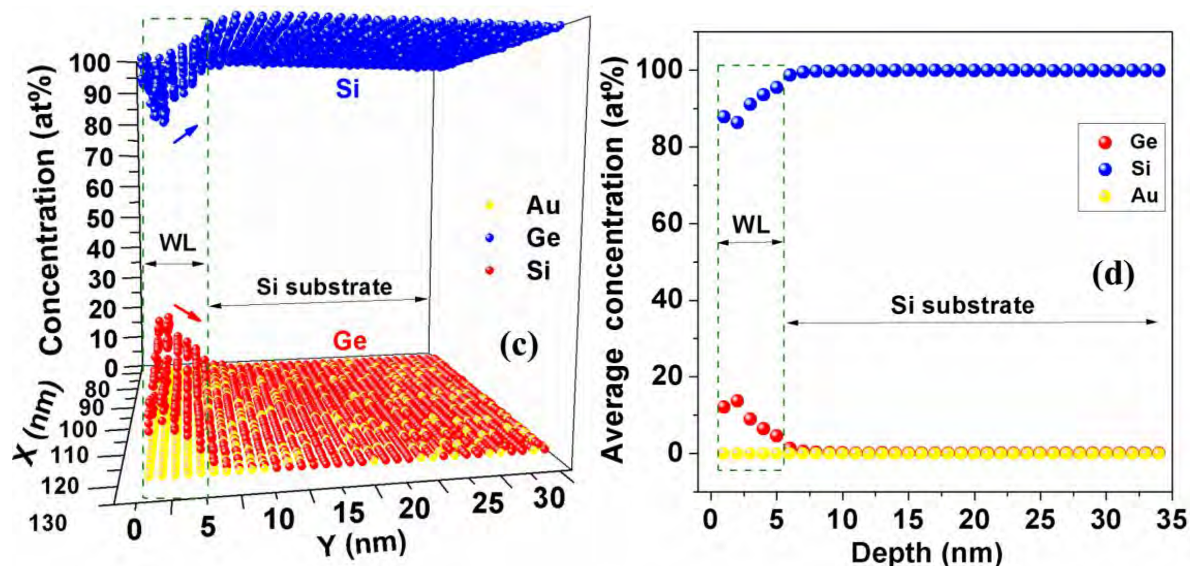

Fig. 28 (a) TEM image of the sample surface where a 5 nm WL is formed, (b), (c) the corresponding composition map and composition profile, respectively, and (d) the average Si, Ge and Au concentration in depth. The spatial resolution of the EDX system is 1 nm.

By further examining composition maps and composition line scans in the selected NWs, we found different vertical composition gradients depending on their cross-sectional size. As this decreases, the composition gradient becomes larger. Figure 29a illustrates the average atomic Si and Ge concentration of each NW as a function of its height. The composition profiles were obtained from composition maps throughout the NWs in the central region around the maximum height. The selected nanowire regions and the corresponding composition maps are shown in Fig. 29c (dark colour means absence of material). The average atomic Ge composition increases (from 50 to 82 %) as the width of the NWs decreases (from 585 to 130 nm). The existence of these composition gradients was expected due to the diffusive nature of the growth mechanism, as has been discussed in previous reports,[110] but the precise values of composition in the NWs core region was difficult to estimate by micro-Raman imaging.

With the previous micro-Raman investigations it was not possible to discern the lateral sizes but it was clear that, in average, thinner NWs were richer in Ge, as is clearly shown here. The obtained large differences in the chemical composition most likely corroborate that diffusing Ge atoms on the substrate tend to incorporate preferentially in regions closer to the top of the NWs, the relative Ge concentration increases being larger in thin

NWs. While the agreement with previous micro-Raman investigations is only qualitative, the results presented here also show that in the NWs the topmost regions tend to be Ge-richer than the core and lower regions.

In addition, we found embedded clusters of Au within all the NWs volume, which indicates that the Au catalyst material was incorporated into the NWs during the growth process. The average atomic Au concentration decreases (from 8.5 to 0.5 %) as the width of the NWs decreases. Figure 29b shows the depth dependent average Au concentration for the four selected NWs. From the composition maps, which are shown in Fig. 29c, we found that the Au is mostly concentrated on the top part of the volume of the NWs. The incorporation of the material catalyst within the NWs volume might affect their electrical properties by creating deep traps in the band gap and changing the carrier mobility as has been discussed elsewhere,[117] therefore a precise determination of Au in the NWs is crucial.

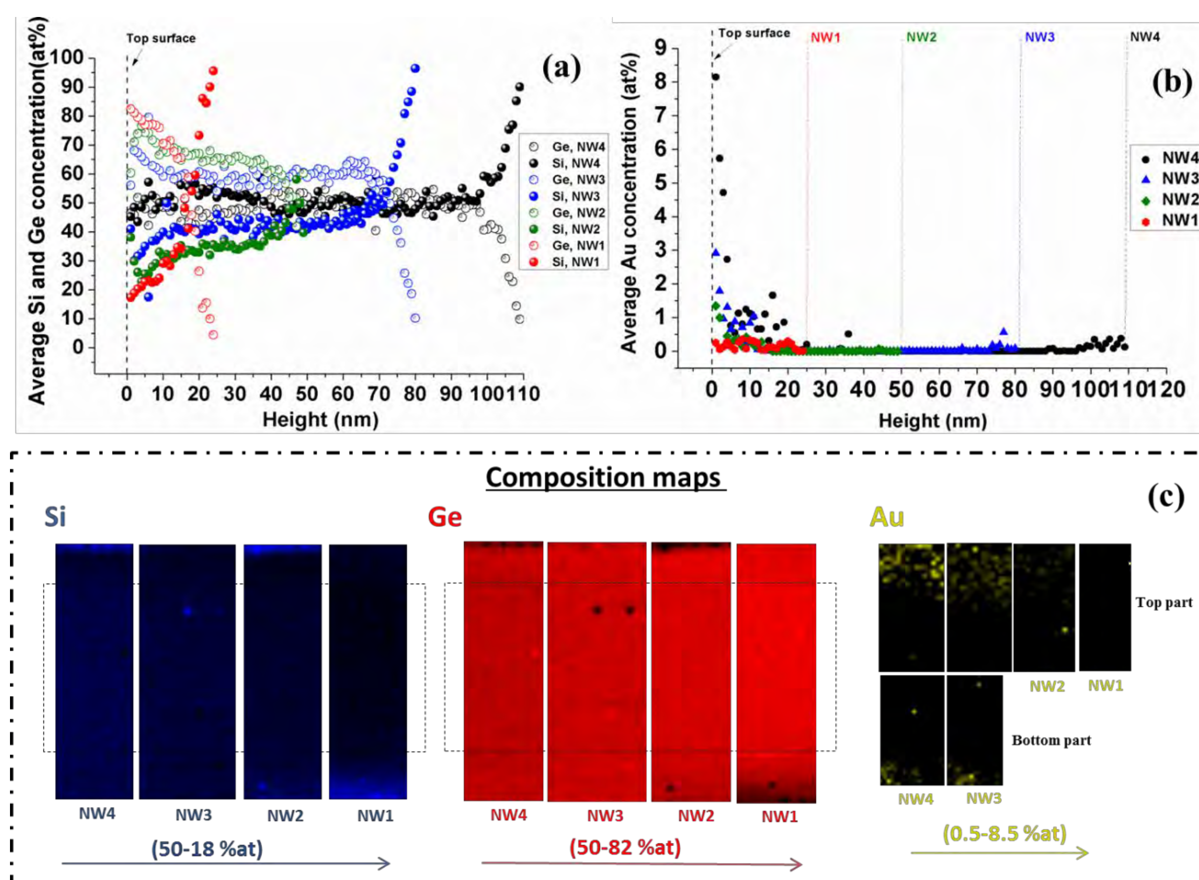

Fig. 29 Average (a) Si, Ge and (b) Au concentration as a function of the height of the four supported $Si_{1-x}Ge_x$ alloy NWs, and (c) the corresponding composition maps. The spatial resolution of the EDX system is 1 nm.

4.3 Thermal properties

In this section, we used the heated tip of a scanning thermal microscope cantilever to study thermal transport across $Si_{1-x}Ge_x$ alloy NWs of different morphological characteristics. We sensitively probed variations of tip-sample effective thermal conductance or resistance by monitoring changes in heat flux related signals by the change of the probe electrical resistance. We consider the heated contact area as an isothermal circular heat source of radius $r_c = (50 \pm 2)\ nm$, as determined from SEM, whereas the low heat capacity ($C_p = 133\ kJ\ kg^{-1} K^{-1}$) of the Pt wires makes the probe sensitive to thermal variations. The thermal probe was used in the active SThM mode, where the probe resistive element is heated by the Joule effect. The thermal conductance between the thermal probe and the sample (G_{th}) includes the thermal conductances due to radiation, the liquid meniscus and air, in addition to its dependence on the contact area.[32,41,42,52,118,119]

First, we obtained the 2D topography and thermal images of the NWs with different dimensions by simultaneous mapping of the local variations in height (Fig. 30a) and the tip-sample thermal resistance (Fig. 30b). The images consist of 256 × 256 points. The integration time of about 30 ms at each point was long enough for the heated volume to reach thermal equilibrium. It is worth mentioning that the scanning probe environment was kept under well controlled conditions (ambient temperature and humidity). In the thermal image (Fig. 30b), the darker regions correspond to signals acquired by the tip in contact with only the $Si_{1-x}Ge_x$ NWs, and the brighter regions corresponds to areas where the scanning probe tip is in contact with the WL. In high thermally conductive regions, the increased heat flux from the tip to the sample results in a larger temperature drop of the probe at the heated junction, which is proportional to a lower probe electrical resistance (R_{pr}^{el}). A Wheatstone bridge circuit was used to correlate changes of R_{pr}^{el} with the measured direct output voltage (V_{out}). In our configuration, changes in the probe electrical resistance (ΔR_{pr}^{el}) produce proportional changes of the output voltage ($\Delta V_{out} \propto \Delta R_{pr}^{el}$) (see details in the experimental methods, chapter 2).

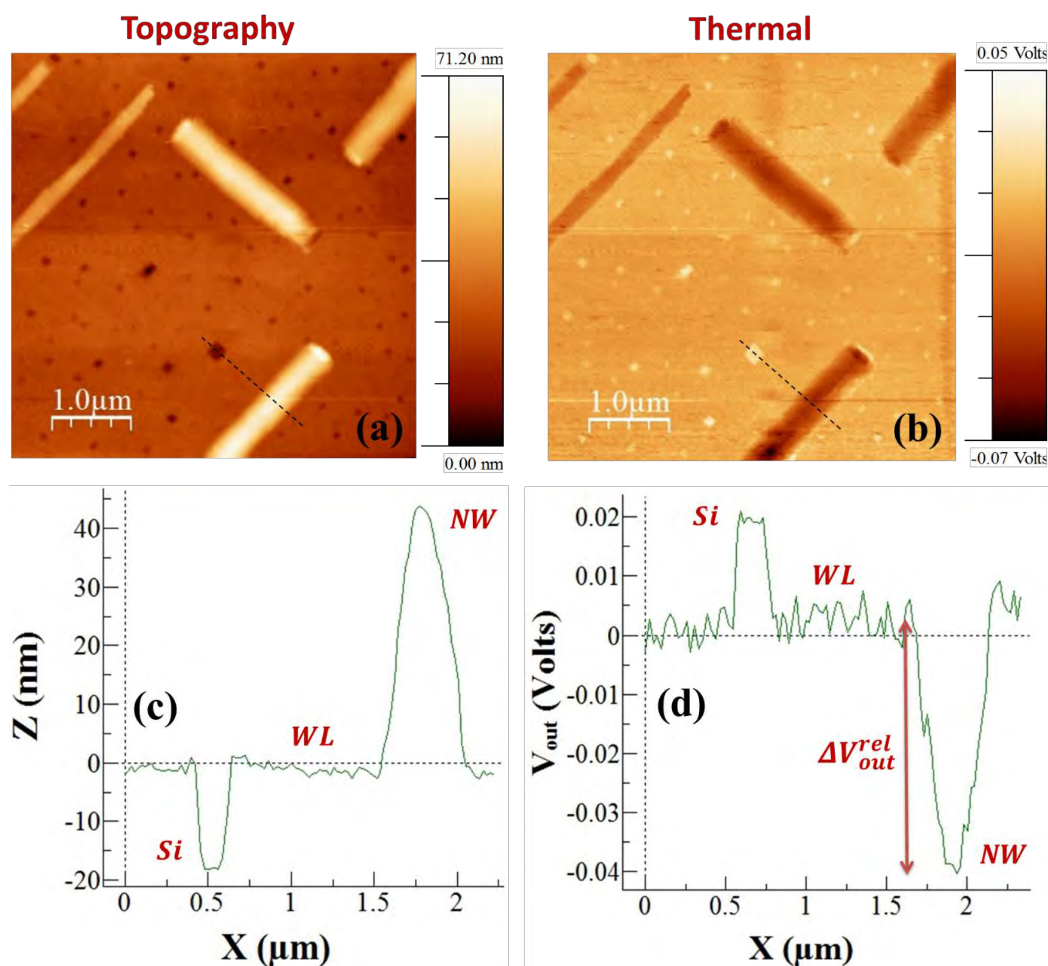

Fig. 30 Examples of (a) topography and (b) thermal image of $Si_{1-x}Ge_x$ alloy NWs with different dimensions, (c) topography and (d) thermal signal profiles along the dashed lines in Fig. 30a and Fig. 30b respectively.

Before the thermal scans, the absolute response of the probe in the WL ($V_{out(WL)} = 3.2\ V$) was measured by bringing the probe in and out of contact with the sample surface. Then, in order to enhance the thermal image contrast when scanning the sample surface and accurately monitor any variation of the signal, for example from the different NWs, we balanced the thermal probe in the WL ($V_{out(WL)}^{rel} \approx 0\ V$) and measured the absolute values of the relative changes of the SThM signal ($\left|\Delta V_{out}^{rel}\right|$) compared to the reference value of the WL.

The relative variation of the thermal signal between the WL and a single NW can be directly observed in the thermal profile of Fig. 30d, which is obtained from the line scan of the thermal image (dashed line in Fig. 30b).

The 40 mV drop of the output voltage on top of the NW compared to the WL region indicates a drop of the heat conduction from the probe to the sample, i.e., an increase of the probe-sample thermal resistance. Note that the probe-sample thermal resistance is composed of interfacial (Kapitza) thermal resistance and the spreading thermal resistance in the NW and the underlying Si substrate. For the four selected NWs, we found that the absolute value of the relative change of the SThM signal ($\left|\Delta V^{rel}_{out(NWs)}\right|$) increases from $10\,mV$ to $56\,mV$ with increasing the cross-sectional size of the NWs.

Finally, the absolute thermal signals in the NWs are obtained taking into account the absolute response of the probe in the WL ($V_{out(NWS)} = V_{out(WL)} + \Delta V^{rel}_{out(NWS)}$). The surface topography indicates the presence of square-like regions where the WL vanishes leaving holes of uncovered Si substrate. The thermal profile in the uncovered Si (see Fig. 30d) displays an increase of the output voltage ($\Delta V^{rel}_{out(Si)} = 20\,mV$), which is consistent with an increased heat transfer compared to the WL. However, in non-contacting regions ($< 100\,nm$), such as the Au particles in the NWs and few anti-dots in the WL (Fig. 30b), the thermal contrast appear to be dominated by the topography related changes of the tip-sample contact geometry. Consequently, we measured mean values of the thermal response of the probe in different NWs by taking into account only the thermal signals derived from flat regions where topography induced artifacts were not apparent.

Before we analyse the thermal response of our probe in the four $Si_{1-x}Ge_x$ NWs and in the WL, we describe and estimate the thermal resistive components which contribute to the SThM signals during the thermal exchange of the thermal probe with the sample surface. Although the effect of heat transfer in the ballistic regime might be considerable at length scales comparable to phonon mean free paths of the probe and the sample material, here we assume the thermal transport as entirely diffusive. This assumption is justified as long as the system is in the steady state and the phonon mean free paths in the NWs is smaller than the contact area of the probe. Next, we

validate this assumption by comparing the experimental data and the results obtained using FEM simulations in the diffusive regime.

The measured heat flux is considered as a function of different thermal resistances, such as the thermal resistance of the probe in air environment (R_{pr}), the thermal interface resistance between the probe and materials in contact (thermal contact resistance) (R_c), and the thermal spreading resistance within the sample (R_{spr}) that include both NWs and underlying substrate (see Fig. 31). Note that the contribution of the interface resistance between the SiGe NWs and the bottom Si substrate (r_{int}) is discussed later in the text. Therefore, we divide the total Joule heat generated by the current flowing through the sensor (Q_{total}) into two pathways, $Q_{total} = Q_{ts} + Q_t$, where Q_{ts}, Q_t are heat fluxes transferred from the probe tip to the sample and to the probe base, respectively. The equivalent thermal resistance (R_{eq}) is given as follows:[120]

$$\frac{Q_{total}}{T_{sensor} - T_0} = \frac{1}{R_{eq}} = \frac{1}{R_{pr}} + \frac{1}{R_c + R_{spr}} \quad (21)$$

where T_{sensor} is the heater temperature, and T_0 is the ambient temperature.

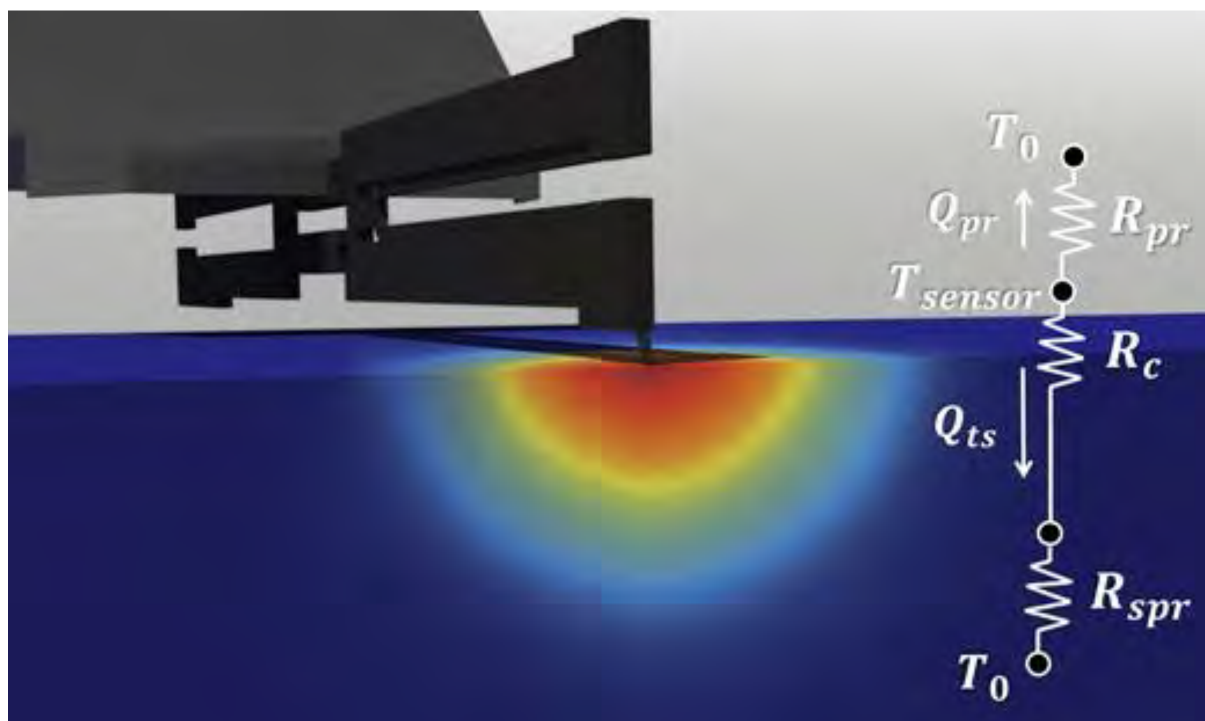

Fig. 31 Schematic of the nanoscopic tip-sample contact and the equivalent thermal resistance circuit.

Next, we estimate each thermal resistance contribution to R_{eq} using FEM simulations (COMSOL Multiphysics) and analytical models reported elsewhere.[119,121,122] The full procedure is described in detail in a separate section below. To estimate R_{pr} we used FEM simulations to calculate the temperature distribution in the thermal probe taking into account the heat transfer from the probe to the surrounding air. The value provided by the FEM model was $R_{pr} = 1.7 \times 10^6\ K\ W^{-1}$.

Since the WL is homogeneously formed on the Si substrate we can estimate the spreading resistance when the thermal probe is in contact with the WL, $R_{spr(WL)}$, from the analytical thin-film approximation derived by Dryden.[122] This model describes the spreading of heat from a circular heat source into an isotropic structure in the case that the thickness of the film is significantly smaller than the contact radius of the heat source. The obtained value $R_{spr(WL)} = 5.32 \times 10^5\ K\ W^{-1}$ is one order of magnitude larger than the spreading resistance in bulk Si ($R_{spr(Si)} = 3.37 \times 10^4\ K\ W^{-1}$) due

to the lower thermal conductivity of the SiGe alloy film forming the WL.

The magnitude of R_{spr} in different NWs is expected to vary with both, the geometrical scaling of the NWs and with possible variations of the thermal conductivity between NWs. We estimated the thermal spreading resistance variations at the probe-NWs contacts ($R_{spr(NWs)}$) first by following the same analytical film approximation for the spreading resistance.[122] Assuming a perfect thermal contact between the thermal tip and the NWs, we estimated thermal spreading resistance variations from $6.0 \times 10^5\ K\ W^{-1}$ to $3.9 \times 10^6\ K\ W^{-1}$ in a thermal conductivity range from 1 to 5 $Wm^{-1}K^{-1}$. In order to validate the estimations of R_{spr} obtained from the thin film approximation, we performed FEM simulations to compute the thermal spreading resistance variations in the four investigated NWs taking into account their real morphology ($R_{spr(NWs)}^{FEM}$). From the simulation results we found a range of R_{spr} variations, from $4.3 \times 10^5\ KW^{-1}$ to $4.4 \times 10^6\ KW^{-1}$, similar than the one derived from the analytical model.

Finally, the value of R_c, which represents the thermal resistance at the probe-sample interface, was estimated to be $9.3 \times 10^7\ KW^{-1}$ both in the WL and the NWs. The relative high value of R_c limits the sensitivity of our method, however, as explained later in the text we are able to measure small amplitude signals changes related with R_{spr} variations (see Fig. 36). The determination of R_c was possible by combining our experimental data and the calculated thermal spreading resistance variations between the WL, the NWs and the bulk Si (see separate section below). Nevertheless, we would expect R_c in the NWs and the WL to be similar since the two materials in contact were the same (Pt/SiGe contacts) during the thermal measurements and the amplitude of the contacting forces was in a similar range.

Following the identification of the heat transfer mechanisms between the thermal probe and the sample, as well as their relative weight, we discuss the variations observed in the SThM signal between different NWs. Considering that the probe Joule power dissipated into the sample is proportional to V_{out}, we correlate changes of V_{out} with

variations of the effective thermal conductance (G_{th}) between our heated tip and the sample surface (see chapter 2). The relation between the measured V_{out} and the estimated thermal resistances is shown in eq. (22) (see details in a separate section below), where we analysed the measured SThM signals by normalizing the thermal response of the probe using a ratio (g) defined as follows:

$$g = \frac{V_{out(NWs)}}{V_{out(Si)}} = \frac{R_c^{Si} + R_{spr}^{Si} + R_{pr}}{R_c^{NWs} + R_{spr}^{NWs} + R_{pr}} \propto \frac{G_{th(NWs)}}{G_{th(Si)}} \quad (22)$$

where $V_{out(NWs)}$ and $V_{out(Si)}$ represent the absolute thermal signals obtained on the $Si_{1-x}Ge_x$ NWs and the bulk Si, respectively. In Fig. 32 we show the variations of the ratio g (black spheres) as observed in the four investigated NWs, as a function of their surface to volume ratio. The observed trend suggests that the effective thermal conductance between our heated tip and the NWs ($G_{th(NWs)}$), which scales proportional with the ratio (g), increases in NWs with larger surface to volume ratio. As the width and the height of the NWs increase less heat is dissipated into the Si substrate. Figure 32 also shows the effect of the $5\,nm$ SiGe alloy WL on the SThM signal compared to the thermal signal measured in bulk Si. In the same graph, we have plotted the normalized thermal response of the probe (g_{FEM}) (red and green stars) obtained according to the calculated thermal spreading resistance values ($R_{spr(NWs)}^{FEM}$), as a function of the surface to volume ratio of the NWs for a direct comparison with the experimental data.

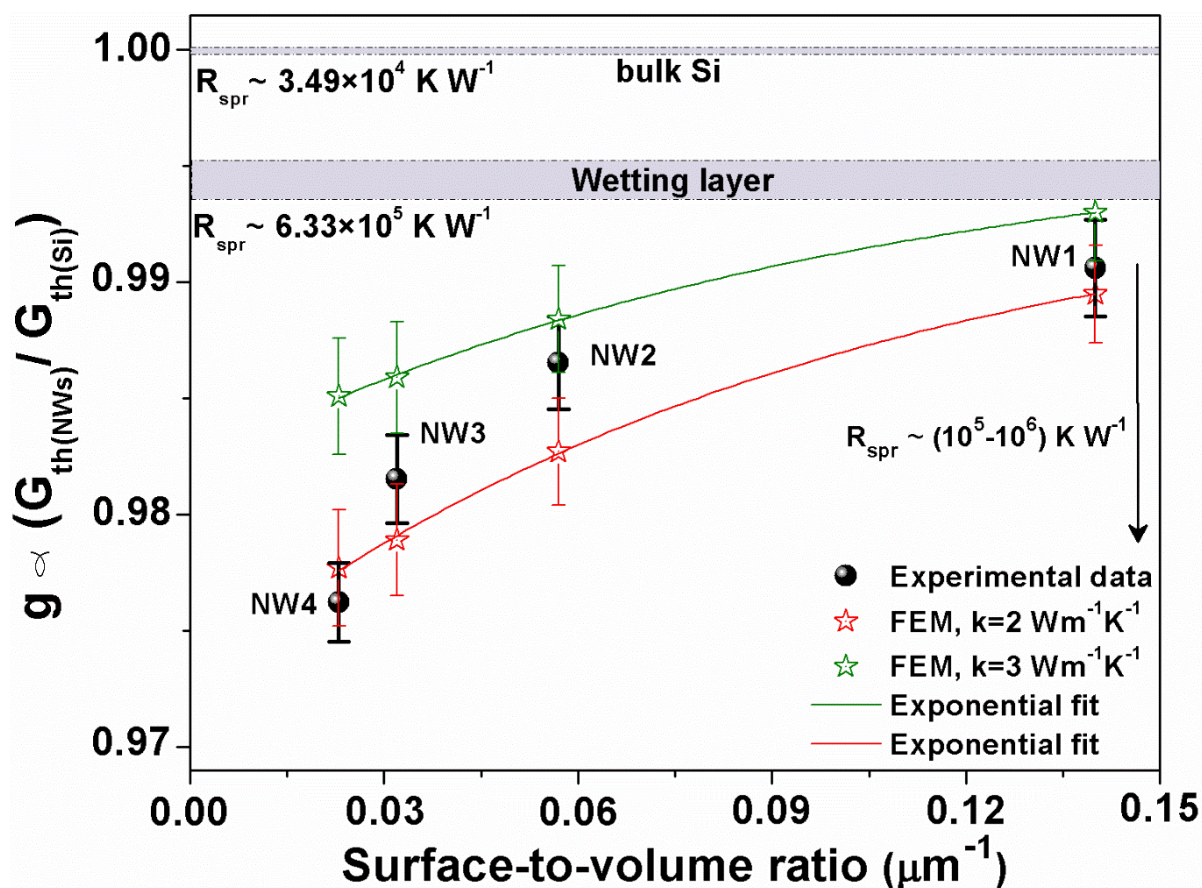

Fig. 32 Plot of the experimental thermal ratio (g) (black spheres) and the ratio obtained from the FEM simulations (g_{FEM}) (red and green stars) versus the surface to volume ratio of the $Si_{1-x}Ge_x$ NWs.

The obtained trend of the ratio g is consistent with the analog picture of a lower conductive layer on top of a higher conductive substrate and a diffusive thermal transport, where one would expect an increasing thermal resistance with increasing layer thickness. The comparison in Fig. 32 demonstrates a quantitative agreement between the FEM simulations, which takes into account only R_{spr} variations, and our experimental results, confirming that despite R_c is the dominant resistive component the variations in the thermal response of the probe between the NWs is most likely associated with variations in R_{spr}. The changes of R_{spr} which are found to be dominant compared to the deviations of R_c are shown in a separate section below (Fig. 35). The small deviations between the modelling and the experimental data can be attributed to composition variations

in the NWs, which were not taken into account in the FEM simulations (e.g. presence of Au and SiGe composition).
Recalling the results from the composition analysis (Fig. 29b), it is interesting to note that in the NWs with relative high Au concentration (NW3, NW4) the deviations between experimental data and simulations become larger (see green line and the experimental data in Fig. 32). The increased Au concentration in these cases generates a nanoscale disorder in the SiGe lattice and increases the number of phonon scattering events. We consider the concentrated Au atoms as an additional thermal resistive layer which potentially reduces the average Λ in the NWs and further suppress the heat dissipation perpendicular to the substrate. Similarly, it was found that nanodot layers, such as interfaces, or surface doping and defects in semiconductor nanostructures, introduce enhanced phonon scattering and phonon trapping at localized vibrational modes.[123-127] Moreover this mechanism can effectively suppress the transport of long-wavelength phonons and, therefore, the ballistic transport.

Finally, in order to assess the effect of an interfacial thermal resistance, (r_{int}), between the NWs and the substrate, an extension of the thin film approximation model previously explained can be derived taking into account the interface effect on the thermal spreading resistance[128]. As precisely knowing this parameter is difficult in the particular NW geometry, we used a wide range of values around reported measurements[123,129,130] and investigated its effect on the ratio g for each NW. Values of interfacial thermal resistance between 0 and $1 \times 10^{-8}\ m^2KW^{-1}$ were chosen and set in the analytical modelling. Then we fit the experimental data and obtained a thermal conductivity for the NWs. The results are plotted in Fig. 33. The first observation was that the overall trend of the modelled ratio g is similar (1% variations) for the different values of r_{int}. Furthermore, the discrepancy between the model and the data increased with increasing interfacial thermal resistance. This supported the explanation described below that the variation of the data to the model is more likely due to Ge composition variations and Au content. Secondly, the thermal conductivity obtained by fitting varied from 1 to 2 $Wm^{-1}K^{-1}$, which are still close to the values

discussed before. This range represents the thermal conductivity of the NWs taking into account the underlying interface with the substrate.

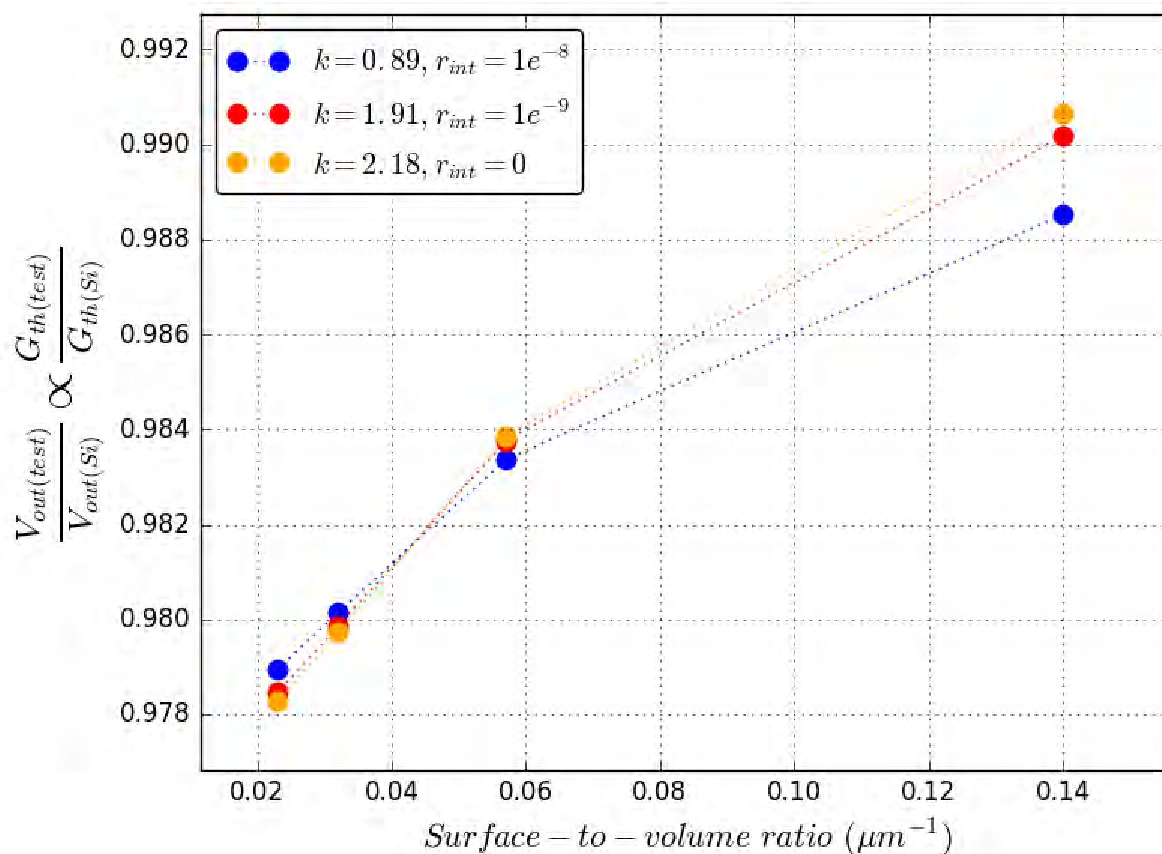

Fig. 33 Effect of the interface thermal resistance between the $S_{1-x}Ge_x$ NWs and the Si substrate in the normalized thermal response of the probe.

According to the previous analysis we could estimate that the thermal conductivity of the four NWs is varying in a range between 2 and 3 $Wm^{-1}K^{-1}$, which represents a thermal conductivity almost four times lower than the bulk value.[123] This range is similar to the values expected in SiGe nanostructures of similar characteristic size and composition, where the reduction of the thermal conductivity has been attributed to phonon boundary scattering.[115,116,127,131-135]

Estimations of thermal resistances with the thin film approximation

We calculate the thermal spreading resistances from an approximate analytical model for a layer on a substrate. Taking into account that the thickness of the WL (5 nm) is significantly smaller than the contact radius of our heat source (100 nm), we estimate the thermal spreading resistance in our sample surface ($R_{spr(WL)}$) as follows:[122]

$$R_{spr(WL)} = \frac{1}{4k_{Si}r_t} + \frac{1}{4k_{WL}r_t}\left(\frac{t_{WL}}{r_t}\right)\left[1-\left(\frac{k_{WL}}{k_{Si}}\right)^2\right] \qquad (23)$$

where the first term is the spreading resistance within the Si substrate and the second term is a correction factor that accounts for the effects of the wetting layer thickness (t_{WL}) and the ratio of the thermal conductivities of the WL (k_{WL}) and the bulk Si (k_{Si}), respectively. Note that in order to estimate the spreading resistance in the bulk Si ($R_{spr(Si)}$), we use the same expression taking into account only the first term as reported elsewhere.[121,122] We calculate $R_{spr(WL)} = 5.32 \times 10^5\ K\ W^{-1}$ and $R_{spr(Si)} = 3.37 \times 10^4\ K\ W^{-1}$ using $k_{WL} = 1\ Wm^{-1}K^{-1}$ [132-134] and $k_{Si} = 148\ Wm^{-1}K^{-1}$, respectively. The spreading thermal resistance (R_{spr}) at the contact of the thermal probe with the relatively thick NWs (NW2, NW3, and NW4) is estimated using the following analytical expression:[122]

$$R_{spr(NWs)} = \frac{1}{4k_{Nwi}r_t} - \frac{1}{2\pi k_{Nwi}r_t}\left(\frac{r_t}{h_{Nwi}}\right) ln\left(\frac{2}{1+\frac{k_{Nwi}}{k_{Si}}}\right) \qquad (24)$$

where the first term is the constriction resistance within the NWs and the second term is the correction factor due to the relative NWs height (h_{Nwi}) and the ratio of the thermal conductivities of the NWs and the Si substrate (k_{NWs}/k_{Si}). In the case of the thinnest nanowire (NW1) and due to the relative small height compared to the tip radius, we use eq. (23). Figure 34

summarizes the spreading thermal resistances calculated according to eq. (23) and eq. (24) for different values of k_{NWi} taking into account that the unknown thermal conductivity of the NWs has to be lower than in the bulk $Si_{1-x}Ge_x$ ($k_{NWs} < k_{bulk(SiGe)}$).[135] Considering that the thermal spreading resistance in the NWs cannot be lower than the value of the spreading resistance of the WL, as inferred from our measurements, the thermal spreading resistance values have to lie in the range of $6.0 \times 10^5\ KW^{-1}$ to $3.9 \times 10^6\ KW^{-1}$, approximately, and therefore the thermal conductivity of the NWs cannot exhibit values larger than 5 $Wm^{-1}K^{-1}$.

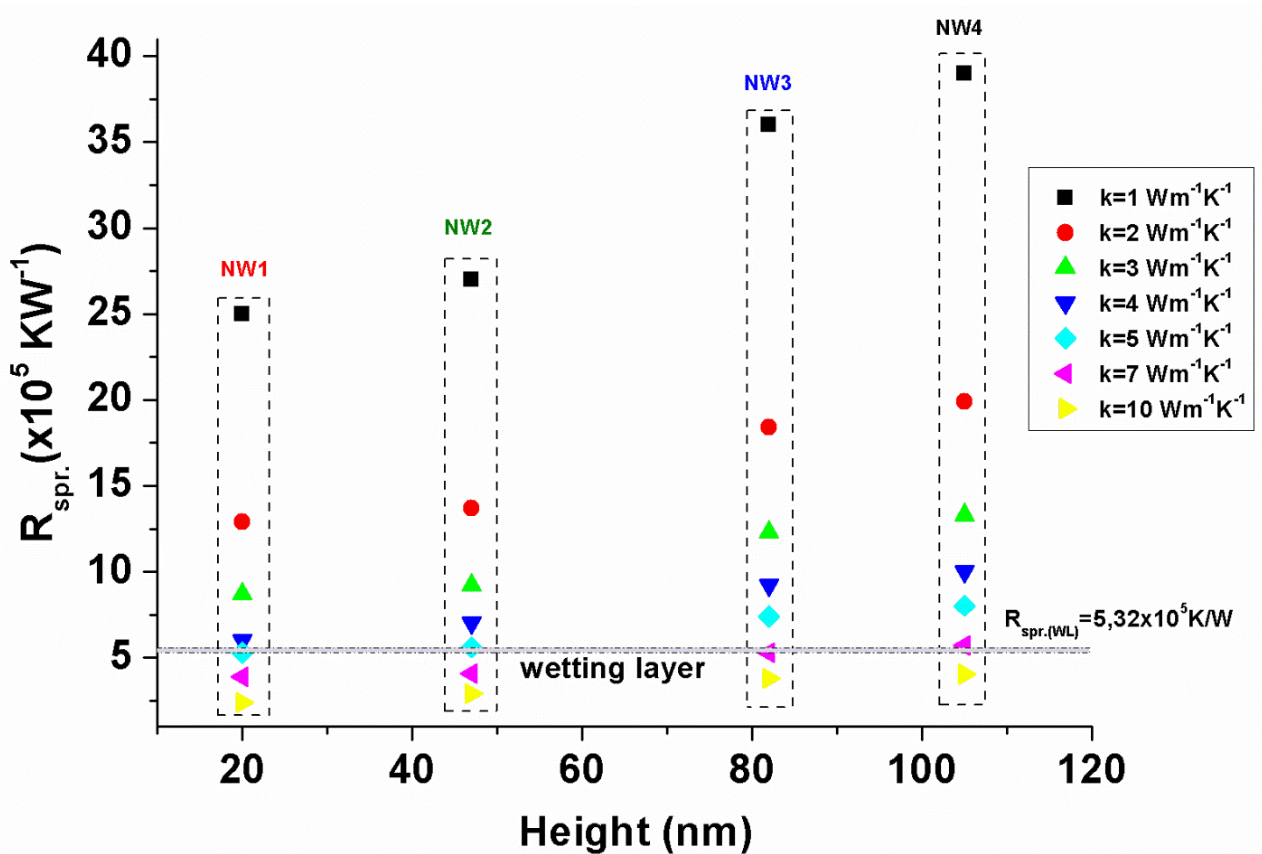

Fig. 34 Estimation of the thermal spreading resistance (R_{spr}) at the contact of the thermal probe with the four NWs for different values of k_{NWs}.

Relation between the SThM signal and the thermal resistances

First, we correlate the contact temperature (T^c) with the absolute output voltage with the following relation:

$$V_{out}(T) = \alpha(T^c - T^{nc}) \quad (25)$$

where T^{nc} is the out-of-contact temperature and α a negative proportional factor with unit V/K. Note that high thermal conductive materials produce lower T^c and proportionally higher V_{out}. The Power P dissipated from a heat source to a heat sink is related to the thermal effective resistance R_{th} by the temperature difference between the source T and the heat sink T_0 as:

$$\frac{T - T_0}{P} = R_{th} \qquad (26)$$

Considering the probe out and in contact with the sample, T^{nc} and T^c can be expressed according to eq. (25) as $T^{nc} = PR_{pr} + T_0$ and $T^c = PR_{eq} + T_0$, respectively. The equivalent thermal resistance (R_{eq}) according to the thermal resistance circuit in Fig. 33 can be written as follows:

$$R_{eq} = \frac{(R_c + R_{spr})R_{pr}}{R_c + R_{spr} + R_{pr}} \qquad (27)$$

When the measurements are performed in air, the thermal contact resistance at the probe–sample interface (R_c) can be written as:

$$R_c = \frac{R_{air}R_{ss}}{R_{air} + R_{ss}} \qquad (28)$$

where R_{air} and R_{ss} are the thermal resistances in parallel due to air conductance from the tip to the sample and the conductance due to solid-solid contact between probe and sample, respectively. Using the expressions of T^{nc}, T^c and R_{eq} in eq. (25), we obtain the relation between the measured V_{out} and the different thermal resistances ($V_{out}(T) = \alpha P(R_{eq} - R_{pr})$). Therefore, the ratio of the thermal response of the probe on a tested sample related to bulk Si is written as follow:

$$\frac{V_{out(test)}}{V_{out(Si)}} = \frac{R_{eq}^{test} - R_{pr}}{R_{eq}^{Si} - R_{pr}} = \frac{R_c^{Si} + R_{spr}^{Si} + R_{pr}}{R_c^{test} + R_{spr}^{test} + R_{pr}} \qquad (29)$$

Next, we estimate R_c from eq. (29) assuming that $R_{c\,(Si)} \approx R_{c\,(WL)}$ and using as inputs the measured value $\frac{V_{out(WL)}}{V_{out(Si)}} = 0.9937$ and the calculated values $R^{FEM}_{spr\,(Si)}$, $R^{FEM}_{spr\,(WL)}$ and R_{pr}. This gives a thermal contact resistance $R_{c\,(Si)} \approx R_{c\,(WL)} = 9.3\ \times 10^7\ KW^{-1}$. Taking this value as a reference and using as inputs in eq. (29) the measured ratios $g = \left(\frac{V_{out(NWs)}}{V_{out(Si)}}\right)$ and the estimated $R^{FEM}_{spr(NWs)}$ and $R^{FEM}_{spr(Si)}$, we calculated almost one order of magnitude smaller R_c variations between the four NWs ($\Delta R_{c\,(NWs)} = 0.029 \times 10^7\ KW^{-1}$) compared to the variation of the spreading resistance ($\Delta R_{spr(NWs)} = (0.08 - 0.12)\ \times 10^7\ K\ W^{-1}$). In Fig. 34 we compare the variations of R_{spr} and R_c in the four NWs.

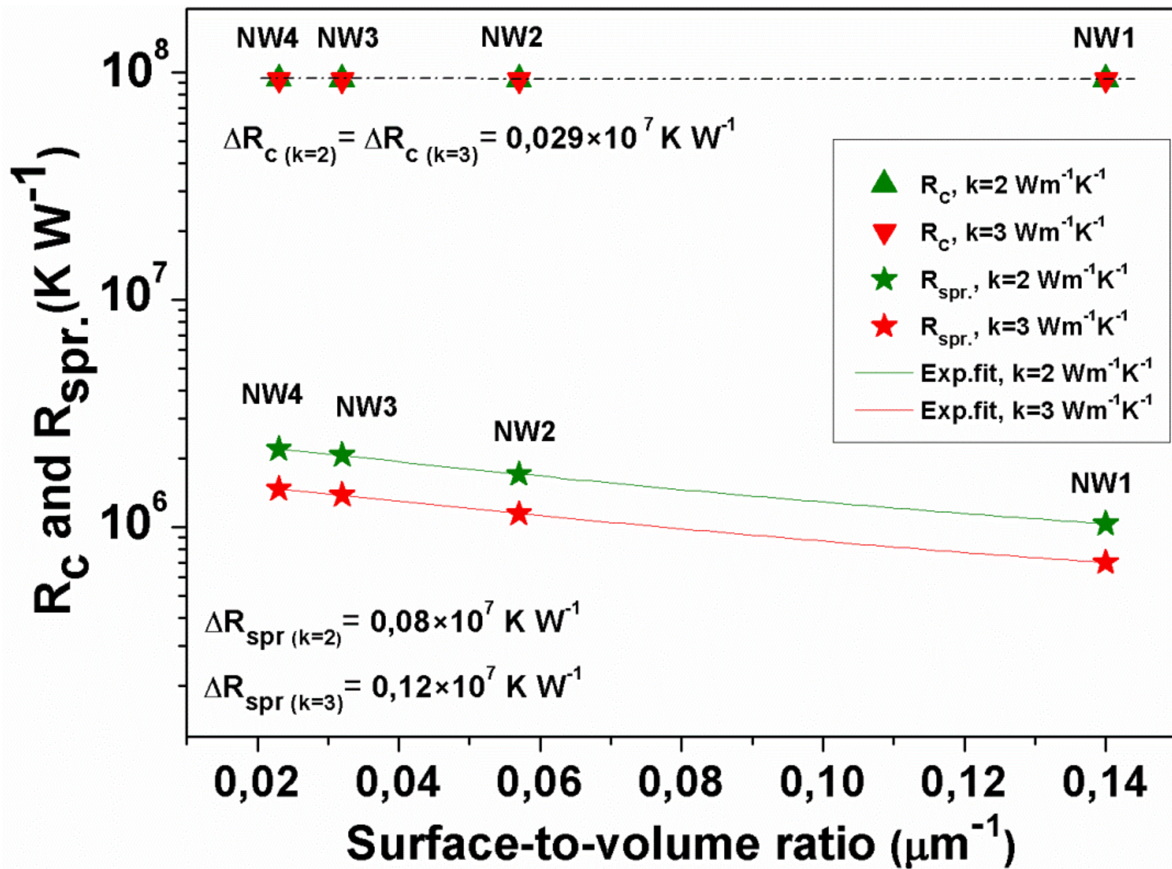

Fig. 34 Thermal contact resistance and thermal spreading resistance at the contact of the thermal probe with the four NWs for different combinations of k_{NWs}.

In order to understand better the probe's behaviour and sensitivity to R_{spr}, we plot eq. (29) for different values of $R_{spr(test)}$ ($10^4 - 10^{10}\ KW^{-1}$). The graph in Fig. 35 shows the sensitivity of the probe in thermal spreading resistance variations. According to our previous calculations through FEM simulations, in the NWs we expect thermal spreading resistance variations from $4.3 \times 10^5 K\ W^{-1}$ to $4.4 \times 10^6\ K\ W^{-1}$. In this range the thermal probe is sensitive to R_{spr} variations as is shown in Fig. 35. For R_{spr} > $10^6\ KW^{-1}$, R_{spr} becomes comparable to R_c and the normalized response changes more rapidly, thus the probe becomes more sensitive to R_{spr} variations.

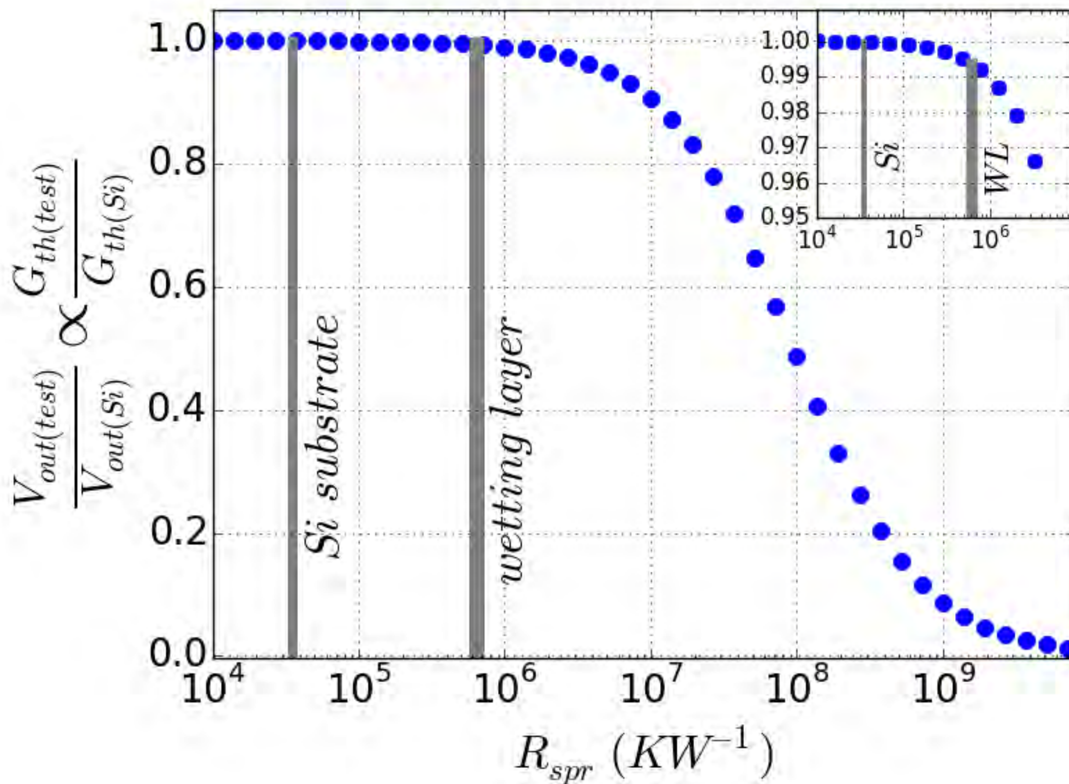

Fig. 35 Sensitivity of the probe to thermal spreading resistance (R_{spr}) variations.

Finally, we compute the normalized thermal response of the probe in the four investigated NWs using as inputs in eq. (29) the calculated $R^{FEM}_{spr\ (NWs)}$ and the estimated values of R_c and R_{pr}. The results are shown in Fig. 36 where we plot the ratio $g_{FEM} = \left(\frac{V_{out(NWs)}}{V_{out(Si)}}\right)_{FEM} \propto \left(\frac{G_{th(NWs)}}{G_{th(Si)}}\right)_{FEM}$ as a function of the surface to volume ratio of the $Si_{1-x}Ge_x$ NWs. Note that the

differences between the NWs originated only from R_{spr} variations. The comparison with the experimental data is shown before (Fig. 32), where the values of g_{FEM} are plotted for $k_{NWs} = 2\, Wm^{-1}K^{-1}$ and $k_{NWs} = 3\, Wm^{-1}K^{-1}$.

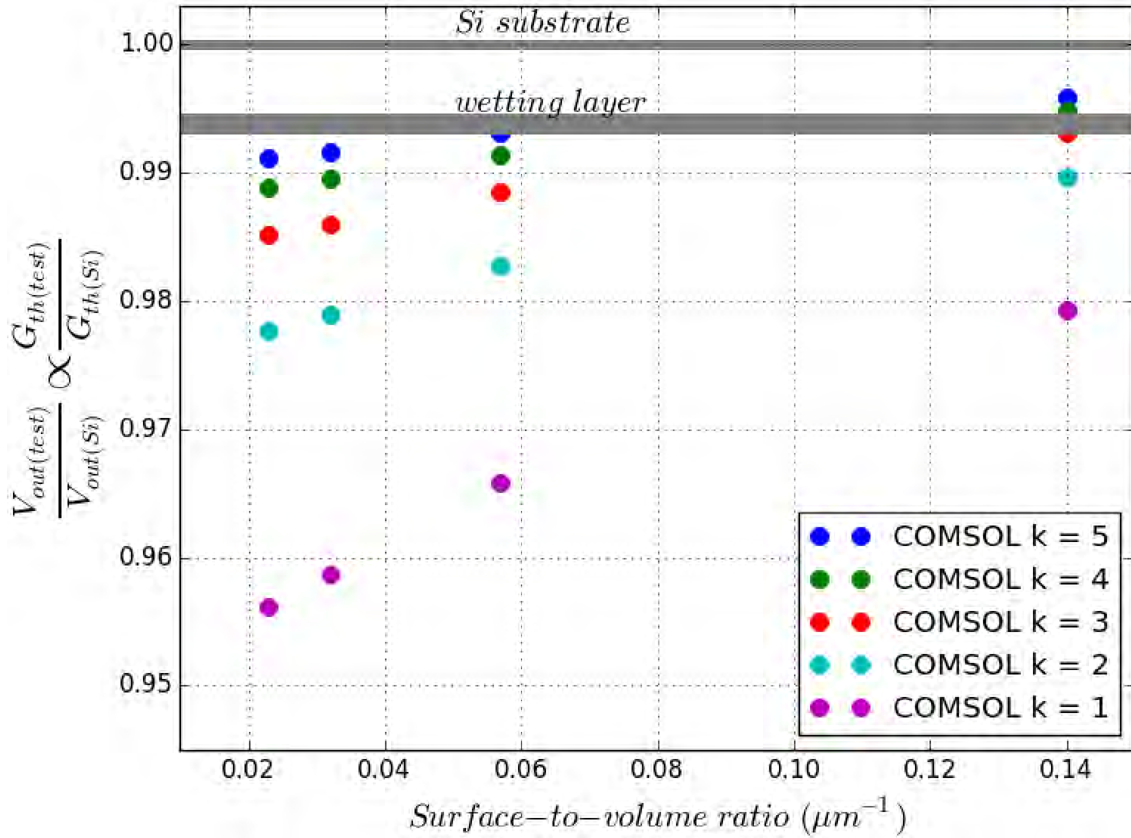

Fig. 36 Normalized thermal response of the probe (g_{FEM}) according to FEM simulations for different combinations of k_{NWs} versus the surface to volume ratio of the $Si_{1-x}Ge_x$ NWs.

In summary, in this chapter we presented a comprehensive experimental study regarding the structure and the composition of supported in-plane epitaxial $Si_{1-x}Ge_x$ alloy NWs of different dimensions providing a deeper understanding of the bottom-up growth processes. We have presented new evidences regarding the morphology of the NWs, their size-dependent gradient composition and the formation of a $5\,nm$ thick WL on the substrate surface. In addition, we have studied the thermal transport between the heated tip of a scanning thermal microscope and the sample surface. SThM has provided high resolution thermal contrast images of sub-

micrometre structures on the sample surface with sub-100 nm spatial resolution. By estimating all the major thermal resistive components contributing to the SThM signals at the probe-sample contacts and determining the dominant mechanisms, we have been able to analyse the experimental thermal response. Particularly in the NWs, we found that the heat flux related signals are modulated by thermal spreading resistance variations, revealing the relation between the measured SThM signals and the effective thermal conductance. The results obtained using FEM simulations, which are in good agreement with the experimental results, allowed us to determine a range of thermal conductivities $(2-3\,Wm^{-1}K^{-1})$ for the investigated NWs. Our analysis indicates that even for nanometer scale heat sources and low conductive materials, heat dissipation can be consistently explained with a diffusive thermal spreading model.

5

Self-assembled block copolymer nanostructures

Micro-phase separation of block copolymers (BCPs) is being explored as a promising method to provide nanometer-scale features in lithographic processing, allowing the production of complex devices for integration in emerging areas of nanotechnology, such as, advanced electronics, optoelectronics and high density data storage.[68,136-139] The characteristic features sizes of these devices are only limited by the size of the copolymer chains ($(5\text{–}20)\ nm$). For example, block copolymer thin films has been used for patterning of microelectronics components on a length scale inaccessible by optical lithography e.g., fabrication of high density hard drives.[136] More recent application are based on the ability to template the block copolymer directly.[139] For instance, poly(ethylene oxide) (PEO) containing block copolymers may be useful as the electrolyte layer of a battery or fuel cell, particularly if the electrolyte channel can be patterned in a particular orientation[136]. Furthermore, the selective incorporation of evaporated metal particles on phase-separated BCPs can be used for the production of various nanostructures, e.g., conductive nanowires[140] or for the formation of hard masks, desirable, for example, in reactive-ion etching process. Several works have reported successful templating of various metallic elements, which selectively covers one of the blocks.[140-144]

In addition, polymers can be used in heat transfer applications, such as microelectronics thermal management. For example, Polydimethylsiloxane (PDMS)-based polymers have been used as thermal interface materials in computer microprocessors and passive heat spreaders in electrical components.[145,146] The possibility given by nanostructuring polymers of

further lowering its thermal conductivity and combining them with heat conductive materials, opens new prospects in the control of heat transport. Therefore, thermal characterization of systems composed of polymers is potentially of high interest.

The subject of self-assembly in microphase separated BCPs has been investigated in this thesis with two motivations. The first is exploring the self-assembly of BCPs as a method to provide nanometer-scale features in lithographic processing, therefore potentially allowing the patterning of features smaller than the obtained by e-beam lithography. The second is the study of the thermal properties of BCPs and the effect of the incorporation of evaporated metal films. Besides studying the heat transfer in thin films and at interfaces of materials with dissimilar thermal properties, these samples could also be valuable for nanometrology purposes, as they pose major challenges regarding spatial thermal resolution and probe sensitivity to changes of the thermal property. In this chapter we present the thermal conductance studies in self-assembled polystyrene-block-poly (ethylene oxide) (PS-b-PEO) films. We studied two different morphologies of the BCP films, and the effect of coating. In addition, by combining thermal annealing and selective chemical treatment we study the possibility to modify the morphology of the BCP templates by re-arranging the position of the PEO cylindrical domains in-plane on the PS polymer matrix surface. Next, only the preliminary results of this study are presented since further measurements and simulations are in progress.

5.1 Preparation of block copolymer templates

A solution of PS-b-PEO diblock copolymer with molecular weights of $M_{n,PS} = 102\ kg/mol^{-1}$ and $M_{n,PEO} = 34\ kg/mol^{-1}$ was dispersed onto a Si substrate, spin-coated at 3000 RPM for 60 sec and thermal annealed at 90 °C for 160 minutes. The microphase separation of the BCP film resulted in the formation of vertical oriented PEO cylinders showing a hexagonal arrangement and embedded in a PS matrix. A schematic illustration of the fabrication process is shown in Fig. 37a. The average radius of the cylinders and the average spacing between them are of about $r = 15 \pm 2\ nm$ and $D = 25 \pm 2\ nm$, respectively (Fig. 37b). Then, by using electron beam

evaporation, Cr layers with different nominal thicknesses (1, 2 and 5 nm) were coated on the surface of the BCP film, expecting, from the surface selectivity, the formation of a metal porous layer (see Fig. 37a). Figures 37c-e illustrate SEM images of the surface of the three BCP templates after the evaporation of Cr layers. The lighter coloured areas correspond to the PS matrix with Cr coating and the darker areas to the PEO blocks of the BCP film. A second set of BCP templates was prepared with the same procedure as before. It was then processed by combining thermal annealing and selective chemical treatment in controlled chloroform and toluene atmosphere. Figure 37f shows the modified BCP template with the PEO cylindrical domains rearranged in-plane on the surface of the PS matrix. Then, similarly, Cr layers with nominal thicknesses of 2 and 5 nm were evaporated on the surface of the film by electron beam evaporation (see Fig. 37g,h). The enhancement of the orientation of the PEO domains can be achieved either by controlling the solvent evaporation environment[136,147] or by pre-coating the underlying substrate with a homopolymer buffer layer[134,148] in order to reduce the interaction with the coated BCP film.

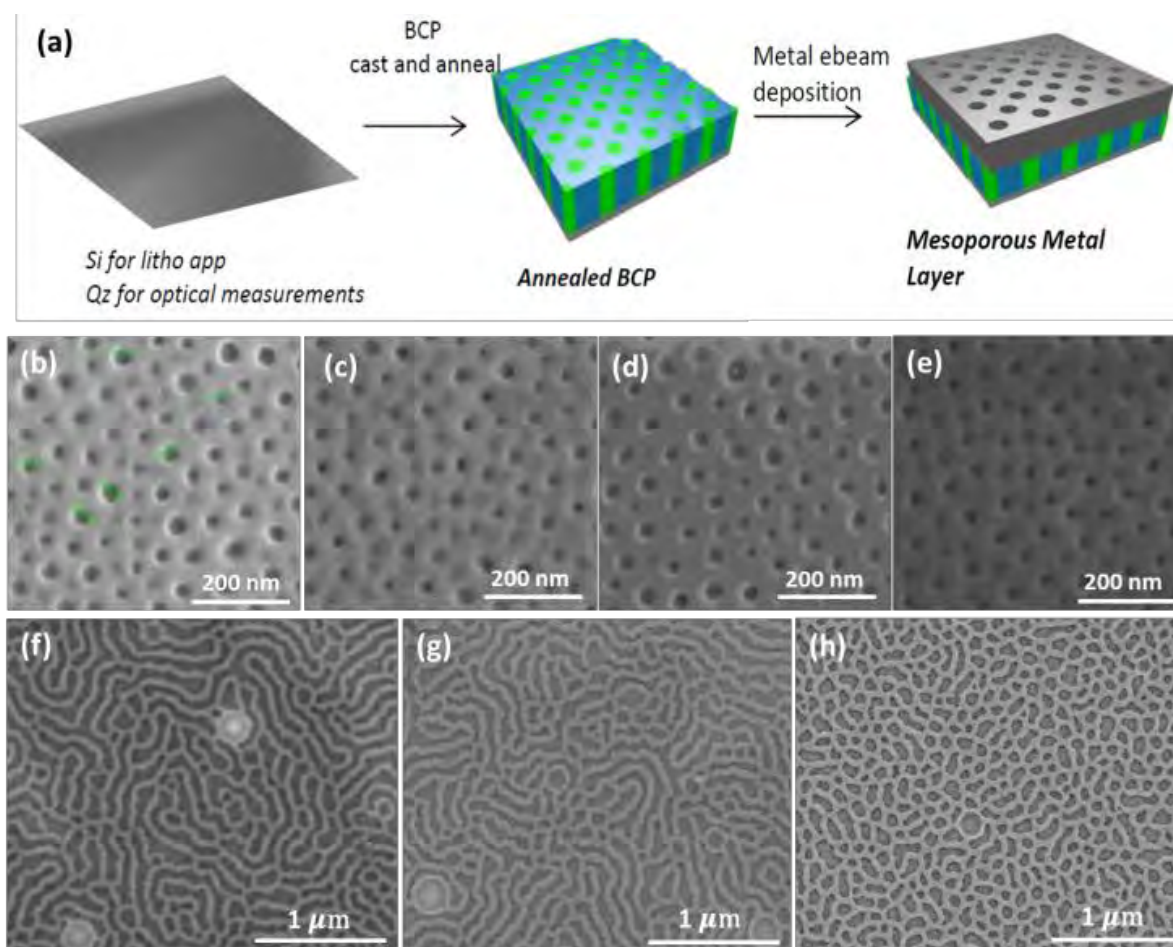

Fig. 37 (a) Schematic illustration of the fabrication process. SEM images of (b) the fabricated microphase separated BCP film on Si substrate and the BCP templates with nominal Cr coatings of (c) 1 nm, (d) 2 nm and (e) 5 nm. (f) The fabricated BCP template after the chemical treatment showing the modified morphology and the BCP templates with (g) 2 nm and (h) 5 nm Cr layers.

5.2 Structural characterization

Figure 38 shows AFM images of the first set of BCP templates. In the BCP template without the Cr layer, the average height between the two different phases, namely PEO cylinders and PS matrix, was $5 \pm 2\,nm$. The RMS surface roughness decreases from 3 to $2\,nm$ with increasing Cr layer thickness.

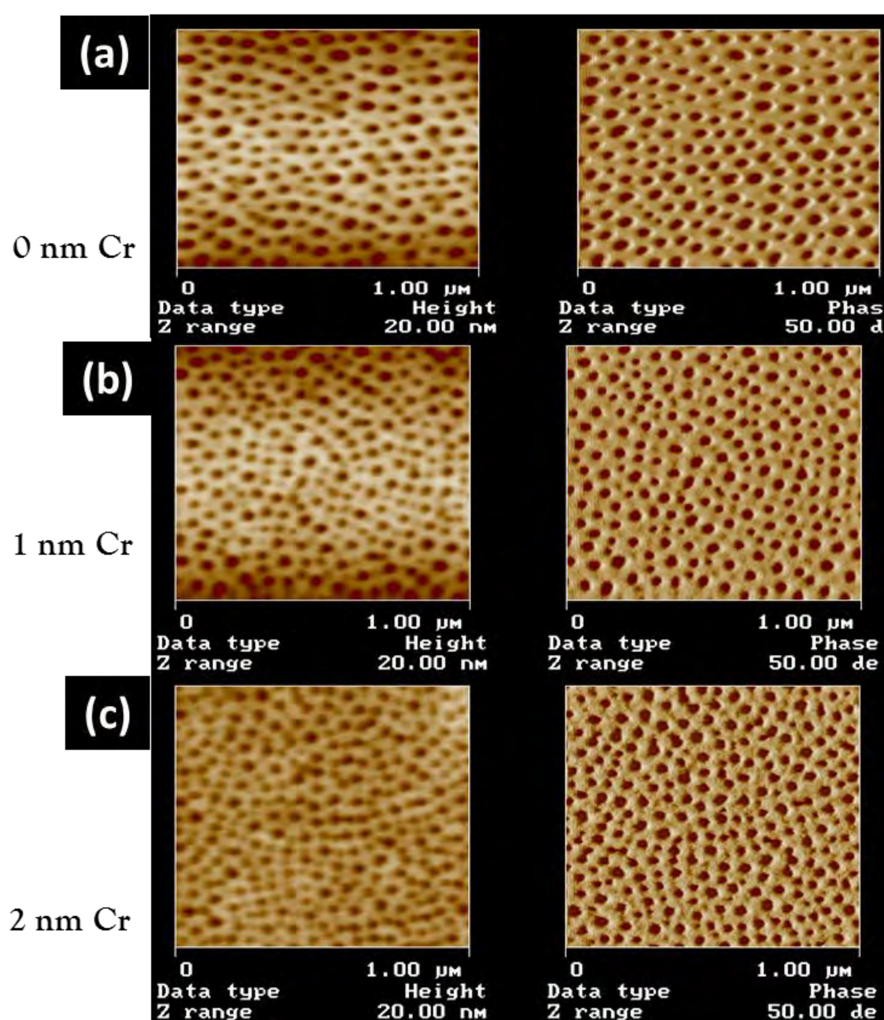

Fig. 38 AFM images of the BCP templates: (a) Pristine Sample, (b) after depositing 1 nm Cr, (c) after depositing 2 nm.

Figures 39a-c show cross-section TEM images of the BCP templates with nominal Cr coatings of 1, 2 and 5 nm, respectively. The cross-sectional TEM shows an increase of the Cr layer thickness in both PS and PEO phases. The evaporated Cr atoms formed a homogeneous Cr layer on the PS matrix top surface and incorporated within the PEO domains. The BCP template with 2 nm thick Cr is shown in STEM mode in Fig. 39d. Figure 39e shows the selected area in Fig.39d with higher magnification. The EDX spectrum taken along the line indicated in Fig.39e confirmed the existence of Cr atoms on top of the PS surface and on the PEO domains as well (see Fig. 39f). The BCP film thickness was measured to be $40 \pm 2\ nm$ and the step between the two phases is found to be deeper than seen in AFM analysis.

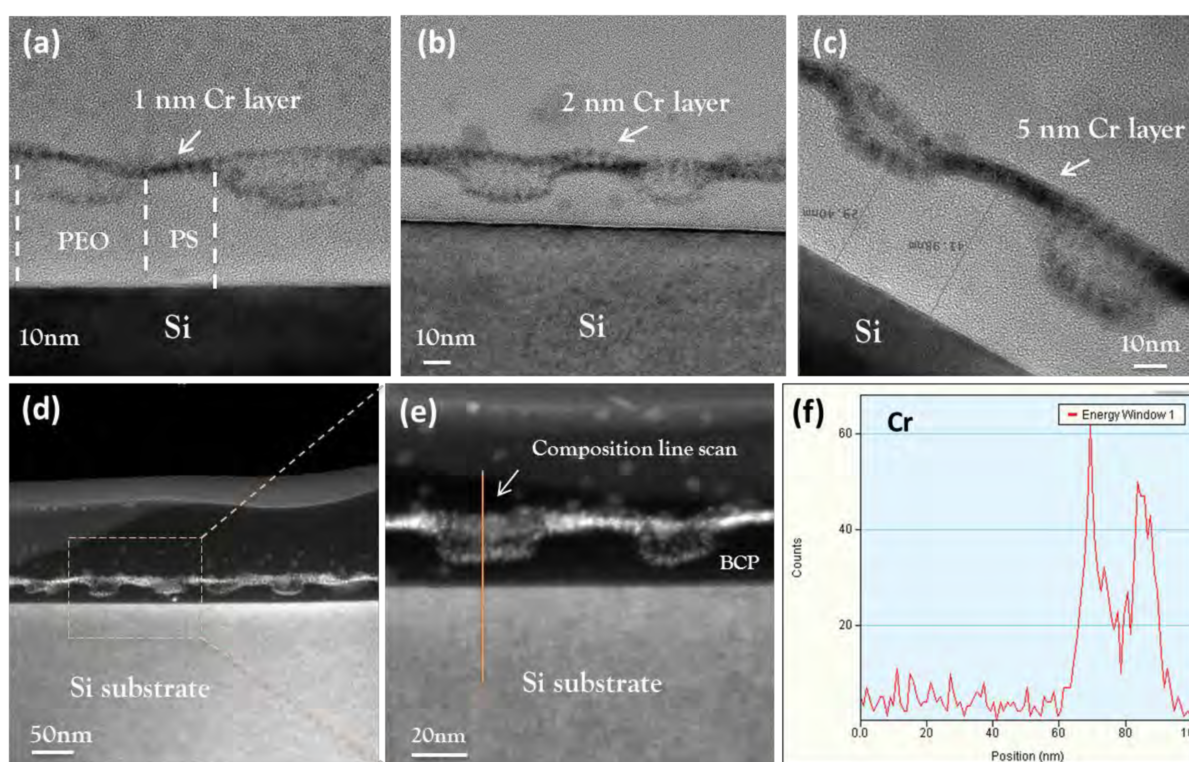

Fig. 39 TEM images of the BCP templates with nominal Cr coatings of (a) 1 nm, (b) 2 nm and (c) 5 nm. (d), (e) High resolution images in STEM mode of the BCP template with 2 nm Cr layer and (f) vertical EDX line scan along to the PEO phase.

High-resolution TEM images of the modified morphology of the BCP templates (second set of samples) with nominal 2 and 5 nm thick Cr layers are shown in Fig. 40a,b and Fig. 40c,d, respectively. TEM images are difficult to interpret and the identification of the different phases is unclear,

therefore we do not have a clear picture of the morphology of the BCPs. In addition, it seems that there is not selectivity in the deposition of the Cr layer, i.e., a homogeneous Cr layer all along the sample surface. We performed EELS composition maps in order to gain insight into the arrangement of the polymers in the sample. Figure 41a shows the selected area in the BCP template with 2 nm Cr layer for the composition analysis (orange box). Figures 41b,c show the EELS composition maps for oxygen and chromium elements, respectively. As already seen in the TEM images, Fig. 41b shows that the Cr layer is homogeneously distributed on top of the BCP surface without showing any selectivity. Oxygen content (brighter regions in Fig. 41c) is clearly detected at the substrate-BCP interface and at the Cr layer. The former is attributed to the native SiO_2 film formed on top of the Si substrate and the latter reveals that the Cr layer is oxidized. In the BCP layer, there is no noticeable image contrast regarding the oxygen concentration and, therefore, the precise morphology of the BCP cannot be disentangled.

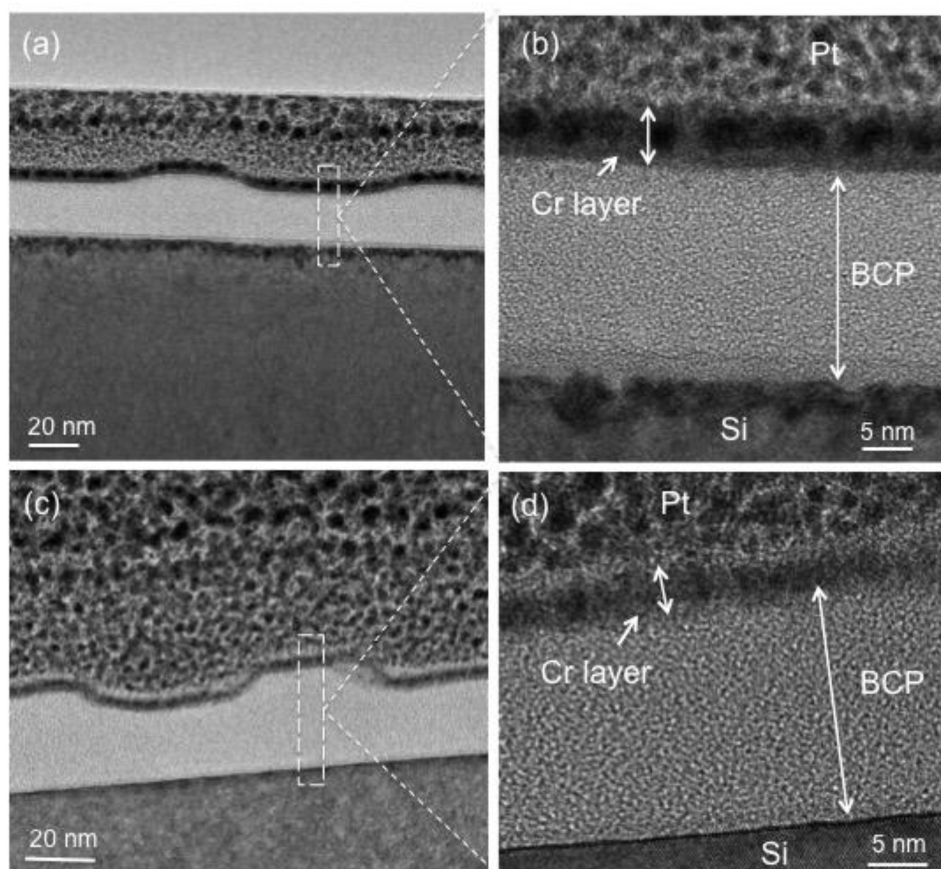

Fig. 40 TEM images of the (a), (b) 2 nm Cr and (c), (d) 5 nm Cr covered BCP templates (set of samples showing lamella morphology)

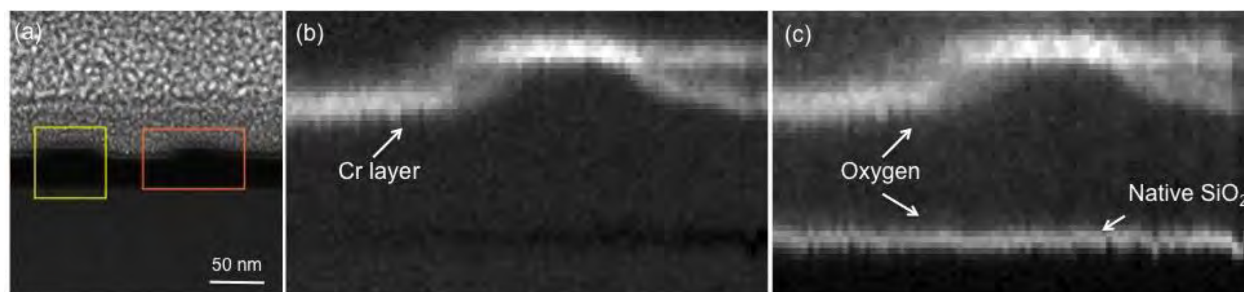

Fig. 41 (a) STEM image of the BCP template with 2 *nm* Cr. (b), (c) EELS composition maps showing the spatial distribution of Cr and O, respectively.

5.3 SThM measurements

Recent studies of the thermal properties of polymer have shown the importance of thickness reduction in polymer films[149] and chain alignment.[150] In contrast, thermal transport in BCP films has been barely explored. George *et al.*[151] reported thermal transport measurements on BCP films containing PS and PMMA polymers (PS-b-PMMA). They found that neither the film thickness nor the blocks phase separation influenced the thermal conductivity of the BCP, obtaining values consistent with the bulk homopolymer values. The thermal conductivity of BCP films has not been studied in detail in the literature. Only few works reported thermal conductivity measurements on BCP films containing PS and PMMA polymers (PS-b-PMMA), where it has been found that the BCP films exhibit thermal conductivity values similar to the bulk homopolymer values.
Considering the thermal imaging capabilities of the SThM technique, it would be interesting to study not only the thermal conductivity of the BCP films, but also individual regions to understand how the interfaces between the two blocks and the reorganization of their chains around these interfaces affect the thermal conductance.

Regarding the first set of sample, SThM measurements performed using three different thermal probes and experimental setups in ambient conditions during my research stay in the University of Lancaster (ULANC) and the Centre for Energy and Thermal Sciences in Lyon (CETHIL). In addition, for this set of sample, in the ULANC we performed SThM measurements in vacuum conditions and thermal mapping in ambient air.

For the second set of sample both, SThM measurements and thermal mapping performed in vacuum conditions in the ULANC. The SThM setup used in ULANC is described in the experimental methods (chapter 2). Details about the experimental setup in CETHIL can be found elsewhere.[53]

Thermal conductance measurements and thermal imaging in BCP templates in ambient air environment

SThM point measurements were performed in ambient air conditions ($T = 24\ ^0C$) in order obtain the thermal response of the resistive probes in the BCP templates. Following the methodology described in chapter 2, we measured the voltage variation ($\mathrm{d}V$) of the probe in and out of contact with the sample, which is proportional to the thermal conductance, for three different thermoresistive probes, namely, Pt, doped Si and palladium (Pd) probes (see chapter 2). SEM images of the three different SThM probes are shown in Fig. 42a,b,c. The SThM measurements presented in Fig. 42d,e,f show that the thermal probes are sensitive to the metal layer thickness, following a similar trend, i.e., the effective thermal conductance decreases as the metal film thickness increasing. Each point is obtained by averaging ten consecutive point contact measurements and the error bars represent the dispersion of the values of the ten measurements.

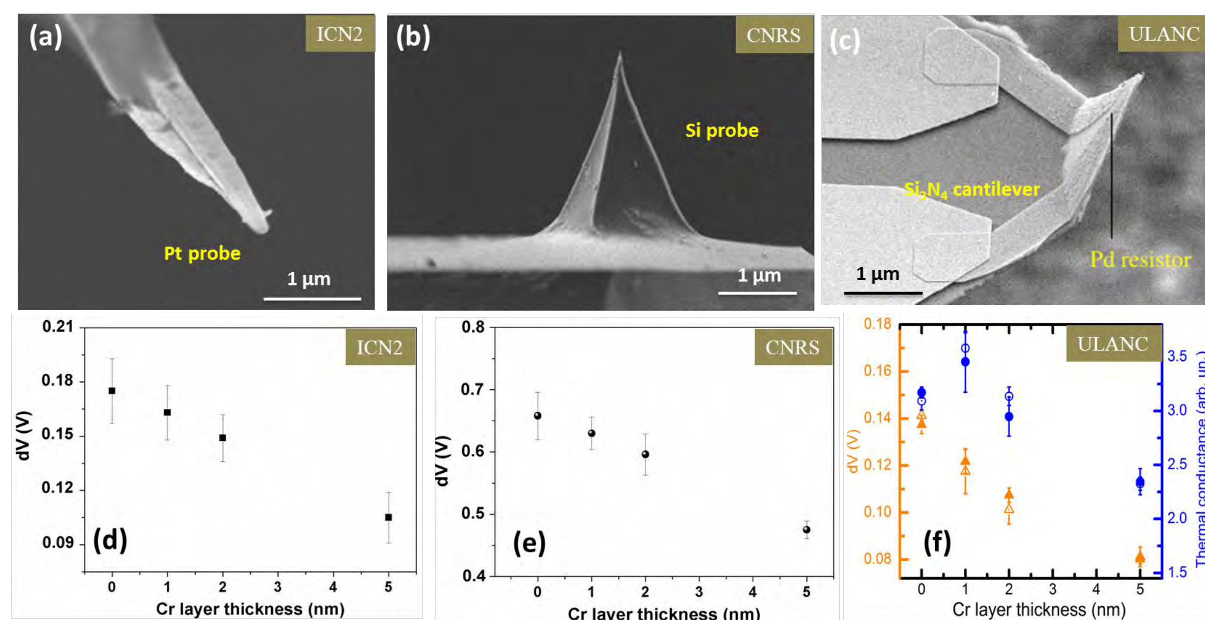

Fig. 42 SEM images of (a) Pt, (b) doped Si and (c) Pd resistive thermal probes. SThM signals as a function of the Cr thickness, for each of the probes (d), (e) and (f).

A possible explanation of the decrease of the thermal conductance with the layer thickness is related to the substrate effect, and will be explained in the next subsection. From the analysis of the topography of the samples, presented in the previous section, we rule out the possibility that this effect originates from an increase of the surface roughness. Note that the measurements in Fig. 42 are related to the relative dissipated power of the probes in contact with the BCP templates. The determination of the thermal conductivity requires a specific thermal model adapted to each experiment as discussed previously.

Figure 43 illustrates examples of topography and thermal images of the BCP surface with the 5 nm Cr layer measured in the setup of ULANC with the Pd probe. The discrimination of the two phases was not possible probably due to the large contact area of the probes and/or the existence of liquid meniscus in the tip apex, which usually limits the thermal spatial resolution. Note that the hydrophilic nature of the BCPs makes the imaging even more challenging. In addition, we found that the BCP surface was modified after imaging as is shown in Fig. 43. In order to increase the thermal spatial resolution of the SThM measurements, we performed thermal measurements in high vacuum environment and sharper tip.

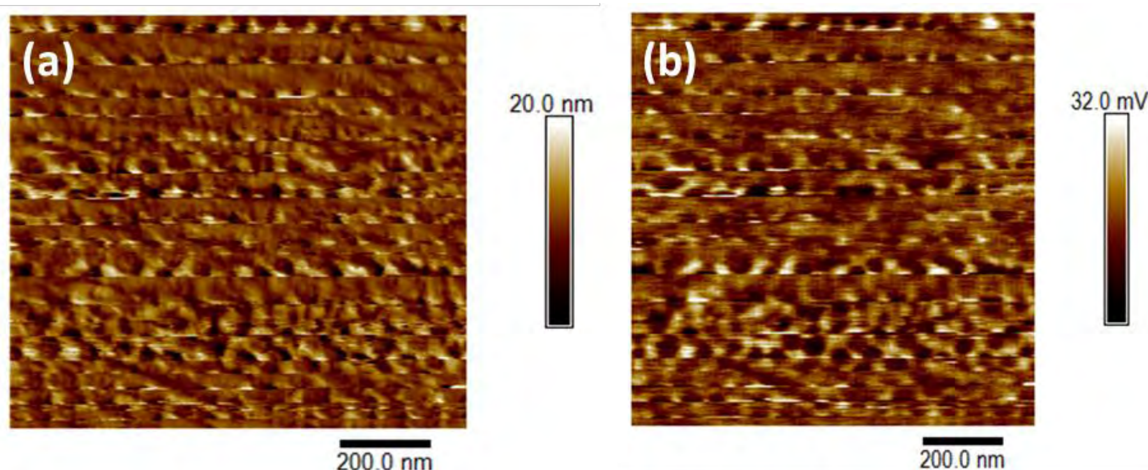

Fig. 43 (a) Topography and (b) thermal image in ambient environment of the BCP template with 5 nm Cr layer.

Thermal conductance measurements and thermal mapping in BCP templates in vacuum environment

SThM measurements were performed in vacuum environment (see details in chapter 2) for the two sets of BCP samples with the same methodology used in ambient environment. Similarly to the measurements in ambient environment, we measured the absolute thermal response of the probe in all the BCP templates, by bringing the probe in and out of contact with the sample surface. In Fig. 44 we plot the normalized probe voltage variations $\left(\frac{dV}{V}\right)$ as a function of the thickness of the Cr layer. A Si bulk sample was used as a reference in our measurements.

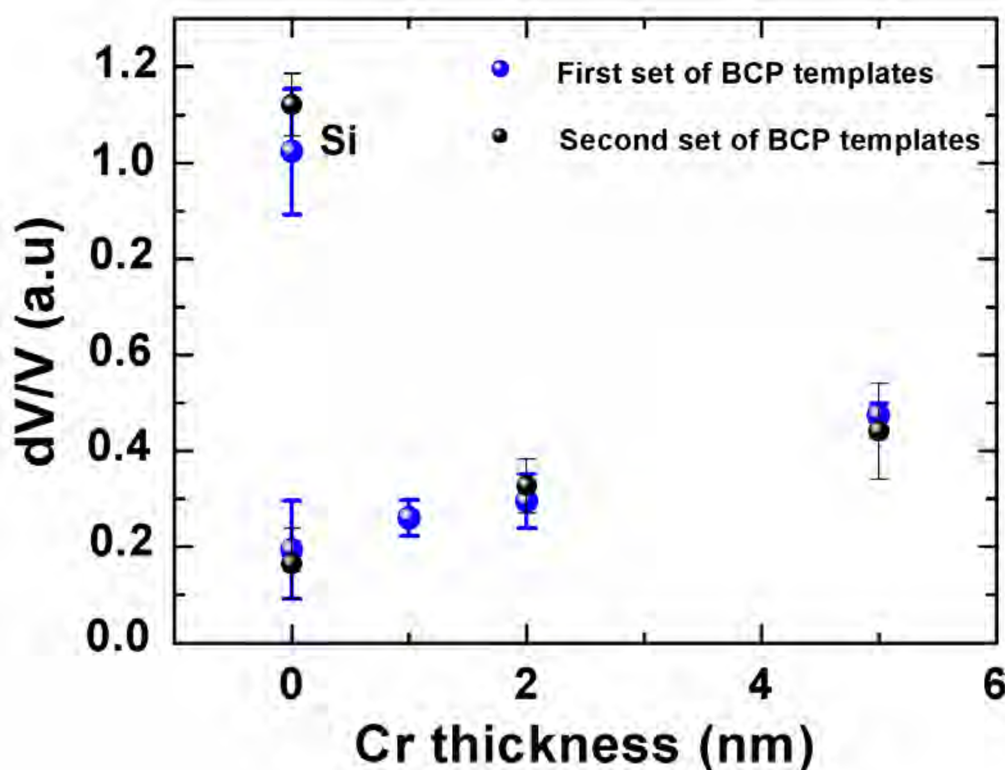

Fig. 44 Normalized probe voltage variations as a function of the thickness of the Cr layer for the BCP templates with the cylindrical domains (blue dots) and the modified BCP templates (blue dots).

Figure 44 shows that by increasing the Cr layer thickness the heat transfer from the tip to the sample and, thus, the thermal conductance increases. This trend is reversed compared to the measurements performed in

ambient air environment, where the effective thermal conductance was decreasing with increasing the Cr layer thickness (see Fig. 42).
To understand the, at first, contradictory results of Fig. 42 and Fig. 44, we shall consider spreading heat variations due to different sizes of heat sources and variations of the Cr layer thickness as the key factor. The parameters that have to be considered are the size of the heat source, and the sizes and thermal conductivities of the sample materials.
The size of the heater is related to the SThM working environment and the geometrical characteristics of the thermal probes. Different heat transfer mechanisms govern the thermal exchange at the tip-sample contact in ambient and vacuum SThM environment as discussed previously. In the measurements in ambient air, the actual heated area of the surface is larger than the tip-sample contact due to the conduction through the air. On the contrary, in vacuum environment the heat transfer through the liquid meniscus and air is eliminated and, neglecting the conductance due to radiation, the dominant heat transfer mechanism is the conduction due to the mechanical contact of the probe with the sample. Considering the small tip apex of the thermal probe ($\sim(5-10)\,nm$) used in vacuum measurements, it is reasonable to assume that the tip-sample thermal exchange is localized at the point contact.
We consider the thermal properties of the BCP layer as homogeneous provided the similar thermal conductivities of the PS and PEO blocks similar intrinsic thermal conductivities ($\sim 0.17\,Wm^{-1}K^{-1}$).[152,153] The system under discussion is outlined in Fig. 45. The low conductive BCP film is placed between two conductive materials, i.e., the Si substrate ($149\,Wm^{-1}K^{-1}$) and the Cr layer ($90\,Wm^{-1}K^{-1}$), therefore, $k_{BCP} << k_{metal} < k_{Si}$.
In the SThM measurements in air environment, the heat source size is much larger compare to the thickness of both metal layer (see Fig. 45a), thus most likely the heat diffusion is not distorted significantly. On the contrary, in the measurements in vacuum, the heat source size ($5-10\,nm$) is comparable to the thickness of the Cr layer (see Fig. 45b). Although the sample is a two layer on a substrate structure and the model of Dryden[122] cannot be applied, a qualitative explanation is still possible. For the measurements in air, although the heat spreading into the sample is affected by the Cr layer, it is more controlled by the Si substrate because of

the large heater size compare to Cr and BCP layers ratio. In this case, heat spreading to the substrate is reduced as the top Cr layer increase, resulting in a lower conductance as seen in Fig. 42. On the contrary, when the reduced size of the heater in-vacuum conditions is commensurate with the thickness of the Cr layer, the influence of the Cr layer dominates over the substrate. Thus, it is the increase of the Cr layer that enhances heat dissipation or conductance within the sample giving the trend seen in Fig. 44. Finally, the increase of conductance in the measurement on the sample with 1 nm Cr layer compared to the measurement on the pristine sample indicates that the heat spreading due to the presence of the metal dominates over the Cr-BCP interface thermal resistance.

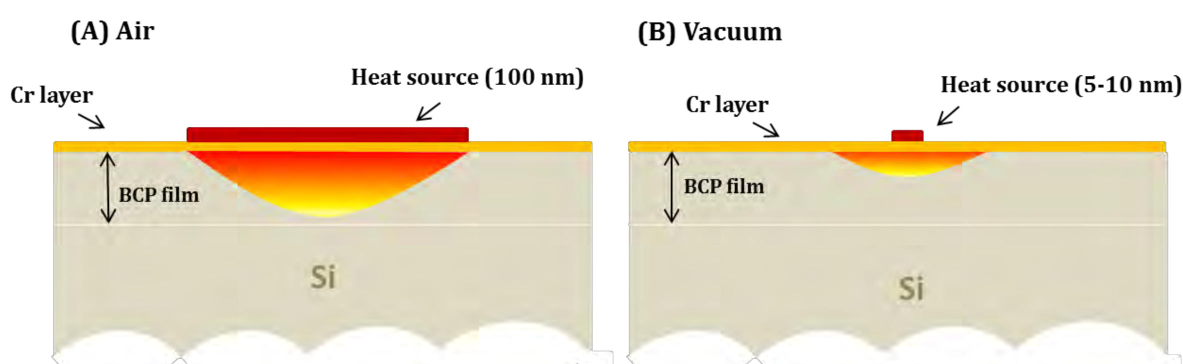

Fig. 45 Schematic illustration of the BCP templates and the different heat source size for measurements performed in (A) air and (B) vacuum conditions.

Our intuitive description gives account of the results of Fig. 42 and Fig. 44, nevertheless, a proper modelling of the heat diffusion between different thermal probe geometries and BCP samples is required to support the described scenario. Nevertheless, a proper modelling of the heat diffusion between different thermal probe geometries and BCP samples is required to support the described scenario.

Next, we present the 2D topography and thermal images of the BCP templates obtained by simultaneous mapping the local variations in height (Fig. 46a,b) and the tip-sample thermal resistance (Fig. 46c,d). The high-resolution thermal images in Fig. 46c,d show thermal contrast between the PS matrix and the PEO cylindrical domains, where the hexagonal arrangement of the latter is clearly visible.

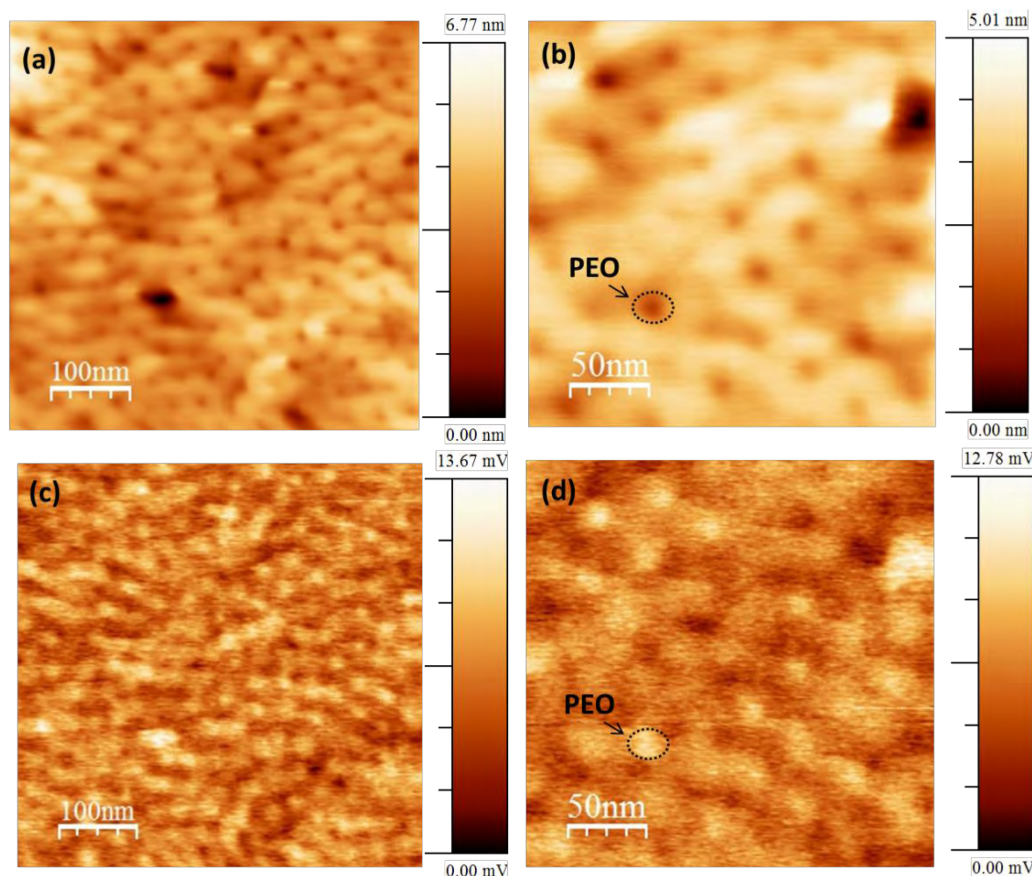

Fig. 46 (a), (b) Topography and (c), (d) thermal images of the BCP template without Cr in high vacuum environment.

The PEO phase of the BCP appears brighter than the PS matrix in the thermal image, indicating that the PS matrix is less thermally conductive than the PEO. Since the two polymers have similar intrinsic thermal conductivities, the origin of the contrast could be related to a topography artifact. The same behaviour appears in the thermal images of BCP templates with Cr layers. Figures 47a-d illustrate 2D topography and thermal images of the BCP template with 5 nm Cr layer, where the PEO cylinders appears more thermally conductive than the PS matrix.

Nevertheless an alternative explanation is possible. Returning to the previous discussion on the results of point measurements, there is a common trait between the cases outlined in Fig. 45 and is that, either dominant or not, heat spreading to the substrate is present and, consequently, affects the tip-sample heat transfer. For a given sample, either the pristine BCP template or a BCP with a Cr layer, if there are no spatial variations of the thermal conductivity and of the Cr layer thickness,

the only parameter that can change the heat spreading to the substrate is the thickness of the BCP. As the samples show a marked surface topography with the PEO cylinders thinner that the PS matrix, this BCP thickness modulation results to a related thermal conductance change and in the contrast in the thermal images.

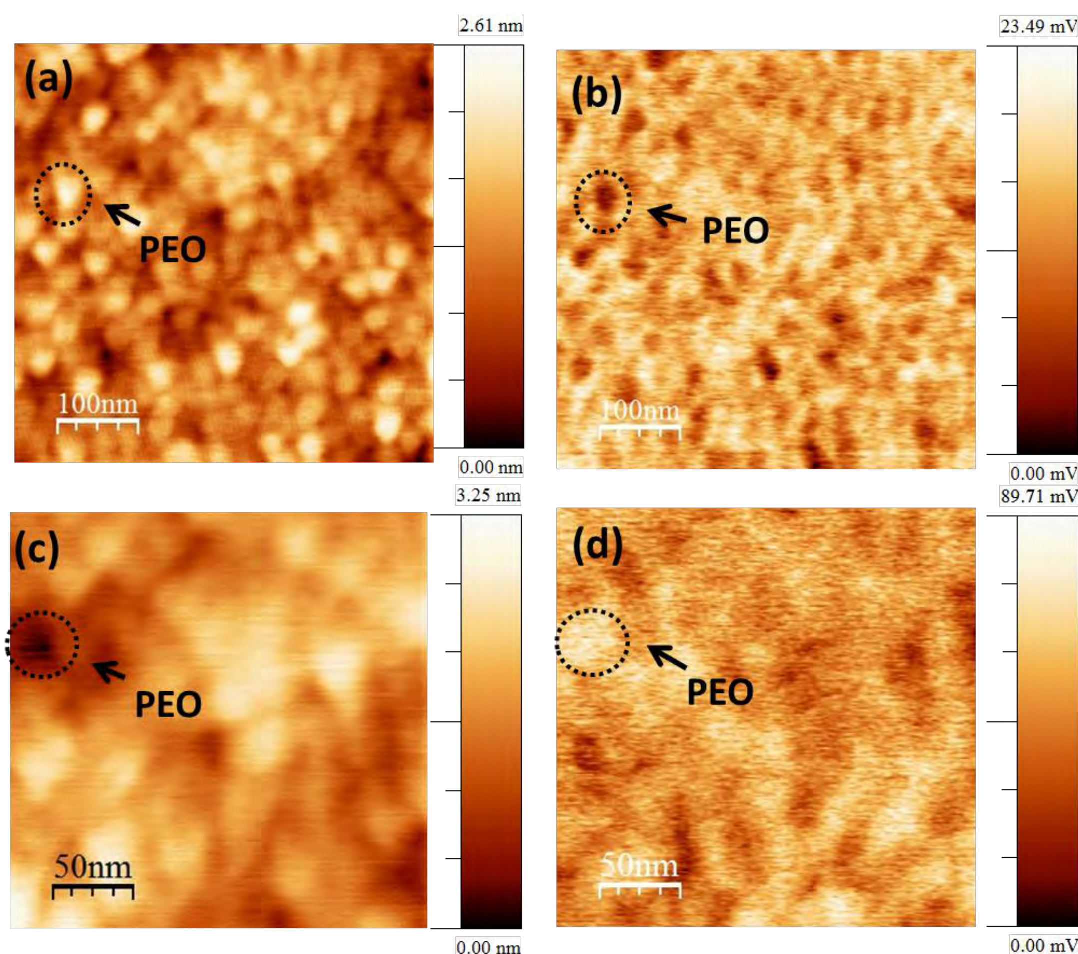

Fig. 47 (a), (c) Topography and (b), (d) thermal images of the BCP template with 5 *nm* Cr layer.

By using the same tip and conditions we performed thermal measurements in the second set of BCP samples. Figure 48 illustrates 2D topography and thermal images of the modified BCP template without Cr layer. Here, we assume that the PEO cylinders rearranged their position in-plane to the PS matrix after the chemical treatment. Therefore the PS matrix now is closer to the Si substrate (black in the topography images) and appears more thermally conductive (bright in the thermal images) than the PEO domains.

This trend is the opposite than before (see Fig. 46, 47), i.e., the PEO phase appeared to be more conductive.

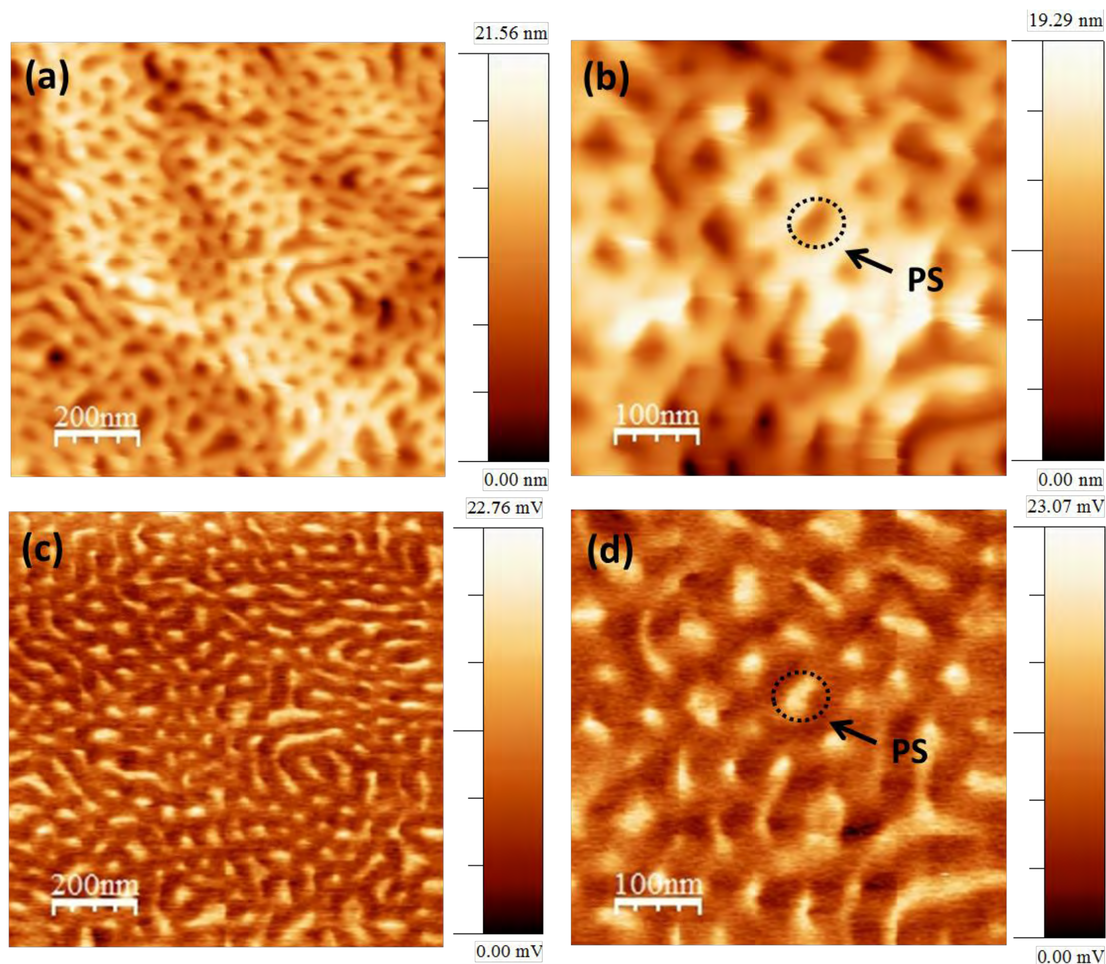

Fig. 48 (a),(b) Topography and (c), (d) thermal images of the modified BCP template in high vacuum environment.

Consequently, seems that the polymer, which is closer to the Si substrate, appears to be more conductive in the thermal images. The same trend has been observed in the BCP templates with 2 and 5 *nm* thick Cr layers as is shown in the thermal images in Fig. 49c,d. In addition, Fig. 49a and Fig. 49b show topography images of the BCP templates with 2 and 5 *nm* Cr layers, where crystallized structures have been observed. The PS-PEO-PS monolayers crystallized during the formation of the BCP due to a rise in the surface pressure, which then resulted in non-uniform growth of the BCP (compression of PS-PEO monolayers). This is a common issue in self-assembled processes as has been reported elsewhere.[154] The incorporation

of the PS component with a higher glass transition temperature (T_g) than the PEO phase, modifies the crystallization behaviour of the film.

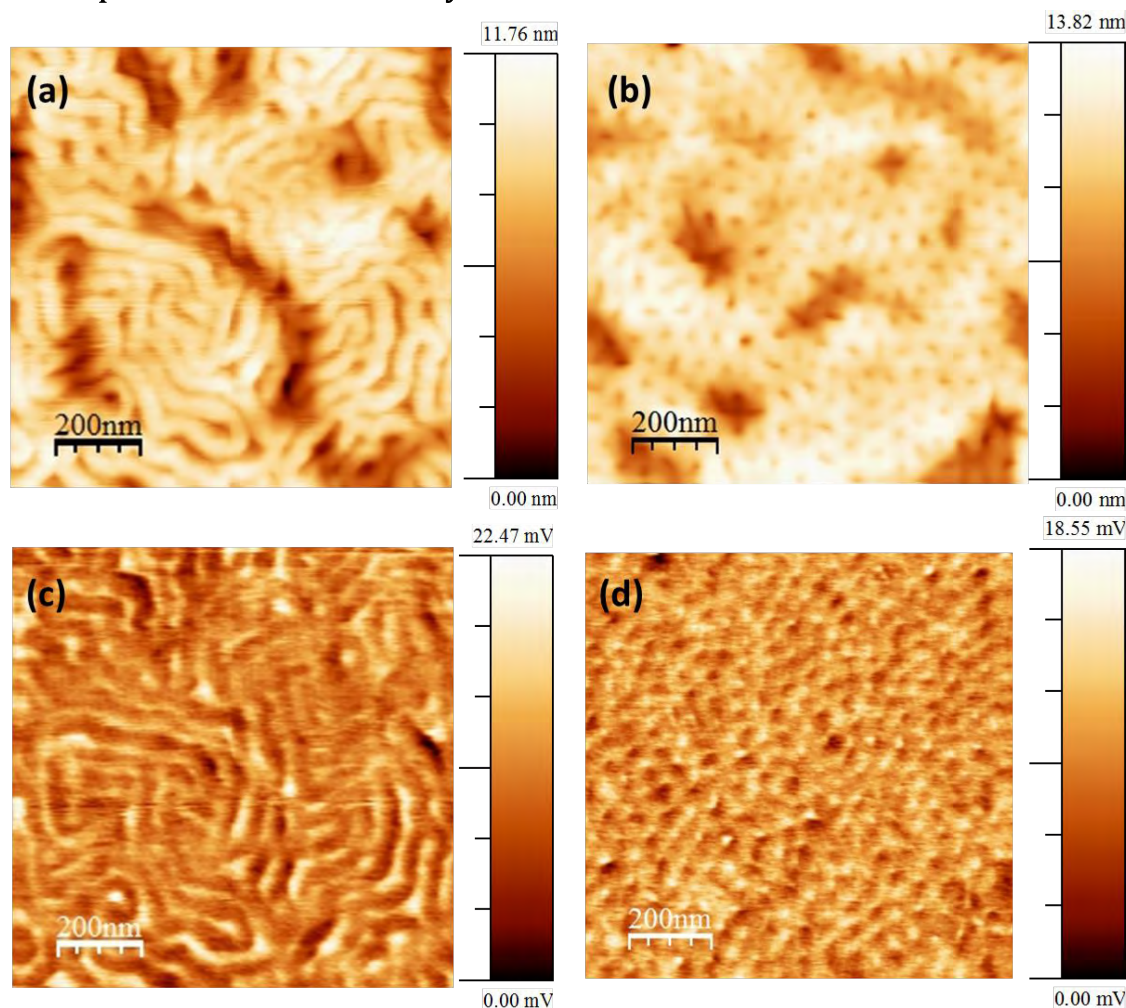

Fig. 49 Topography and thermal images of the modified BCP templates with (a), (c) 2 and (b), (d) 5 nm Cr layers, respectively.

Next we determine the thermal spatial resolution in our measurements by analyzing topography and thermal signal profiles along the dashed lines in Fig. 50a and Fig. 50b, respectively. The images are constituted of 256 × 256 points. By monitoring the thermal line scan depicted in Fig. 50d we can see that as the tip is moving from the higher level (PEO) towards the edge of the PS phase, the probe voltage increases. This 13 mV increase of the probe voltage on top of the PS matrix indicates an increase of the heat conduction from the probe to the sample, i.e., a decrease of the probe-sample thermal resistance. However, topographic artifacts have to be carefully distinguished from true variations in the voltage signal that are not related to the geometrical change in tip-sample contact area. Comparing the 20 nm

flat area in the topography line scan in Fig. 50c (square red box) and the corresponding thermal signal in Fig. 50d, we can approximately estimate that the thermal spatial resolution is in the sub-20 *nm* range. In this region there is not cross talk between topography and thermal signals, indicating that the contact between the tip and the sample does not change significantly and the acquired signal is not related with topography-induced artifacts.

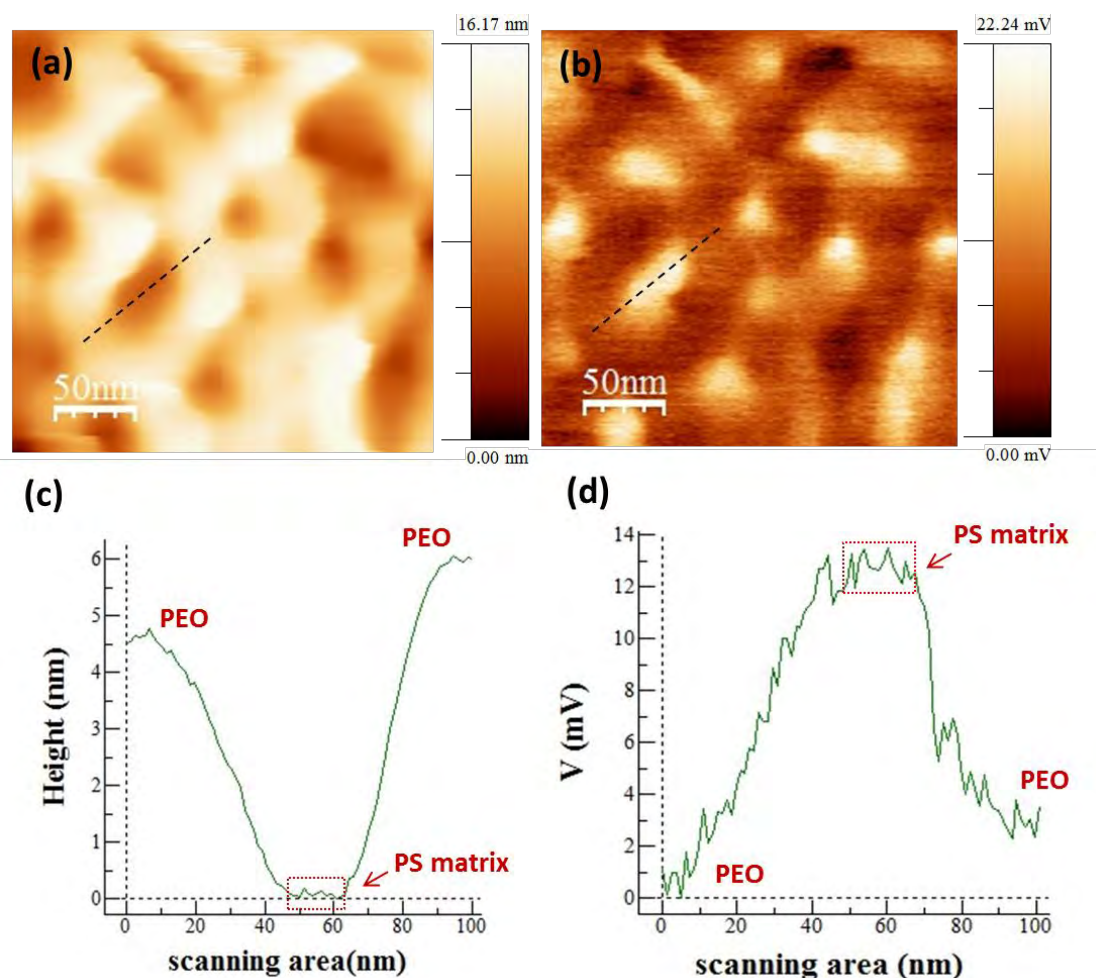

Fig. 50 High resolution (a) topography and (b) thermal images of the modified BCP template in high vacuum environment. (c) Topography and (d) voltage signal profiles along the dashed lines in Fig. 50a and Fig. 50b, respectively.

In summary, the fabrication of bare and Cr covered micro-phase separated block copolymer templates has been investigated. TEM-EDX and ELLS measurements were performed to confirm the separation of the two block

copolymer phases (PEO, PS) and the existence of Cr. The SThM results revealed that thermal transport depends on sample properties, the size of the heat source and the experimental conditions. Thermal measurements in ambient environment and with large probe geometries showed that the heat spreading to Si controls the thermal transport. On the other hand SThM measurements in high vacuum environment and with smaller probes indicated the increased impact of the heat spreading into the metal and reduced Si substrate effect. SThM measurements in high vacuum environment on bare and metal covered BCP samples allow the thermal imaging of the two segregated phases (PEO-PS) of the BCPs with sub-20 nm thermal spatial resolution. The contrast in the thermal images seems to be related to the modulation of the BCP layer thickness. However, additional experiments and modelling are necessary for the determination of the thermal conductivity of the BCP films.

6

Conclusions and perspectives

In this thesis we report on the studies of thermal transport in suspended materials, specifically crystalline Si membranes and periodic porous crystalline Si membranes. We followed two different strategies to suppress the thermal conductivity and tune the temperature dependence of the thermal conductivity at high temperatures. From the experimental results obtained with 2LRT we found that there is a characteristic size in each material system, which characterizes the surface phonon scattering, thus thermal transport. For the unpatterned membranes this size is given by their thickness (t), whereas for the periodic porous Si membranes is given by the neck size (n).The characteristic sizes t and n are the limiting dimensions, which set a cut-off frequency for the propagation of phonons due to diffusive boundary scattering, i.e., phonons with $\Lambda > t, n$ will not fully propagate, thus, reducing their contribution to thermal conductivity.

We demonstrated that for a given membrane thickness ($250\,nm$ in the reported studies), the thermal conductivity can be reduced to values close to a-Si by drilling holes in a periodic pattern (periodic porous membranes), i.e., increasing the surface to volume ratio. Moreover, it has been seen that the temperature evolution, $k(T)$, from room temperature to about $1000\,K$ can be effectively tuned and approaching to a regime where the thermal conductivity is almost insensitive to T. Such reduction can only be achieved for thicknesses down to $10\,nm$ in unpatterned membranes, which can compromise the electronic properties and the mechanical stability of a hypothetical thermoelectric device. Furthermore, the contribution of convective heat transfer has been studied and found to compete with heat conduction, which can be detrimental in the performance of thermoelectric

modules operating at atmospheric pressure. However, this clear disadvantage might be favourable in the cases where fast and efficient cooling is required like in, e.g., Si-based electronics, mechanical resonators, photonics and optomechanics.

Next, we studied the thermal transport in supported materials and smaller length scales with scanning thermal microscope probes both in ambient and vacuum environment. To this aim, we studied thermal transport in self-assembled in-plane epitaxial $Si_{1-x}Ge_x$ alloy NWs provided in addition combined structural and chemical composition analysis of the investigated NWs. We presented new insights regarding the morphology of the in-plane nanostructures, their size-dependent gradient chemical composition and we determined their thermal conductivity with values in the range of $2-3\ Wm^{-1}K^{-1}$. These results can provide valuable information to evaluate the growth processes and essential guidance for the integration of epitaxial in-plane nanowires in devices with varying composition in a controllable way and with improved heat management.

Last, we studied the fabrication, the structure morphology, and the thermal behaviour of bare and chromium covered block copolymers containing PS and PEO compartments in thin films on Si wafers. TEM-EDX analysis allowed us to understand how metal nanoparticles integrated in BCP domains. In addition, SThM provided the thermal imaging of the two segregated phases (PEO-PS) of sub-50 nm characteristic sizes with sub-20 nm thermal spatial resolution. SThM measurements in vacuum and ambient environment revealed that the nanometre metal coated layers strongly influence the heat dissipation in the volume of the BCP domains. The comparison of the SThM results obtained in ambient and vacuum conditions and with different probe geometries showed the importance to apply an appropriate thermal model depending on environment and thermal probe characteristics. Further analysis and simulations are required for a quantitative analysis of the results in order to obtain the thermal conductivity of the BCP films. However, these results show the great potential of the self-assembly method for the fabrication of nanostructures with sub-50 nm characteristic sizes and the applicability of the SThM technique for nanoscale thermal studies in complex nanostructures.

Numerous opportunities may arise based on the experimental techniques and results obtained in this thesis. The capability to perform thermal measurements in nanostructures with high thermal and spatial resolution encourages the investigation of heat transport in different material systems with high technological relevancy, such as interfaces and two dimensional materials. In parallel, by using well studied nanomaterials as model systems fundamental aspect of thermal transport such as the transition from the ballistic to the diffusive thermal transport regime and the spectral distribution of the phonon mean free path, can be further explored. The comparison between the obtained experimental data and present phonon transport theories, for example based on molecular dynamic simulations and calculations using the full Boltzmann equation, could provide new insights to establish a consistent theory of thermal transport on nanoscopic length scales.

Another interesting direction could be to implement the studied instrumentations and methods to investigate non-equilibrium thermal processes with nanoscopic spatial resolution. In these processes the temperature may depend on the time scale of the measurement and the sensitivity of the thermometers. This is a challenging goal considering that the study of dynamic effects in systems out of equilibrium requires high temporal resolution ($\sim ps$). Although experimental techniques nowadays, such as time domain thermoreflectance, fulfil this requirement, the thermal spatial resolution is limited in the micrometre scale. On the other hand SThM at the moment provides very low temporal resolution which makes the study of non-equilibrium effects almost impossible. The capability to study thermal dynamic effects with submicron thermal spatial resolution might be a way to better understand the basic principles govern heat propagation and scattering on nanoscopic length scales.

Bibliography

1. David G. Cahill, Paul V. Braun, G.Chen, D. R. Clarke, S. Fan, K. E. Goodson, P. Keblinski, W. P. King, G.D. Mahan, A. Majumdar, H. J. Maris, Si. R. Phillpot, E. Pop, and L.Shi, *Appl. Phys. Rev* 2014, **1**, 011305.
2. Olga Caballero-Caleroa, and Roberto D'Agosta *ECS J. Solid State Sci.,* 2017, **6**, 3065-3079.
3. L. Shia, C. Dames, J. R. Lukes, P. Reddy, J. Duda, D.G. Cahill, J. Lee, A. Marconnet, K. E. Goodson, J. H Bahk, A.Shakouri, R. S. Prasherk, J.Felts, W. P. King, B. Han and J. C. Bischof, NANOSC. MICROSC. THERM. 2015, **19**, 127-165.
4. D. G. Cahill, W. K. Ford, K. E. Goodson, G. D. Mahan, A. Majumdar, H. J. Maris, R. Merlin, S. R. Phillpot, *J. Appl. Phys.,* 2003, **93**, 2.
5. D. G. Cahill, K. Goodson, A. Majumdar, *J. Heat Transfer,* 2002, **124**, 237.
6. H. M. Pollock and A. Hammiche, *J. Phys. D: Appl. Phys.* 2001, **34**, 23-53.
7. A. M. Marconnet M. Asheghi, K. E. Goodson, *J. Heat Transfer,* 2013, **135**, 061601-1.
8. L. Shi, C. Yu, and J. Zhou, *J. Phys. Chem. B* 2005**, 109***,* 22102-22111.
9. R. P. Prasankumar, A. J. Taylor, in *Optical Techniques for Solid-State Materials Characterization,* by CRC Press, July, 2011.
10. L. Lu, W. Yi and D. L. Zhang, *Rev. Sci. Instrum.* 2001, **72**, 2996.
11. Y. Singh, *Int. J. Mod. Phys. Conf. Ser.* 2013, **22**, 745–756
12. B. Stoib, S. Filser, J. Stotzel, A. Greppmair, N. Petermann, H. Wiggers, G. Schierning, M. Stutzmann, and M. S. Brandt, *Semicond. Sci. Technol.* 2014, **29**,124005.
13. R. S. Das, Y. K. Agrawal, 2011, **57,**163-176**.**
14. R. Tsu and J. G. Hernandez, *Appl. Phys. Lett.* 1982, **41**, 1016.
15. S. Perichon, V. Lysenko, B. Remaki, D. Barbier, and B. Champagnon, *J. Appl. Phys.* 1999, **86**, 4700.
16. S. Perichon, V. Lysenko, P. Roussel, B. Remaki, B. Champagnon, D. Barbier, P. Pinard, *Sens. Actuators A* 2000, **85**, 335.
17. X. Liu, X. Wu, T. Ren, *Appl. Phys. Lett.* 2011, **98**, 174104.

18. S. Huang, X. Ruan,J. Zou, X. Fu, and H. Yang, *Microsyst. Technol.* 2009, **15**, 837.
19. A. Balandin, S. Ghosh, W. Bao, I. Calizo, D. Teweldebrhan,F. Miao, C. N. Lau, *Nano Lett.* 2008, **8**, 902.
20. W. Cai, A. L. Moore, Y. Zhu, X. Li, S. Chen L. Shi and R. S. Ruoff, *Nano Lett.* 2010, **10**, 1645
21. J.-U. Lee, D. Yoon, H. Kim, S. W. Lee, and H. Cheong, *Phys. Rev.* 2011, **83**, 081419.
22. M. Soini, I. Zardo, E. Uccelli, S. Funk, G. Koblmuller, A. Fontcuberta i Morral, and G. Abstreiter, *Appl. Phys. Lett.* 2010, **97**, 263107.
23. J. Liu, H. Wang, W. Ma, X. Zhang, and Y. Song, *Rev. Sci. Instr.* 2013, **84**, 044901.
24. B. Stoib, S. Filser, N. Petermann, H. Wiggers, M. Stutzmann, and M. S. Brandt, *Appl. Phys.* Lett. 2014, **104**, 161907.
25. J. S. Reparaz, E. Chavez-Angel, M. R. Wagner, B. Graczykowski, J. Gomis-Bresco, F. Alzina, and C. M. Sotomayor Torres, *Rev. Sci. Instrum.* 2014, **85**, 034901.
26. Y. Kuk and P. J. Silverman, *Rev. Sci. Instrum.* 1989, **60**, 165-181.
27. G. S. Hsiao, R. M. Penner, and J. Kingsley, *Appl. Phys. Lett.* 1994, **64**, 1350.
28. G. Binnig and C. F. Quate, *Phys. Rev. Lett.* 1986, **56**, 9.
29. R. J. Pylkki, P. J Moyer, P. E West, *Jpn. J. Appl. Phys.* 1994, **33**, 3785?90.
30. E. Oesterschulze, M. Stopka, L. Ackermann, W. Scholz, S. Werner, *J. Vac. Sci. Technol. B*, 1996, **14**, 832
31. L. Shi, S. Plyasunov, A. Bachtold, P. McEuen, A. Majumdar, *Appl. Phys. Lett.* 2000, **77**, 4295-7.
32. F. Menges, H. Riel, A. Stemmer, and B. Gotsmann, *Nano Lett.* 2012, **12**, 596–601.
33. F. Ruiz, W. D. Sun, F. H. Pollak and C. Venkatraman, *Appl. Phys. Lett*. 1998, **73**, 1802.
34. F. Menges, P. Mensch, H. Schmid, H. Riel, A. Stemmer and & B. Gotsmann, *Nature Com.*, 2016, **7**, 10874.
35. D. Florescu, V. Asnin, F. Pollak, A. Jones, J. Ramer, M. Schurman, I. Ferguson, *Appl. Phys. Lett.* 2000, **77**, 1464-6.
36. M. E. Pumarol, M. C. Rosamond, P. Tovee, M. C. Petty, D. A. Zeze, V. Falko, O.V. Kolosov, *Nano Lett.* 2012, **12**, 2906-2911.

37. F. Menges, H. Riel, A. Stemmer, C. Dimitrakopoulos, and B. Gotsmann, *Phys. Rev. Lett.* 2013, **111**, 205901.
38. S. Lefèvre, S. Volz, J. B. Saulnier, C. Fuentes, N. Trannoy, *Rev. Sci. Instrum.* 2003, **74**, 2418.
39. S. Gomès, L. David, V. Lysenko, A. Descamps, T. Nychyporuk, M. Raynaud, *J. Phys. D: Appl. Phys.* 2007, **40**, 6677-6683
40. H. M. Pollock, A. Hammiche, *J. Phys. D: Appl. Phys.* 2001, **34**, 23–53.
41. S. Gomès, A. Assy, P. O. Chapuis, *Phys. Status Solidi A* 2015, **212**, 3.
42. L. Shi and A. Majumdar, *J. Heat Transfer* 2002, **124**, 329.
43. A. Altes, K. Mutamba, R. Heiderhoff, H. L. Hartnagel, and L. J. Balk, *Superlattices Microstruct.* 2004, **35**, 465.
44. P. Janus, D. Szmigiel, M. Weisheit, G. Wielgoszewski, Y. Ritz, P. Grabiec, M. Hecker, T. Gotszalk, P. Sulecki, and E. Zschech, *Microelectron. Eng.* 2010, **87**, 1370.
45. S. Gomes, H. Trannoy, P. Grossel, F. Depasse, C. Bainier, and D. Charraut, *Int. J. Therm. Sci.* 2001, **40**, 949.
46. S. Lefèvre and S. Volz, *Rev. Sci. Instrum.* 2005, **76**, 033701.
47. J. Bodzenta, J. Juszczyk, and M. Chirtoc, *Rev. Sci. Instrum.* 2013, **84**, 093702.
48. A. Bontempi, T. P. Nguyen, R. Salut, L. Thiery, D. Teyssieux and P. Vairac, *Rev. Sci. Instrum.* 2016, **87**, 063702.
49. T. P Nguyen, L. Thiery, D. Teyssieux, D. Briand and P. Vairac, *Conf. Series: Journal of Physics: Conf. Series*, 2017, **785**, 012005.
50. K. Kim, J. Chung, G. Hwang, O. Kwon, and J. Sik Lee, *ACS Nano*, 2011, 5 8700–8709.
51. A. Hammiche, H. M Pollock, M. Songyand D. J Hourston, *Meas. Sci. Technol*., 1996, **7**, 142–150.
52. A. Majumdar, *Annu. Rev. Mater. Sci.,* 1999, **29**, 505–58.
53. A. Assy, S. Lefèvre, P. O. Chapuis and S. Gomès*, J. Phys. D: Appl. Phys.* 2014, **47**, 442001.
54. B. Cretin, S. Gomès, N. Trannoy, and P. Vairac, in Microscale and Nanoscale Heat Transfer, 2007,181–238, Springer Berlin, edited by S. Volz.
55. S. Kwon, M. Wingert, J. Zheng, J. Xiang, and R. Chen, *Nanoscale* 2016, **8**, 13155-13167.
56. M. Asheghi, Y. K. Leung, S. S. Wong, and K. E. Goodson, *Appl. Phys. Lett.* 1997, **71**, 1798.

57. E. Chavez-Angel, J. S. Reparaz, J. Gomis-Bresco, M. Wagner, J. Cuffe, B. Graczykowski, A. Shchepetov, H. Jiang, M. Prunnila, J. Ahopelto, et al., *APL Mater.* 2014, **2**, 012113.
58. J. Cuffe, J. K. Eliason, A. A. Maznev, K. C. Collins, J. A. Johnson, A. Shchepetov, M. Prunnila, J. Ahopelto, C. M. Sotomayor Torres, G. Chen, and K. A. Nelson, *Phys. Rev. B* 2015, **91**, 245423.
59. M. Asheghi, M. N. Touzelbaev, K. E. Goodson, Y. K. Leung and S. S. Wong, *J. Heat Transfer* 1998, **120**, 30-36.
60. W.Liu and M. Asheghi, *J. Appl. Phys.* 2005, **98**, 123523.
61. B. Graczykowski, M. Sledzinska, F. Alzina, J. Gomis, Bresco, J. Reparaz, M. Wagner, and C. M. Sotomayor Torres, *Phys. Rev. B* 2015, **91**, 075414.
62. A. Jain, Y.-J. Yu, and A. J. H. McGaughey, *Phys. Rev. B*, 2013, **87**, 195301.
63. M. Maldovan, *Nature*, 2013, **503**, 209.
64. R. Anufriev, J. Maire, and M. Nomura, *Phys. Rev. B* 2016, **93**, 593, 045411.
65. N. Zen, T. A. Puurtinen, T. J. Isotalo, S. Chaudhuri, and I. J. Maasilta, *Nat. Commun.* 2014**, 5,** 3435**.**
66. S. Alaie, D. F. Goettler, M. Su, Z. C. Leseman, C. M. Reinke, and I. El-Kady, *Nat. Commun.* 2015, **6**, 7228.
67. J.-K. Yu, S. Mitrovic, D. Tham, J. Varghese, and J. R. Heath, *Nat. Nanotechnol.* 2010, **5**, 718-721.
68. J. Lim, H.-T. Wang, J. Tang, S. C. Andrews, H. So, J. Lee, D. H. Lee, T. P. Russell, and P. Yang, 2015, *ACS nano* , 2016, **10**, 124–132.
69. C. J. Glassbrenner and G. A. Slack, *Phys. Rev.* 1964, **134**, 619.
70. S. Neogi, J. S. Reparaz, L. Felipe C. Pereira, B. Graczykowski, M. R. Wagner, M. Sledzinska, A. Shchepetov, M. Prunnila, J. Ahopelto, C. M. Sotomayor-Torres, and D. Donadio, *ACS Nano* 2015, **9**, 3820.
71. R. Anufriev, A. Ramiere, J. Maire and M. Nomura, *Nature Com.* 2017, **8**, 15505.
72. X. Wang and B. Huang, *Sci. Rep.* 2014, **4**, 6399.
73. M. Sledzinska, B. Graczykowski, F. Alzina, J. S. Lopez, C. M. Sotomayor *Microelectron. Eng*. 2016, **149**, 41-45.
74. Y. Ju and K. Goodson, *Appl. Phys. Lett.* 1999, **74**, 3005.
75. A. Eucken, VDI-Forschungsheft, 1932, **16**, 353.
76. Z. Hashin and S. Shtrikman, *J. Appl. Phys.* 1962, **33**, 3125.
77. K. Esfarjani, G. Chen, and H. T. Stokes, *Phys. Rev. B* 2011, **84**, 085204.
78. K. T. Regner, D. P. Sellan, Z. Su, C. H. Amon, A. J. McGaughey, and J. A. Malen, *Nat. Commun.* 2013, **4**, 635 1640.

79. M. Maldovan, *Nat. Mater.* 2015*,* **14**, 667.
80. K. Uchinokura, T. Sekine, and E. Matsuura*, J. Phys. Chem. Solids* 1974, **35**, 171.
81. P. A. Temple and C. E. Hathaway, *Phys. Rev. B* 1973, **7**, 3685643.
82. W. P. Acker, B. Yip, D. H. Leach, and R. K. Chang, *J. Appl. Phys.* 1988, **64**, 2263.
83. M. R. Wagner, B. Graczykowski, J. S. Reparaz, A. El Sachat, M. Sledzinska, F. Alzina, and C. M. Sotomayor Torres, *Nano Lett.* 2016, **16** (9), 5661–5668.
84. K. Kadoya, N. Matsunaga, and A. Nagashima, *Journal of J. Phys. Chem. Ref.* Data 1985, **14**, 947.
85. S. Chen, A. L. Moore, W. Cai, J. W. Suk, J. An, C. Mishra, C. Amos, C. W. Magnuson, J. Kang, L. Shi, and R. S. Ruo, *ACS Nano* 2011, **5**, 321.
86. S. Sokolov, J. Lian, E. Yuce, S. Combrie, G. Lehoucq, A. De Rossi, and A. P. Mosk, *Appl. Phys. Lett.* 2015, **106**, 171113.
87. C. Cheng, W. Fan, J. Cao, S.-G. Ryu, J. Ji, C. P. Grigoropoulos, and J. Wu, *ACS nano* 2011, **5**, 10102.
88. D. Paul, *Adv. Mater.* 1999, **11**, 3.
89. M. Amato, M. Palummo, R. Rurali, and S. Ossicini, 2014, *Chem. Rev.* **114**, 1371−1412.
90. J. C. Bean, *Science* 1985, **230**, 4722.
91. G. Eneman, P. Verheyen, R. Rooyackers, F. Nouri, R. Schreutelkamp, V. Moroz, L. Smith, M. Jurczak, and K. De Meyer, *IEEE Trans. Electron Devices* 2006, **53**, 7.
92. C.-C. Shih, W. Y. Lee and W. C. Chen, *Mater. Horiz.* 2016, **3**, 294.
93. A. Irrera, P. Artoni, V. Fioravanti, G. Franzò, B. Fazio, P. Musumeci, S. Boninelli, G. Impellizzeri, A. Terrasi, F. Priolo and F. Iacona, *Nanoscale Res. Lett.* 2014, **9**, 74.
94. W. Lu, P. Xie, and C. M. Lieber, *IEEE Trans. Electron Devices* 2008, **55**, 2859–2876.
95. D. Saccheto, M. Ben-Jamaa, G. De Micheli and Yusuf Leblebici, presented in part at the 39th European Solid-State Device Research Conference, 2009.
96. M. Schvartzman, D. Tsivion, D. Mahalu, O. Raslin, and E. Joselevich, *PNAS* 2013, **110**, 38.
97. G. Lebon, H. Machrafi, *Physica E* 2015, **71**, 117–122.
98. D. Li, Y. Wu, R. Fan, P. Yang, A. Majumdar, *Appl. Phys. Lett.*, 2003, **83**, 15.
99. M. C. Wingert, Z. C. Y. Chen, E. Dechaumphai, J. Moon, Ji-Hun Kim, J. Xiang and R. Chen, *Nano Lett.* 2011, **11**, 5507-5513.

100. S. Kwon, M. C. Wingert, J. Zheng, J. Xiang, and R. Chena, *Nanoscale* 2016, **8**, 13155.

101. H. Kim, l. Kim, H. J. Choi, and W. Kim, *Appl. Phys. Lett.*, 2010, **96**, 233106-10190.

102. Z. Wang and N. Mingo, *Appl. Phys. Lett.* 2010, **97**, 101903.

103. L. Shi, Deyu Li, C. Yu, W. Jang, D. Kim, Z. Yao, P. Kim, A. Majumdar, *J. Heat transfer* 2003, **125**, 881.

104. J. Chen, G. Zhang, and B. Li, *Appl. Phys. Lett.* 2009, **95**, 073117.

105. E. K. Lee, L. Yin, Y. Lee, J. Woon Lee, S. Jin Lee, J. Lee, S. Nam Cha, D. Whang, G. S. Hwang, K. Hippalgaonkar, A. Majumdar, C. Yu, Byoung L. Choi, J. Min Kim, and K. Kim, *Nano Lett.* 2012, **12**, 2918–2923.

106. L. Yin, , E. Kyung Lee, , J. Woon Lee, D. Whang, B. Lyong Choi, and Choongho Yu, 2012, *Appl. Phys. Lett.* **101**, 043114.

107. T. K. Hsiao, H. K Chang, S. C Liou, M. W. Chu, S. C. Lee and C. W. Chang, *Nat. Nanotechnol.* 2013, **8,** 534-538.

108. S. Grauby, E. Puyoo, J. M. Rampnoux, E. Rouvière, and S. Dilhaire, *J. Phys. Chem. C* 2013, **117**, 9025−9034.

109. A. I. Persson, Y. K. Koh, D. G. Cahill, L. Samuelson, H. Linke, *Nano Lett.* 2009, **9,** 4484.

110. M. I. Alonso, E. Bailo, M. Garriga, A. Molero, P. O. Vaccaro, A. R. Goñi, A. Ruiz, and M. Alonso, *J. Phys. Chem. C* 2015, **119**(38), 22154–22163.

111. A. Tiberj and J. Camassel, in *Raman Imaging Techniques and Applications*, ed. A. Zoubir, Springer series in Optical Sciences 168, Berlin Heidelberg, 2012, **2**, 386.

112. A. Picco, E. Bonera, F. Pezzoli, E. Grilli, O .G. Schmidt, F. Isa, S. Cecchi and M. Guzzi, *Nanoscale Res. Lett.* 2012, **7**, 633.

113. P. Meduri, G. U. Sumanasekera, Z. Chen, and M. K. Sunkara, *J. Nanosci. Nanotechno.*, 2008, **8***,* 3153–3157.

114. M. Bezuidenhout, T. Kennedy, S. Belochapkine, Y. Guo, E. Mullane,P. A. Kiely and K. M. Ryan, *J. Mater. Chem. C* 2015, **3**, 7455—7462.

115. H-K Chang and Si-C. Lee, *Nanoscale Res. Lett.* 2012, **7**, 155.

116. M. I. Alonso, A. Ruiz, M. Alonso, E. Bailo, M. Garriga, A. Molero, P.O. Vaccaro, A. R. Goñi, in Mater. Today: Proceedings, 2015, **2**, 548-556.

117. P. D. Kanungo, A. Wolfsteller, N.D. Zakharov, P. Werner, U. Gosele, *Microelectron. J.* 2009, **40**, 452– 455.

118. P. O. Chapuis, J. J. Greffet, K. Joulain and S. Volz, *Nanotechnology*, 2006, **17**, 2978–2981.

119. B. Gotsmann, M. A. Lantz, A. Knoll, U. Dürig, in *Nanotechnology vol. 6: Nanoprobes*, Wiley-VCH, Weinheim ed. H. Fuchs, 2010.
120. P. Tovee, M. Pumarol, D. Zeze, Kevin Kjoller, and O. Kolosov, *J. Appl. Phys.,* 2012, **112**, 114317.
121. M. M. Yovanovich, J. R. Culham, and P. Teertstra, *IEEE Trans. Compon. Packag. Manuf. Technol.* 1998, **21**, 1070–9886.
122. J. R. Dryden, *ASME J. Heat Transf.,* 1993, **105**, 408–410.
123. G. Pernot, M. Stoffel, I. Savic, F. Pezzoli, P. Chen, G. Savelli, A. Jacquot, J. Schumann, U. Denker, I. Mönch, Ch. Deneke, O. G. Schmidt, J. M. Rampnoux, S. Wang, M. Plissonnier, A. Rastelli, S. Dilhaire and N. Mingo, *Nat. Materials* 2010, **9**, 491–495.
124. S. K. Estreicher, T. M. Gibbons, By. Kang, and M. B. Bebek, *J. Appl. Phys.* 2014, **115**, 012012.
125. Y. Pan, G. Hong, S. N. Raja, S. Zimmermann, M. K. Tiwari, and D. Poulikakos, *Appl. Phys. Lett.* 2015, **106**, 093102.
126. N. Uchida, T. Maeda, R. R. Lieten, S. Okajima, Y. Ohishi, R. Takase, M.Ishimaru, and J. P Locquet, *Appl. Phys. Lett.* 2015, **107**, 232105.
127. P. Chen, N. A. Katcho, J. P. Feser, W. Li, M. Glaser, O. G. Schmidt, D. G. Cahill, N. Mingo, and A. Rastelli, *Phys. Rev. Lett.*, 2013, **111**, 115901.
128. Y. S. Muzychka, M. R. Sridhar, M. M. Yovanovich, V. W. Antonetti, *J. Thermophys. Heat. tr.* 1999 **13**, 489-494.
129. S. M. Lee, D. G. Cahill, and R. Venkatasubramanian, *Appl. Phys. Lett.,* 1997, **70**, 2957–2959.
130. M. L. Lee and R. Venkatasubramanian, *Appl. Phys. Lett.,* 2008, **92**, 053112.
131. A. Iskandar, A. Abou-Khalil, M. Kazan, W. Kassem, and S. Volz, *J. Appl. Phys.*, 2015, **117**, 125102.
132. R. Cheaito, J. C. Duda, T. E. Beechem, K. Hattar, J. F. Ihlefeld, D. L. Medlin, M. A. Rodriguez, M. J. Campion, E. S. Piekos, and P. E. Hopkins, 2012, *Phys. Rev. Lett.*, 2012, **109**, 195901.
133. G. Xie, Y. Guo, X. Wei, K. Zhang, L. Sun, J. Zhong, G. Zhang, and Y.W. Zhang, 2014, *Appl. Phys. Lett.*, **104**, 233901.
134. J. A. P. Taborda, M. M. Rojo J. Maiz, N. Neophytou and M. Martin-Gonzalez, *Sci. Rep.*, 2016, **6**, 32778.
135. S. M. Lee, D. G. Cahill and R. Venkatasubramanian, *Appl. Phys. Lett.* 1997, **70**, 2957.
136. I. W. Hamley, *Nanotechnology*, 2003, **14**, R39–R54.

137. R. A. Segalman, *Mater. Sci. Eng. Rep.* 2005, **48**, 191–226.

138. C. J. Hawker and T. P. Russell. Block Copolymer Lithography: Merging "Bottom-Up" with "Top-Down" Processes (Fabrication of Sub-45-nm Device Structures), December 2005, Volume 30, Issue 12, pp. 952-966

139. S. B. Darling, *Prog. Polym. Sci.* 2007, **32**, 1152–1204.

140. C. Minelli, C. Hinderling, H. Heinzelmann, R. Pugin, M. Liley, *Langmuir* 2005, **21**, 7080–2.

141. Morkved TL, Wiltzius P, Jaeger HM, Grier DG, Witten TA, *Appl. Phys. Lett.* 1994, **64**, 422–4.

142. W. A. Lopes, Heinrich M. Jaeger, *Nature,* 2001, **414**, 735-738.

143. W. A. Lopes, *Phys. Rev E.* 2002, **65**, 031606.

144. M. Kreuzer, C. Simão, A. Diaz, and C. M. Sotomayor Torres, *Macromolecules*, 2014, **47**, 8691–8699.

145. S. Sadasivam, Y. Chen, Z. Huang, L. Chen, S. Kumar, and T. S. Fisher, *Ann. Rev. Heat Transfer* 2014, **17**, 89–145.

146. Y. Chalopin, A. Rajabpour, H. Han, Y. Ni and S. Volz, *Ann. Rev. Heat Transfer* 2014, **17**, 147–176.

147. G. Kim and M. Libera, 1998, *Macromolecules,* **31**, 2670.

148. C. Harrison, *Macromolecules,* 2000, **33,** 857.

149. J. Liu, S. Ju, Y. Ding, R. Yang, *Appl. Phys. Lett.* 2014*,* **104**, 153110.

150. C. Lu, S. W.Chiang , H. Du, J. Li a, L. Gan, X. Zhang, X. Chu, Y. Yao B. Li F. Kang, *Polymer* 2017, **115,** 52.

151. M. C. George, M. A. Rodriguez, M. S. Kent, G. L. Brennecka, P. E. Hopkins, *J. Heat Transfe.* 2016, **138**, 024505-1.

152. H. Lee, Films, *Rev. Sci. Instrum.* 1982, **53**, 884–887.

153. L. Song, Y. Chen and J. W. Evans, *J. Electrochem. Soc.* 1997, **144**, 11.

154. M.-S. Hsiao, W. Y. Chen, J. X. Zheng, R. M. Van Horn, R. P. Quirk, D. A. Ivanov, E. L. Thomas, B. Lotz and S. Z. D. Cheng, *Macromolecules*, 2008, **41**, 4794-480.

Acknowledgements

At the end of this thesis I would like to thank many colleagues and friends for their support and contribution all these years in my research work. I would like to thank first Dr. Francesc Alzina, my academic mentor who supported, encouraged and guided my scientific work for more than three years. I have been impressed by his dedication in research, and his way of thinking has significantly influenced me. I am also grateful to him for giving me the freedom during my research work to follow new ideas, work in different environments, meet many researchers and explore new research fields. I hope that we will continue to work together in the future. I would like to thank also Prof. Clivia Sotomayor Torres, leader of the Phononic and Photonic Nanostructures group (P2N) at the Catalan Institute of Nanoscience and Nanotechnology (ICN2), firstly, because she gave me the opportunity to join her research group and secondarily, for her support and advices all these years. A special thank goes to Dr. Juan Sebastian Reparaz who essentially supported my experimental training and contributed in the main results of this thesis related to the Si membranes. In addition, I would like to thank particularly the postdoctoral researcher Dr. Bart Graczykowski for his support and all his help in the thermal measurements with the PnCs, which is one of the main topics of this thesis.

I thank also Dr. Marianna Sledzinska for the fabrication of the PnCs and generally for her help in issues related with a research project of the group. Many thanks also to Dr. Markus Wagner for the interesting discussions that we had and his contribution in my thesis work related with the disorder porous membranes. I am grateful also to Dr. Martin Kreuzer who worked with me in the fabrication of the BCPs, and Dr. Isabel Alonso and Dr. Alejandro Goñi who provided me the nanowire samples and contributed in the analysis of the experimental results. I would like also to thank Dr. Emigdio Chávez Ángel for his help to perform temperature measurements related with a research project of the group. I thank also the project manager of the group Mrs. Cristina Morales for all the help in many different issues during my stay in the group. I am thankful to all members of

the P2N group and the ICN2 for their support and the great time we had also apart from the scientific work.

External to my own research group, I have had the honour of working with many outstanding scientists. From my short research stays in the University of Lancaster and the Center of Energy and Thermal Sciences in Lyon, many thanks to Mr. Jean Spiece, Dr. Charalambos Evangeli, Prof. Oleg Kolosov, Dr. Pierre-Olivier Chapuis and Dr. Severine Gomes. I am grateful to all of them for their contribution to the results of my thesis. From my doctoral internship in the IBM-Research center in Zurich, I would like to thank Dr. Bernd Gotsmann, Mr. Fabian Motzfeld and Dr. Fabian Menges for the excellent collaboration and the interesting discussions that we had, and all the members of the Materials Integration and Nanoscale Devices (MIND) group.

Last but not least I would like to thank Carmen, Theodore and my family for their love and support.

Publication List

1. **A. El Sachat,** J. S. Reparaz, J. Spiece, M. I. Alonso, A. R. Goñi, M. Garriga, P. O. Vaccaro, M. R. Wagner, O. V. Kolosov, C. M. Sotomayor Torres and F. Alzina *"Thermal transport in epitaxial $Si_{1-x}Ge_x$ alloy nanowires with varying composition and morphology"*. (submitted 2017)

2. **A. El Sachat,** B. Graczykowski, M. R. Wagner, A. Shchepetov, M. Prunnila, J. Ahopelto, F. Alzina, C. M. Sotomayor Torres, and J. S. Reparaz, *"Temperature dependence of the thermal conductivity in Si low-dimensional suspended structures in the high temperature range from 400 K to 1000 K"*. (submitted 2017)

3. B. Graczykowski, **A. El Sachat**, J. S. Reparaz, M. Sledzinska, M. R. Wagner, E. Chavez-Angel, S. Volz, Y. Wu, F. Alzina and C. M. Sotomayor Torres, "*Thermal conductivity and air convection losses in periodic porous silicon membranes at high temperatures",* Nature Communication, 2017. (under revision)

4. M. R. Wagner, B. Graczykowski, J. S. Reparaz, **A. El Sachat,** M. Sledzinska, F. Alzina, and C. M. Sotomayor Torres: *"Two-Dimensional Phononic Crystals: Disorder Matters"*, Nano Letters, 16 (9), 5661–5668, 2016.

5. M. Sledzinska , B. Graczykowski , M. Placidi, D. S. Reig, **A. El Sachat,** J. S. Reparaz, F. Alzina, B. Mortazavi, R. Quey, L. Colombo, S. Roche, and C. M. Sotomayor Torres, *"Thermal conductivity of MoS_2 polycrystalline nanomembranes",* 2D Materials, 3, 3, 2016.

- Selected oral talks in Conferences and Workshops

1. **A. El Sachat,** B. Graczykowski, J. S. Reparaz , M. Sledzinska, M. R. Wagner, E. Chavez-Angel, S. Volz, Y. Wu, F. Alzina and C. M. Sotomayor Torres. *"Tuning the temperature dependence of the thermal conductivity in silicon membranes by nanopatterning",* **(oral talk)**, Eurotherm seminar 108-Nanoscale and Microscale Heat Transfer V, Santorini, Greece, 2016.

2. **A. El Sachat,** E. Guen, A. Robson, J. Spiece, M. Kreuzer, P.O Chapuis, S. Gomès, O. Kolosov, F. Alzina, C. M Sotomayor Torres*. "Structural and thermal properties of bare and chromium-covered block copolymer",* **(oral talk)**, Eurotherm seminar 108-Nanoscale and Microscale Heat Transfer V, Santorini, Greece, 2016.

3. **A. El Sachat,** J. S. Reparaz, B. Graczykowski, M. Sledzinska, F. Alzina, M. Wagner, A. Shchepetov, M. Prunnila, J. Ahopelto and C. M. Sotomayor Torres, *"Thermal conductinity of nanomembrane structures investigated using two-laser Raman thermometry",* **(oral talk),** European Materials Research Society (E-MRS) Fall Meeting, Warsaw (Poland), September 15-18, 2015.

4. **A. El Sachat,** F. Alzina, J. S. Reparaz, M. I. Alonso, M. Garriga, A. Ruiz, M. Alonso, P. O.Vaccaro, A. R.Goñi, and C. M. Sotomayor Torres. *"Structure, composition, and thermal properties of epitaxial* $Si_{1-x}Ge_x$ *alloy nanowires studied by scanning thermal microscopy",* **(oral talk)** Workshop: "Nanothermal Measurements and heat transport", York, United Kingdom, 15-16 December, 2015.

5. B. Graczykowski, **A. El Sachat,** J.S. Reparaz, M. Sledzinska, M. R. Wagner, E. Chavez-Angel, S. Volz, Y. Wu, F. Alzina, C. M. Sotomayor Torres, *"Thermal conductivity and air-mediated losses in periodic porous silicon membranes at high temperatures"*, **(oral talk)** 4th International conference on Phononic Crystals /Metamaterials,

Phonon Transport/ Coupling and Topological Phononics, Changsha, China, June 4-June 9, 2017.

6. M. R. Wagner, B. Graczykowski, J. S. Reparaz, **A. El Sachat**, M. Sledzinska, F. Alzina, C. M. Sotomayor Torres, *"Limitation of Hypersonic and Thermal Phonon Coherence by Disorder and Roughness in 2D Phononic Crystals"*, (invited talk) 4th International Conference on Phononic Crystals/Metamaterials, Phonon Transport/Coupling and Topological Phononics Changsha, China, June 4-June 9, 2017.

7. F. Alzina, J. S. Reparaz, B. Graczykowski, **A. El Sachat**, M. Sledzinska, E. Chávez-Ángel, M. R. Wagner, A. Shchepetov, M. Prunnila, J. Ahopelto, C. M. Sotomayor-Torres. *"Phonon dispersion engineering and thermal transport in Si membranes",* (Invited talk), Thermoelectric and Thermal Interface Materials 2, symposium 2, 28th ECS Meeting, Phoenix AZ, Oct 11-16, Nottingham, 2015.

8. C. M Sotomayor-Torres, B. Graczikowski, F. Alzina, M. Sledzinska, J. S. Reparaz, **A. El Sachat**, M. R. Wagner, A. Shchepetov, M. Prunnila, J. Ahopelto, *"Free-standing Silicon Membranes-based Phononic Crystals"*, (Invited talk) at NM5: Nanomembrane Materials from Fabrication to Application sumposium, 2016.